1

PM-1 3½"x4" PHOTOGRAPHIC MICROCOPY TARGET
NBS 1010a ANSI/ISO #2 EQUIVALENT

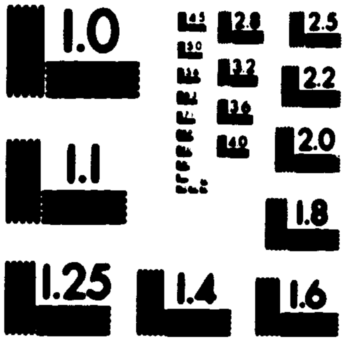

PRECISION℠ RESOLUTION TARGETS

National Library
of Canada

Acquisitions and
Bibliographic Services Branch

395 Wellington Street
Ottawa, Ontario
K1A 0N4

Bibliothèque nationale
du Canada

Direction des acquisitions et
des services bibliographiques

395, rue Wellington
Ottawa (Ontario)
K1A 0N4

Your file Votre référence

Our file Notre référence

NOTICE

The quality of this microform is heavily dependent upon the quality of the original thesis submitted for microfilming. Every effort has been made to ensure the highest quality of reproduction possible.

If pages are missing, contact the university which granted the degree.

Some pages may have indistinct print especially if the original pages were typed with a poor typewriter ribbon or if the university sent us an inferior photocopy.

Reproduction in full or in part of this microform is governed by the Canadian Copyright Act, R.S.C. 1970, c. C-30, and subsequent amendments.

AVIS

La qualité de cette microforme dépend grandement de la qualité de la thèse soumise au microfilmage. Nous avons tout fait pour assurer une qualité supérieure de reproduction.

S'il manque des pages, veuillez communiquer avec l'université qui a conféré le grade.

La qualité d'impression de certaines pages peut laisser à désirer, surtout si les pages originales ont été dactylographiées à l'aide d'un ruban usé ou si l'université nous a fait parvenir une photocopie de qualité inférieure.

La reproduction, même partielle, de cette microforme est soumise à la Loi canadienne sur le droit d'auteur, SRC 1970, c. C-30, et ses amendements subséquents.

Canada

UNIVERSITY OF ALBERTA

Computer Investigation of Stability Boundaries of Chemical Reaction Networks

by

Weimin Jiang ©

A Thesis
Submitted to the Faculty of Graduate Studies and Research
in Partial Fulfillment of the Requirements for the Degree of
Doctor of Philosophy

DEPARTMENT OF CHEMISTRY

EDMONTON, ALBERTA
Spring 1994

National Library of Canada

Acquisitions and Bibliographic Services Branch

395 Wellington Street
Ottawa, Ontario
K1A 0N4

Bibliothèque nationale du Canada

Direction des acquisitions et des services bibliographiques

395, rue Wellington
Ottawa (Ontario)
K1A 0N4

The author has granted an irrevocable non-exclusive licence allowing the National Library of Canada to reproduce, loan, distribute or sell copies of his/her thesis by any means and in any form or format, making this thesis available to interested persons.

L'auteur a accordé une licence irrévocable et non exclusive permettant à la Bibliothèque nationale du Canada de reproduire, prêter, distribuer ou vendre des copies de sa thèse de quelque manière et sous quelque forme que ce soit pour mettre des exemplaires de cette thèse à la disposition des personnes intéressées.

The author retains ownership of the copyright in his/her thesis. Neither the thesis nor substantial extracts from it may be printed or otherwise reproduced without his/her permission.

L'auteur conserve la propriété du droit d'auteur qui protège sa thèse. Ni la thèse ni des extraits substantiels de celle-ci ne doivent être imprimés ou autrement reproduits sans son autorisation.

ISBN 0-612-11247-0

Canada

UNIVERSITY OF ALBERTA

RELEASE FORM

NAME OF AUTHOR: *Weimin Jiang*

TITLE OF THESIS: **Computer Investigation of Stability Boundaries of Chemical Reaction Networks**

DEGREE: *Doctor of Philosophy*

YEAR THIS DEGREE GRANTED: 1994

(SIGNED) ____________________

Department of Chemistry
University of Alberta
Edmonton, Alberta, Canada T6G 2G2

DATED Dec. 20, 1993

UNIVERSITY OF ALBERTA

FACULTY OF GRADUATE STUDIES AND RESEARCH

The undersigned certify that they have read, and recommend to the Faculty of Graduate Studies and Research for acceptance, a thesis entitled **Computer Investigation of Stability Boundaries of Chemical Reaction Networks** submitted by *Weimin Jiang* in partial fulfillment of the requirements for the degree of *Doctor of Philosophy*.

Bruce L Clarke
Dr. Bruce Clarke (Supervisor)

Loren Hepler
Dr. Loren Hepler

Dr. Robert Jordan

Dr. Michael Menzinger

Dr. Krishnaswamy Nandakumar

Dr. Walter Thorson

DATED December 20, 1993

To my mother and father for the intelligence they gave me and for the hardship they experienced.

To Xiaoling, my wife, for her love and support which are critically important to me.

To Lulu, my seven-year-old daughter, who is learning and growing toward her bright future.

Abstract

Stability boundaries [illegible] important [illegible] the study of chemical reaction networks with nonlinear kinetics. [illegible] this area apply to nonlinear chemical, biochemical and environmental [illegible]. Potential applications in industry are also very promising.

This thesis focuses on computer investigation of stability boundaries. First, numerical algorithms and approximate analytical formulas for calculating steady state manifolds are discussed. Criteria for determining the stability of steady states are then presented with emphasis on the Hurwitz determinants and the first column of the Routh array. The global structure of stability boundaries for bifurcations from steady states is analysed using Orlando's theorem and the symmetrical eigenvalue curves. To study the dependence of stability boundaries on the experimental parameters, three methods are proposed for deriving explicit approximate stability boundary equations. For the situations where explicit equations are difficult to obtain, a slope pattern method is developed and it can be applied to any networks.

Two reaction networks are analyzed using the new methods. As an important prototype network, the Gray-Scott network is used to illustrate the details of the various methods. A complete stability analysis is conducted and the important extreme currents in various regions of the steady state manifold are found. The stability boundary structures and stability regions of the network are also explored in detail.

The bromate-sulfite-ferrocyanide (BSF) network is an important experimental reaction network. This thesis finds that the stability boundary structure of

the network is intrinsically different from the original interpretation of the experimental data. An in-depth investigation reveals the reasons for the previous misunderstanding and a procedure is developed to correct the problem. An excellent fit to the experimental results at $20^0 C$ was obtained by setting $k_1 = 5.765 \times 10^{-2} M^{-1} s^{-1}$ and $k_9 = 39.5 M^{-2} s^{-1}$. Among the twenty-eight extreme currents of the network, four are responsible for the saddle-node bifurcations in the experimental parameter range. They constitute a simplified network, whose stability boundary equations were derived. The feedback cycles responsible for the instability were found. They give physical insight into the reason for instability.

Acknowledgment

I sincerely appreciate the advice and help I received from my supervisor Dr. Bruce Clarke in completion of this thesis. I also would like to thank members of my Ph.D. advisory committee for their helpful discussions and suggestions. Special thanks are also extended to Dr. Michael Menzinger of University of Toronto who attended my Ph.D. final exam and discussed some very stimulating ideas with me.

Contents

List of Tables

List of Figures

I. Introduction

1.1 Brief history and background

When two or more chemicals are mixed in a closed container, the reactions will eventually reach an equilibrium state where the Gibbs free energy is a minimum. But in the real world, do all chemical reactions approach such equilibria states?

The answer is no. Real world chemical systems are mostly open systems. Flow reactors in chemical plants, human bodies and environmental systems are open systems. When a chemical system is open, has nonlinear kinetics, and is operating far from equilibrium, the system can exhibit exotic behaviour that is more interesting than simple exponential decay to the unique equilibrium state[1-3]. Biological and industrial implications have generated increasing interest[4-8] in exotic phenomena such as sustained oscillations, multi-stability and chaos during the last 30 years.

The first advance in this area was achieved by Lotka. As early as 1910, he showed that the law of mass-action and an autocatalytical process may cause oscillations in a chemical reaction[9]. In 1920, he presented another simple scheme where an open autocatalytic chemical system had sustained oscillations[10]. Even though there was evidence for the existence of such sustained oscillations at that time[11], real interest appeared only after Belousov[12] published his discovery of an inorganic redox reaction with sustained barely damped oscillations, and Zhabotinskii[13] intensively studied the reaction. The Belousov-Zhabotinskii reaction (the oxidation and bromination of malonic acid by acidic bromate, catalysed by Ce(IV) ions) and the FKN mechanism (Field-Körös-Noyes)[14] proposed for the BZ reaction have been used to lay the foundation for this field.

Among the many problems to be solved, the *stability boundary problem* is one of the most important. The objective is to find the boundaries of the regions in multi-dimensional parameter space where systems exhibit different stability behaviour such as asymptotic stability, sustained oscillations and bistability. The results can be applied directly to explain experimental observations, to evaluate *experimental parameters* such as rate constants or concentrations, and to predict system behaviour under different conditions where experiments have not been done or are difficult to do because of experimental obstacles.

There are two closely related concepts here. One is the stability boundary just mentioned, which is sometimes called the *bifurcation set*. The other is the *phase diagram*, which is a graph showing the regions divided by the stability boundaries. These regions are called *stability regions* because each region possesses its own stability properties.

Stability boundaries are hypersurfaces in a multi-dimensional parameter space. Because of mathematical difficulties arising from the nonlinearities, it is usually impossible to derive accurate analytical formulas for the stability boundaries of real reaction networks. To obtain insight into the sources of instability in complicated dynamic features, Gray and Scott proposed a two variable model network[15] and carried out a series of investigations on the network[16-20]. The stability boundaries for the Gray-Scott network show great richness of dynamical features in different stability regions in the parameter space. Further studies by Pearson found complex patterns when diffusion terms are included[21]. Boissonade and De Kepper[22] proposed another simple chemical scheme and studied the relationship between its bistability and oscillation regions. They found many small regions with various dynamic features near the crossing point in the *cross-shaped phase diagram*. Later, Guckenheimer[23] studied the mathematical details of the general cross-shaped phase diagrams, which has been used as a tool to help discover new chemical oscillators.

It is not difficult to imagine that real chemical networks are much more complicated because more parameters and variables are involved. In practice, researchers usually do the experiments by changing two experimental parameters while keeping all others fixed. The results are summarized in phase diagrams[24,25], where different stability regions are divided by stability boundaries. Based on the reaction mechanisms proposed for the experimental systems, either an IVP (Initial Value Problem) solver[25] or a two-parameter numerical continuation method[26] is used to calculate the stability boundaries. Using the IVP solver, the calculation is slow and the result is necessarily partial, as Olsen and Epstein[26] have pointed out. Even more seriously, the conclusions could be wrong even though they might meet the widely accepted expectations of a cross-shaped phase diagram. This will be discussed in detail later in the thesis. Using the two-parameter continuation method, results are usually accurate, but this method cannot give a global picture of stability boundaries, either quantitatively or qualitatively, in the whole multi-dimensional parameter space. It does not tell us how other parameters affect stability boundaries or phase diagrams. Ringland[27] recently pointed out that the qualitative structure of a two-parameter phase diagram can be changed very easily by a change in a third parameter. His rapid reconnaissance approach using numerical continuation can help look for qualitative changes. But in situations where more parameters are involved, this approach is hopeless, no matter how fast the computer or the algorithm.

1.2 New work in this thesis

Until recently, there have been no general methods or techniques available for obtaining stability boundaries in a multi-dimensional experimental parameter space. The most promising approach is called the *Stoichiometric Network Analysis* (SNA)$^{28-29}$. In this approach, Clarke proposed a set of new parameters, called $(\mathbf{h}, \mathbf{j})$ parameters, and developed the theory and algorithms to do stability analysis of chemical systems based on the $(\mathbf{h}, \mathbf{j})$ parameters. It is the only successful attempt up to now to explore the stable and unstable regions throughout the whole parameter space. The basic ideas of SNA have recently been used by other authors to study various aspects of nonlinear chemical dynamics$^{30-35}$.

Although SNA was a very effective approach, improvements were required. Since results provided by Clarke's program package were in terms of $(\mathbf{h}, \mathbf{j})$ parameters, their direct application to real chemistry problems was limited because chemical experimental results are usually presented in conventional experimental parameters. Therefore, it was essential to develop a method for converting between the $(\mathbf{h}, \mathbf{j})$ parameters and the conventional experimental parameters. The conventional experimental parameters are the set of rate constants $\mathbf{k} = (k_1, k_2, \cdots, k_r)$ and the amounts of the conserved species $\mathbf{C} = (C_1, C_2, \cdots, C_m)$. They will be called $(\mathbf{k}, \mathbf{C})$ *parameters*. It is not possible to interpret and predict experimental results using the SNA without a mapping between the $(\mathbf{h}, \mathbf{j})$ and the $(\mathbf{k}, \mathbf{C})$ parameters.

A formula giving the $(\mathbf{k}, \mathbf{C})$ parameters in terms of the $(\mathbf{h}, \mathbf{j})$ parameters was discussed by Clarke. The difficult problem is to calculate the $(\mathbf{h}, \mathbf{j})$ parameters from the $(\mathbf{k}, \mathbf{C})$ parameters. The $\mathbf{h}$ *parameters* are defined as the reciprocals of the steady state concentrations. This problem requires calculating steady state concentrations in terms of rate constants $\mathbf{k}$. Due to the nonlinear nature of the equations involved, it is usually impossible to derive accurate analytical solutions.

There are two possible ways to approach this problem. One is numerical and one is analytical. Computer programs which calculate the steady state manifold are now available on mainframe computers and workstations. AUTO is such a program[36]. It is not convenient to use these program packages because of technical reasons. For example, the AUTO package needs to be recompiled for each network that is treated. It calculates steady state manifolds but not phase diagrams. It puts all calculated points into a file and a separate graphics program must be used to display the results. To solve this problem, I developed a program to do the calculation on IBM personal computers. Using my program, one clicks a mouse button and a plot of the steady state concentrations vs. rate constants is promptly displayed on the screen. The steady states are colored to represent different stability properties. Changes of steady state concentrations with a specific rate constant are obtained at fixed settings of all other rate constants. Changing the rate constants can be done quickly by dragging the mouse. This allows us to focus our attention on a kinetically interesting region in parameter space. It also enables us to flip back and forth easily between the unstable region screen in $(\mathbf{h}, \mathbf{j})$ space and the steady state manifold screen in $(\mathbf{k}, \mathbf{C})$ space. Corresponding stability regions in the two spaces can be compared efficiently.

The analytical approach derives approximate analytical equations for the steady state manifold in the regions of interest. For this purpose, I developed three methods which can be used in different circumstances. The resulting equations show the explicit dependence of steady state concentrations on the experimental parameters.

After the $\mathbf{h}$ parameters have been calculated from the $(\mathbf{k}, \mathbf{C})$ parameters, the vector $\mathbf{j}$ may be calculated easily, either numerically or analytically. Once the $\mathbf{j}$ vector is calculated, the stability boundaries can be calculated without difficulty. The stability boundaries calculated in this way not only provide us with knowledge of different stability regions, but also reveal the important factors that determine the stability.

The analytical stability boundaries derived using SNA in the $(\mathbf{h}, \mathbf{j})$ space are based on three approximations[37]. We need accurate numerical stability boundaries to test the approximate equations, and to show the detailed stability boundary structures on 2-dimensional subspaces. I could have used software packages that explicitly evaluate the signs of the Jacobian matrix eigenvalues[36]; however, I developed a new software package which fits much better into the SNA approach. An important mathematical concept called the Hurwitz determinant has been used by Clarke for many years. This thesis extends the application of Hurwitz determinants using Orlando's theorem and the Routh array. Stability boundaries defined and calculated this way show very interesting geometrical structures, which cannot be obtained using other software packages.

Using these methods and programs, I carried out research on several important reaction networks. They include the Gray-Scott (GS) network[15], the Chloride-Iodide network[24], the Showalter-Noyes-Bar-Eli (SNB) network[38], and the Bromate-Sulfite-Ferrocyanide (BSF) network[25]. Among them, the GS network and the BSF network received the most emphasis. I paid particular attention to their stability boundaries in experimental parameter space and to their sources of instability.

Besides the above work, I have also removed another barrier of the old SNA program package. The package restricted the number of intermediates to eight species. The new algorithms can handle any number of intermediates, so the package can be used to study larger and more realistic systems.

1.3 Prospects

Today's SNA package makes analyzing reaction networks enjoyable. We can analyze various experimental and model reaction networks with a few clicks of the mouse. The package is not only efficient, it also finds the unique and important features of the stability boundary diagrams. It is expected that a wide range of chemical reaction networks will be analyzed in the near future with very high efficiency. The outcome will be applied to explain experimental observations, to elucidate reaction mechanisms, to evaluate rate constants, and to predict experimental results.

II. Steady states of chemical reaction networks

To analyze stability boundaries of chemical reaction networks, we first need to define, calculate and understand their steady state manifolds. This chapter discusses the definition of steady states, the treatment of steady states in terms of two different sets of parameters, an effective algorithm for numerical calculation of steady state manifolds in log space, and the methods for deriving analytical steady state equations in the multi-dimensional experimental parameter space. It will lay a foundation for the following chapters.

2.1 Reaction systems and reaction networks

2.1.1 Reaction systems and reaction networks

In chemistry, complicated chemical reactions are made from simple reaction steps called *elementary reactions*. The set of elementary reactions for a complicated reaction constitutes a *reaction mechanism* for the reaction. The definition of a reaction mechanism includes the following information:

1. reactants, products and intermediates of the reaction,
2. stoichiometry of the reaction,
3. kinetic orders with respect to each reactants and intermediates.

In this thesis, the term '*reaction network*' has the same meaning as the term 'reaction mechanism' defined above; however, the reactions in a reaction network need not be elementary. They could be complex reactions, which are composed of elementary steps.

We consider that a reaction mechanism may be specified without giving rate constants for each reaction. Rate constants are parameters rather than being part of a mechanism. A mechanism only specifies how the chemicals react with each other but does not indicate how fast or how far the reactions will go.

To express the effect of rate constants on reaction kinetics, the term *reaction system* is used. A reaction system is a reaction network with a specified vector $\mathbf{k}$ of rate constants. It corresponds to a real reaction system in a laboratory, which runs under a specific temperature, pressure and other experimental conditions. The experimental conditions determine the specific rate constants. A reaction network is a set of reaction systems, one for each possible set of rate constants.

2.1.2 Reaction network diagrams

A reaction network can be represented by a *network diagram*. Fig. 1 is a typical reaction network diagram using Clarke's notation[30]. On the diagram, the numbers of head barbs and tail feathers at each chemical on the branched arrows indicate the stoichiometry of each reaction. The number of left feathers on a tail represents the kinetic order with respect to the chemical. Single line arrows indicate forward reactions while double line arrows show reversible reactions. Each chemical appears only once in a reaction network diagram. Chemical formulas enclosed in cup-shaped symbols are *major species*. They are either chemicals in *CSTR (Continuous Stirred Tank Reactor)* reservoirs or chemicals whose concentrations change so slowly that they are considered constant in the time scale of interest. In some cases, they could also be reaction products that are washed out of the reactor by a CSTR flow without affecting the dynamics of other species. This last type of major species is also called a *downstream species*. Chemical formulas without cup-shaped symbols are called *dynamic intermediates* or simply *intermediates*. When we talk about dynamic features or stabilities, we are referring to these dynamic intermediates.

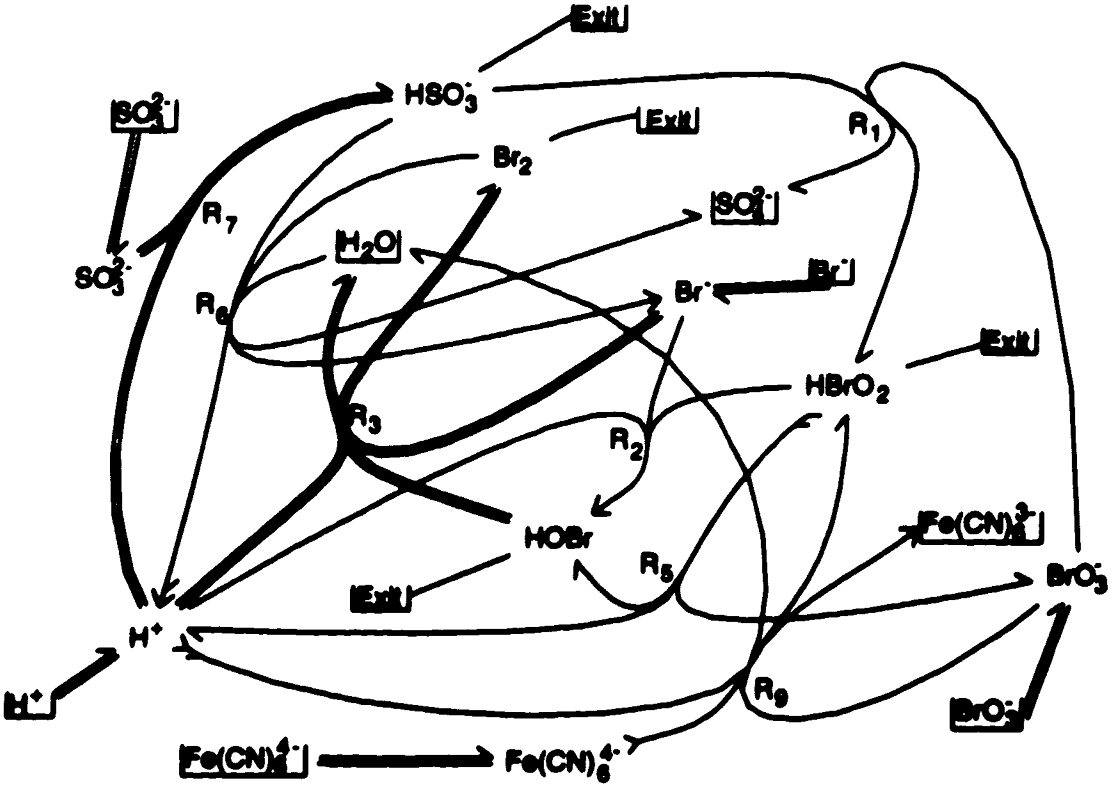

Fig. 1 Network diagram of the bromate-sulfite-ferrocyanide network.

The network diagram in Fig. 1 represents the reactions involving bromate, sulfite and ferrocyanide in a CSTR system. This mechanism was proposed by Edblom, Luo, Orban, Kustin, and Epstein[25] (ELOKE) and is given in Scheme I.

Scheme I:

$$\mathrm{BrO_3^- + HSO_3^- \xrightarrow{k_1} HBrO_2 + SO_4^{2-}}$$

$$\mathrm{HBrO_2 + Br^- + H^+ \xrightarrow{k_2} 2HOBr}$$

$$\mathrm{HOBr + Br^- + H^+ \underset{k_4}{\overset{k_3}{\rightleftharpoons}} Br_2 + H_2O}$$

$$\mathrm{2HBrO_2 \xrightarrow{k_5} BrO_3^- + HOBr + H^+}$$

$$\mathrm{Br_2 + HSO_3^- + H_2O \xrightarrow{k_6} 2Br^- + SO_4^{2-} + 3H^+}$$

$$H^+ + SO_3^{2-} \underset{k_8}{\overset{k_7}{\rightleftharpoons}} HSO_3^-$$

$$BrO_3^- + 2Fe(CN)_6^{4-} + 3H^+ \xrightarrow{k_9} HBrO_2 + 2Fe(CN)_6^{3-} + H_2O$$

The reactions which ELOKE called $B_1, B_2, \ldots$ are called $R_1, R_2, \ldots$ here. The reversible reaction which ELOKE called B_3 and B_4 is shown as a single reaction R_3 on the diagram with a double line to indicate reversibility. The same comment applies to reactions B_7 and B_8.

2.2 Steady states of reaction networks

2.2.1 Conventional steady state conditions

For a chemical reaction network with n intermediates and r reactions, the kinetic equations of the network can be written as

$$\frac{d\mathbf{X}}{dt} = \mathbf{N}\mathbf{v}, \tag{1}$$

where $\mathbf{X}$ is the concentration vector with n components; $\mathbf{N}$ is the n by r stoichiometric matrix, and $\mathbf{v}$ is the reaction rate vector with r components.

At a *steady state*, rates of concentration change are zero for all intermediates. Therefore,

$$\frac{d\mathbf{X}_0}{dt} = \mathbf{N}\mathbf{v}^0 = 0, \tag{2}$$

where $\mathbf{X}_0$ is $\mathbf{X}$ at the steady state and $\mathbf{v}^0$ is $\mathbf{v}$ at the steady state.

Steady state reaction rates can be expressed in different forms depending on the parameter set used. In the conventional experimental parameter space,

$$\mathbf{v}^0 = \mathrm{diag}(\mathbf{k})\mathbf{X}_0^{\mathbf{K}}, \tag{3}$$

where $\mathbf{k} = (k_1, k_2, \cdots, k_r)$ is the rate constant vector with r components; diag(**k**) is a n by n diagonal matrix whose diagonal elements are $k_1, k_2, \cdots, k_n$; $\mathbf{K} = (\kappa_{ij})$ is the n by r kinetic matrix. The order of reaction j in species i is κ_{ij}. The expression $\mathbf{X}_0^{\mathbf{K}}$ represents a vector whose j-th component is

$$(\mathbf{X}_0^{\mathbf{K}})_j = \Pi_{i=1}^{n} X_{0,i}^{\kappa_{ij}},$$

where $X_{0,i}$ is the steady state concentration of the i-th intermediate.

Substituting equation (3) into (2) gives the conventional steady state condition,

$$\frac{d\mathbf{X}_0}{dt} = \mathbf{N}\mathbf{v}^0 = \mathbf{N}(\mathrm{diag}(\mathbf{k}))\mathbf{X}_0^{\mathbf{K}} = 0, \tag{4}$$

which is a system of nonlinear equations. Generally speaking, its solutions cannot be expressed by explicit formulas.

2.2.2 Extreme currents and steady state conditions in j parameters

Steady state conditions can also be expressed in a much simpler form using appropriate parameters. Clarke[20] invented a new set of parameters called the (**h**, **j**) *parameters* in order to simplify the stability analysis.

Consider the meaning of equations (1) and (2). In equation (1), **v** is a reaction rate vector for all r reactions. Each component of **v** gives the speed from the left to the right of a chemical equation

$$\mathrm{A} + \mathrm{B} + \ldots \longrightarrow \mathrm{C} + \mathrm{D} + \ldots.$$

If we imagine the reaction to be a flow of chemicals from the left to the right in the chemical equation (even though chemicals are changed in the course of this flow, we imagine them to be flowing), then a sequence of reactions $(R_1, R_2, R_3, ..., R_n)$

will form a current of the flow. In equation (2), a restriction is imposed on the reaction rates to keep the reaction network at a steady state. We call a steady state reaction rate vector $\mathbf{v}^0$ *a steady state current*, or *a current*. In this way, flowing chemicals through a reaction network are treated like flowing electricity through an electrical network. Then concepts of electrical network theory should help us investigate chemical reaction networks.

Clarke found that currents have a geometrical interpretation. Based on linear programming ideas[40], he proved that the set of all currents of a reaction network constitutes a convex polyhedral cone[41,42], called the *current cone*. Fig. 2 shows some simple current cones in a three-dimensional space. Note that in a three-dimensional space, current cones can be 1, 2 or 3 dimensional. The edges of a convex polyhedral cone are called *half-lines* or *rays*. Since they are the extreme points of a convex set, they are called *extreme currents*. Chemically, extreme currents correspond to basic chemical pathways through which the intermediates achieve steady states. The term "extreme current" will sometimes be shortened to *current* for brevity when the meaning is clear from the context.

Because of the geometrical structure mentioned above, any current $\mathbf{v}^0$ can be written as a linear combination of extreme currents, i.e.

$$\mathbf{v}^0 = \mathbf{E}\mathbf{j}. \tag{5}$$

Here $\mathbf{E}$ is the r by f extreme current matrix. Each of the f columns of the $\mathbf{E}$ matrix is an extreme current. Each component of $\mathbf{j} = (j_1, j_2, \ldots, j_f)$ is a weighting factor, which measures the relative importance of the flow for each extreme current. We call j_i the *rate of extreme current* $\mathbf{E}_i$.

Substituting equation (5) into (2) gives the steady state conditions in the $\mathbf{j}$

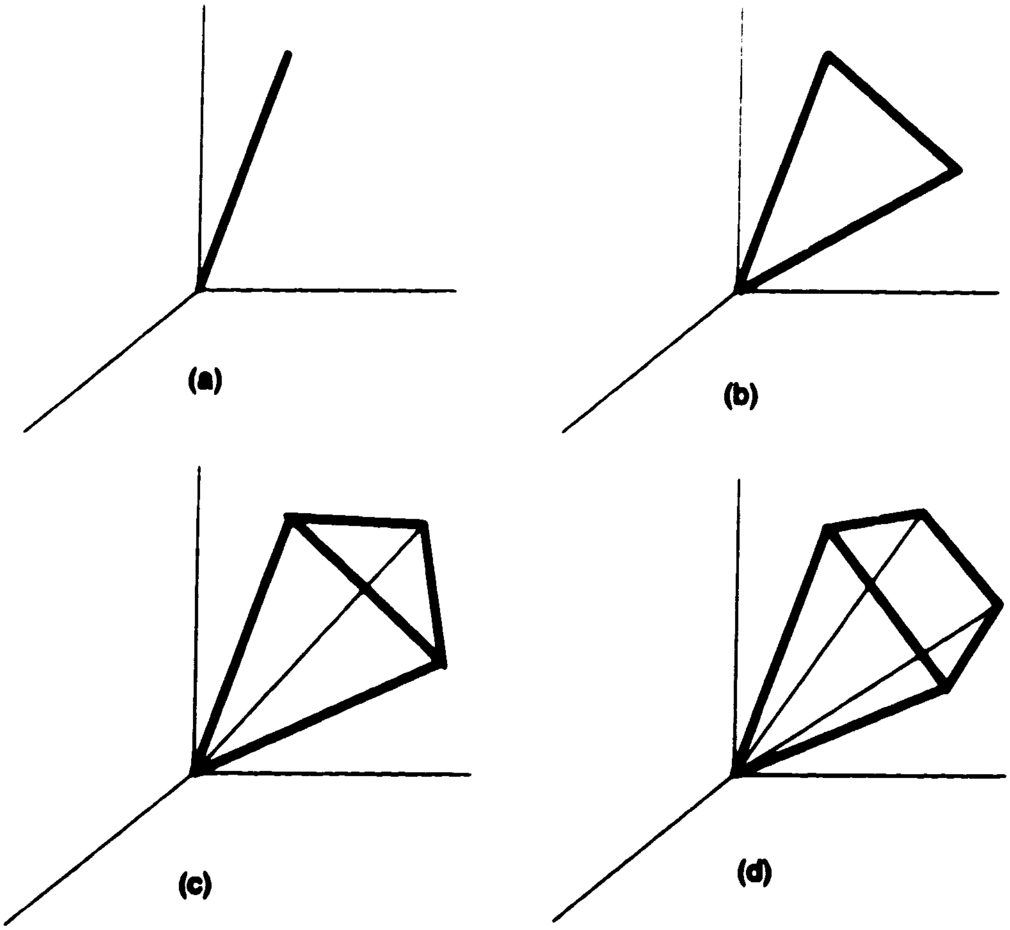

Fig. 2 Some simple current cones in a three-dimensional space. Note that the dimensions of the cones themselves are (a) one-dimensional, (b) two-dimensional, (c) three-dimensional, and (d) three-dimensional.

parameters,

$$\frac{d\mathbf{X}_0}{dt} = \mathbf{N}\mathbf{v}^0 = \mathbf{N}\mathbf{E}\mathbf{j} = 0. \tag{6}$$

Since every column of $\mathbf{E}$ is a steady state, $\mathbf{N}\mathbf{E} = 0$ identically. Hence every $\mathbf{j}$ represents a steady state.

2.2.3 Two sets of steady state parameters: (k, C) and (h, j) parameters

We have seen that steady states of chemical reaction networks can be described by different parameters. Let's have a closer look at these parameters and examine their relationships to each other.

As we have seen in Section 2.2.1, steady state conditions of a reaction network with r reactions and n intermediates can be presented by equation (2). If there exist some conservation conditions among chemical intermediates, then not all rows of $\mathbf{N}$ are independent. Let the number of independent rows of the matrix $\mathbf{N}$ be d, that is $d = \text{rank}(\mathbf{N})$. If there are conservation conditions, d is smaller than n. The difference $n - d$ is the number of conservation conditions. The dynamics of the network is then d-dimensional.

The $(\mathbf{k}, \mathbf{C})$ parameter vector is the complete set of parameters that are widely used in chemistry. In this set of parameters, there are r rate constant parameters $\mathbf{k}$, and $n - d$ conservation condition parameters $\mathbf{C}$. The total number of parameters is $r + n - d$. If there are no conservation conditions, then $d = n$, and the total number of parameters is r. These are rate constants.

The $(\mathbf{h}, \mathbf{j})$ parameters are the parameters proposed by Clarke. Definition of the $\mathbf{j}$ parameters has been given by equation (5). The $\mathbf{h}$ parameters are defined as reciprocals of steady state concentrations of all intermediates, i.e.,

$$\mathbf{h} = \frac{1}{\mathbf{X}_0}, \tag{7}$$

or

$$h_i = \frac{1}{X_{0,i}}.$$

Since there are n intermediates, there are n $\mathbf{h}$-parameters. To make the total number of parameters be $r + n - d$, the number of independent $\mathbf{j}$ parameters must be $r - d$. In other words, dimension of the current cone is $r - d$ in general. For networks without conservation conditions, $d = n$, so the dimension is $r - n$.

Cross sections of a current cone are called *current polytopes*. The dimension of a current polytope is one less than the dimension of its corresponding current cone. Hence the dimension of a current polytope is $r - d - 1$. Fig. 3 shows current polytopes corresponding to the current cones shown in Fig. 2. Any steady state current vector can be expressed as a point in a current polytope.

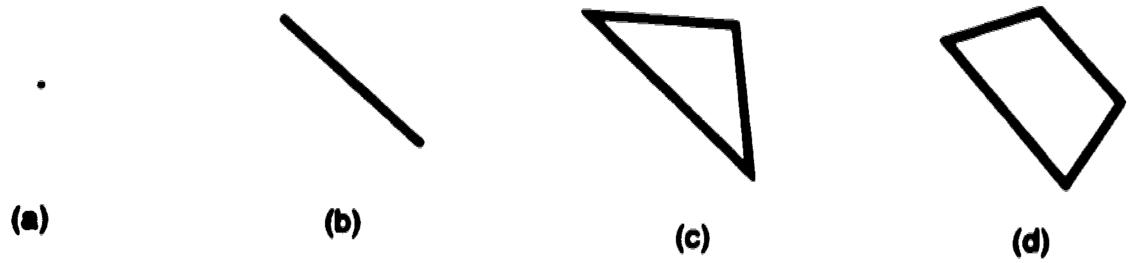

Fig. 3 Current polytopes corresponding to the current cones shown in Fig. 2. Dimensions of the current polytopes are one less than dimensions of the corresponding current cones.

In the $(\mathbf{k}, \mathbf{C})$ parameter space, the steady states of a reaction network form a steady state manifold. In $(\mathbf{h}, \mathbf{j})$ space, the same set of steady states forms a convex polyhedral cone. Clarke[28,42] proved that a smooth 1-1 mapping exists between the steady states in the two representations. The $(\mathbf{h}, \mathbf{j})$ space cone is an unfolding of the corresponding steady state manifold in the $(\mathbf{k}, \mathbf{C})$ space.

The two sets of steady state parameters can be inter-converted. It is easy to calculate $(\mathbf{k}, \mathbf{C})$ parameters from $(\mathbf{h}, \mathbf{j})$ parameters. According to equations (3), (5) and (7),

$$\mathbf{E}\mathbf{j} = \mathrm{diag}(\mathbf{k})\mathbf{X}_0^{\mathsf{K}} = \mathrm{diag}(\mathbf{k})\mathbf{h}^{-\mathsf{K}}. \tag{8}$$

Here,

$$(\mathbf{h}^{-\mathsf{K}})_j = \Pi_{i=1}^{n}\left(\frac{1}{h_i}\right)^{\kappa_{ij}} \qquad j = 1, 2, \cdots, r.$$

Solving this for $\mathbf{k}$ gives

$$\mathbf{k} = \mathrm{diag}(\mathbf{E}\mathbf{j})(\mathbf{h}^{\mathbf{K}}). \tag{9}$$

The $\mathbf{C}$ parameters can be directly calculated from the $\mathbf{h}$ vector and a *conservation matrix* $\mathbf{\Gamma}$,

$$\mathbf{C} = \mathbf{\Gamma}\mathbf{h}^{-1}. \tag{10}$$

$\mathbf{\Gamma}$ is an $(n-d)$ by n matrix that shows the conservation of atoms, functional groups or electrical charges.

Calculating $(\mathbf{h},\mathbf{j})$ parameters from $(\mathbf{k},\mathbf{C})$ parameters is much more difficult because of the nonlinear nature of equation (8) with respect to the $(\mathbf{h},\mathbf{j})$ parameters. If we could do this calculation analytically, we would be able to calculate stability boundaries directly from the systems of inequalities in the $(\mathbf{h},\mathbf{j})$ space. This thesis develops an approach to calculate $(\mathbf{h},\mathbf{j})$ from two angles. One is to calculate $\mathbf{X}_0$ (thus $\mathbf{h}$) from $\mathbf{k}$ parameters numerically, and then calculate steady state reaction rates $\mathbf{v}^0$. Equation (5) is solved for $\mathbf{j}$ vector, as discussed in Ref. 43. The other is to develop approximate analytical formulas. Both methods should be considered complementary and will be used for different purposes.

2.3 Numerical calculation of steady state manifolds in log space

In the $(\mathbf{k},\mathbf{C})$ parameter space, for networks without conservation conditions, the steady state concentrations of intermediates depend on the following parameters:

1. $k_1, k_2, \ldots, k_r$: the rate constants of true chemical reactions,
2. k_0 : the CSTR flow rate,

3. $A_{0,1}, A_{0,2}, \ldots$: the concentrations that each input species would attain in the CSTR if no reactions took place. They are also referred to as the *concentrations of CSTR input species in the reservoir*;
4. $M_1, M_2, \ldots$: the concentrations of major species, i.e., the species whose concentrations are assumed to be constant during the reactions.

We call these *abscissa parameters* because they will be plotted horizontally when showing the steady state manifolds. Abscissa parameters are either **k** parameters themselves or parameters that determine **k**. We want to know how the steady state concentrations of intermediates change with the abscissa parameters.

The condition for a reaction network to be at steady states can be written as

$$\frac{d\mathbf{X}_0}{dt} = \mathbf{f}(\mathbf{X}_0, \mathbf{k}) = 0. \tag{11}$$

We want to plot the solutions of the system of equations (11) as a function of any given abscissa parameter a in the log space. The **k** parameters depend on a and are given by known functions $\mathbf{k}(a)$. The form of the function depends on which type of parameter is used for a. The solutions $\mathbf{X}_0$ at steady states satisfy

$$\mathbf{f}(\mathbf{X}_0(a), \mathbf{k}(a)) = 0 \tag{12}$$

Our purpose is to calculate $\log \mathbf{X}_0(a)$ against $\log a$, which requires evaluating the dependence of the solution of a system of equations on the parameter a. The curve $(\log \mathbf{X}_0(a), \log a)$ can be obtained by a numerical continuation method provided a starting point $(\log \mathbf{X}_0(a_0), \log a_0)$ is known.

The numerical continuation method I programmed into SNA is an extension and refinement of an algorithm developed by Kubíček[44]. It uses Gaussian elimination with controlled pivoting[45], the Adams-Bashforth explicit multi-step method of integration[45], and the Newton method as a corrector to improve the results[44,45]. I also developed a method to decide the direction of the solution curve as the continuation method was being applied. The details are provided in Appendix I. Here I discuss only a new general form for the Jacobian matrix which is valid for all stoichiometric methods.

According to equations (4) and (12),

$$\mathbf{f}(\mathbf{X}_0(a), \mathbf{k}(a)) = \mathbf{N}\mathrm{diag}(\mathbf{k}(\mathrm{a}))\mathbf{X}_0{}^{\mathbf{K}}(a) = 0$$

at the steady states $\mathbf{X}_0(a)$. Consider a curve $\log \mathbf{X}_0(a)$ vs. $\log a$. Let τ be the arc length along such a curve. Then $\log \mathbf{X}_0$ and $\log a$ are functions of τ. Thus $(\log \mathbf{X}_0(\tau), \log a(\tau))$ are the points on the curve for τ in some range. Therefore

$$\frac{d\mathbf{f}}{d\tau} = \frac{\partial[\mathbf{N}\mathrm{diag}(\mathbf{k})\mathbf{X}_0{}^{\mathbf{K}}]}{\partial \ln \mathbf{X}_0}\frac{d \ln \mathbf{X}_0}{d\tau} + \frac{\partial[\mathbf{N}\mathrm{diag}(\mathbf{k})\mathbf{X}_0{}^{\mathbf{K}}]}{\partial \ln a}\frac{d \ln a}{d\tau} = 0 \qquad (13)$$

where a is the abscissa parameter. Note that ' ln ' is used in equations for the simplicity of calculation. It can be converted to 'log' after the calculation is done.

The terms in the Jacobian matrix in equation (13) can be evaluated explicitly.

$$\frac{\partial[\mathbf{N}\mathrm{diag}(\mathbf{k})\mathbf{X}_0{}^{\mathbf{K}}]}{\partial \ln \mathbf{X}_0} = \mathbf{N}\mathrm{diag}(\mathbf{k})\mathrm{diag}(\mathbf{X}_0{}^{\mathbf{K}})\mathbf{K}^t = \mathbf{N}\mathrm{diag}(\mathbf{v})\mathbf{K}^t \qquad (14)$$

$$\frac{\partial[\mathbf{N}\mathrm{diag}(\mathbf{k})\mathbf{X}_0{}^{\mathbf{K}}]}{\partial \ln a} = \mathbf{N}\frac{\partial}{\partial \ln a}\begin{pmatrix} k_1 & 0 & \cdots & 0 \\ 0 & k_2 & \cdots & 0 \\ \vdots & \vdots & \ddots & \vdots \\ 0 & 0 & \cdots & k_r \end{pmatrix}\mathbf{X}_0{}^{\mathbf{K}} \qquad (15)$$

where $\mathbf{K}^t$ is the transpose of $\mathbf{K}$.

The derivatives of k_i with respect to $\ln a$ in equation (15) depend on the parameter a and on the forms of the functions $\mathbf{k}(a)$. The derivatives of the four types of abscissa parameters listed earlier fall into the following six cases:

a) k_i does not depend on a: then

$$\frac{\partial k_i}{\partial \ln a} = 0;$$

b) $k_i = a$: then

$$\frac{\partial k_i}{\partial \ln a} = \frac{\partial a}{\partial \ln a} = a = k_i;$$

c) $k_i = ak_0$, where k_0 is the flow rate of CSTR; a is the concentration of a species in a CSTR reservoir: then

$$\frac{\partial k_i}{\partial \ln a} = k_0 \frac{\partial a}{\partial \ln a} = k_0 a = k_i;$$

d) $k_i = A_0 a$, where a is the flow rate of CSTR; A_0 is the concentration of a species in a CSTR reservoir: then

$$\frac{\partial k_i}{\partial \ln a} = A_0 \frac{\partial a}{\partial \ln a} = A_0 a = k_i;$$

e) $k_i = M^{\kappa_{c_i}} a$, where a is the true rate constant of a reaction involving a major species as a reactant; M is the concentration of the major species; κ_{c_i} is the kinetic order with respect to the major species: then

$$\frac{\partial k_i}{\partial \ln a} = M^{\kappa_{c_i}} \frac{\partial a}{\partial \ln a} = M^{\kappa_{c_i}} a = k_i;$$

f) $k_i = k_i^* a^{\kappa_{c_i}}$, where a is the concentration of a major species;κ_{c_i} is the kinetic order with respect to a; k_i^* is the true rate constant of the reaction: then

$$\frac{\partial k_i}{\partial \ln a} = k_i^* \cdot \kappa_{c_i} \cdot a^{\kappa_{c_i}} = k_i \cdot \kappa_{c_i}.$$

The six cases above can be classified into three classes:

class i) $\frac{\partial k_i}{\partial \ln a} = 0;$

class ii) $$\frac{\partial k_i}{\partial \ln a} = k_i;$$

class iii) $$\frac{\partial k_i}{\partial \ln a} = k_i \cdot \kappa_{r_i}.$$

These expressions for $\frac{\partial k_i}{\partial \ln a}$ enable us to calculate $\frac{\partial[\mathbf{N}\mathrm{diag}(\mathbf{k})\mathbf{X}_0{}^{\mathbf{K}}]}{\partial \ln a}$ using equation (15).

Equation (13) is a system of n equations in $n+1$ variables, which include the n components of the $\frac{d \ln \mathbf{X}_0}{d\tau}$ and $\frac{d \ln a}{d\tau}$. To solve the system of equations, we need the $(n+1)$-th equation

$$\sum_{i=1}^{n}(d \ln X_i)^2 + (d \ln a)^2 = (d\tau)^2$$

which defines τ to be the arc length.

Based on the Jacobian evaluation formulas discussed above, the numerical continuation of steady state manifolds is carried out and the results are displayed on the computer screen. By clicking the mouse, different cross-sections of the calculated steady state manifold can be seen on the screen. We can quickly observe how various chemical concentrations change with any abscissa parameter.

2.4 Analytical steady state equations in the $(\mathbf{k}, \mathbf{C})$ *parameter space*

The steady state manifold in the log space often appears to be composed of several segments which are close to linear. If this is the case, then it should be possible to approximate the steady state manifold using linear equations.

I will discuss two techniques for obtaining analytical steady state equations. One is a geometrical method based on slope measurements of the linear parts. Since linear equations represent hyperplanes in a multi-dimensional space, the method will be called the *hyperplane approximation in* log *space*. The second method is algebraic and is based on the concept of *dominant extreme current*. It will be called the *dominant extreme current approximation*. The first method can produce analytical steady state equations directly without any chemical basis. The second method depends on the chemical processes in the network and provides insight into the important reactions at steady states.

2.4.1 Hyperplane approximation in the log space

Let X_i be the steady state concentration of the i-th intermediate for $i = 1, 2, \cdots, d$. Suppose there are m abscissa parameters, $a_1, a_2, \cdots, a_m$, whose values determine X_i, i.e.

$$\log X_i = \log X_i(\log a_1, \log a_2, \cdots, \log a_m).$$

Then,

$$d\log X_i = (\frac{\partial \log X_i}{\partial \log a_1})d\log a_1 + (\frac{\partial \log X_i}{\partial \log a_2})d\log a_2 + \cdots + (\frac{\partial \log X_i}{\partial \log a_m})d\log a_m.$$

In the linear region, all slopes are approximately constant, so we have

$$(\frac{\partial \log X_i}{\partial \log a_1}) = s_{i1}, \qquad (\frac{\partial \log X_i}{\partial \log a_2}) = s_{i2}, \qquad \cdots, \qquad (\frac{\partial \log X_i}{\partial \log a_m}) = s_{im}.$$

and

$$d\log X_i = \sum_{j=1}^{m} s_{ij} d\log a_j. \tag{16}$$

Integrating equation (16) gives the equation of the hyperplane tangent to the steady state manifold at the point where the partial derivatives are evaluated. The equation is

$$\log X_i = \sum_{j=1}^{m} s_{ij} \log a_j + c_i \tag{17}$$

where c_i is an integration constant. In the non-log space, equation (17) has the form

$$X_i = C_i a_1^{s_{i1}} a_2^{s_{i2}} \cdots a_m^{s_{im}} = C_i \prod_{j=1}^{m} a_j^{s_{ij}}. \qquad (18)$$

with a constant coefficient C_i. The matrix form of Equation (17) is

$$\log \mathbf{X} = \mathbf{S} \log \mathbf{a} + \mathbf{c},$$

where $\mathbf{S} = (s_{ij})$.

For convenience in determining slopes of linear regions, we plot steady state manifold curves using an *isotropic scale*. Unit lengths of vertical and horizontal axes are at 1:1 ratio with this scale. We measure the slopes of different line segments against all abscissa parameters and get approximate linear equations for the steady state manifolds in the neighbourhood of a chosen point.

2.4.2 Example: hyperplane approximation for the steady state manifold of the Gray-Scott network

The Gray-Scott network is an important reaction network with rich dynamical features. I will discuss this network in detail in chapter V. For now this network will be used to illustrate the hyperplane approximation method.

The Gray-Scott network contains two intermediates and six reactions. They are shown in Scheme II.

Scheme II:

R_1=1	$A+2B \xrightarrow{k_1} 3B$	$v_1 = k_1 AB^2$
R_2=2	$B \xrightarrow{k_2}$	$v_2 = k_2 B$
R_3=A exit	$A \xrightarrow{k_0}$	$v_3 = k_0 A$
R_4=B exit	$B \xrightarrow{k_0}$	$v_4 = k_0 B$

$$R_5 = \text{A inflow} \quad \xrightarrow{k_0 A_0} A \quad v_5 = k_0 A_0$$

$$R_6 = \text{B inflow} \quad \xrightarrow{k_0 B_0} B \quad v_6 = k_0 B_0.$$

A and B are the two dynamical intermediates; A_0, B_0 are their concentrations in the CSTR reservoir; k_0 is the flow rate of the CSTR flow; k_1, k_2 are the two true rate constants.

The network diagram of the GS network is shown in Fig. 4.

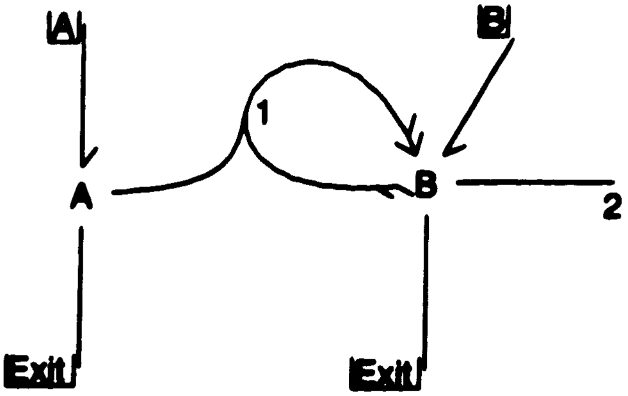

Fig. 4 Network diagram of the Gray-Scott network.

Fig. 5 shows several steady state manifolds, where the logarithm of the intermediates, $A(a), B(a)$, is plotted versus five different choices of the abscissa parameters:

$$a_1 = \text{CSTR flow}, \quad a_2 = A_0, \quad a_3 = B_0, \quad a_4 = k_1, \quad a_5 = k_2.$$

All curves are plotted through the point

$\log A = -1.868 \times 10^{-4}$ $\quad \log B = -3.675$

$\log A_0 = -1.727 \times 10^{-2}$ $\quad \log B_0 = -2.310$

$\log k_0 = -2.960$ $\quad \log k_1 = 1.010$

$\log k_2 = -1.494,$

which is called point #1 to distinguish it from other points of interest.

To obtain hyperplane equations for $\log A$ and $\log B$, we measure the slopes at the point #1 on the plots. As an example, we show how an equation for $\log B$ is obtained. From Figure 5

$$s_1 = \frac{\partial \log B}{\partial \log k_0} = 1 \qquad s_2 = \frac{\partial \log B}{\partial \log A_0} = 0 \qquad s_3 = \frac{\partial \log B}{\partial \log B_0} = 1$$

$$s_4 = \frac{\partial \log B}{\partial \log k_1} = 0 \qquad s_5 = \frac{\partial \log B}{\partial \log k_2} = -1.$$

Substituting the slopes into equation (17) gives

$$\log B = \log k_0 + \log B_0 - \log k_2 + c. \tag{19}$$

Evaluating c at point #1 gives

$$c = 0.101.$$

In the non-log space, the equation is

$$B = 1.26\, k_0 B_0 k_2^{-1}. \tag{20}$$

This approximate equation for the steady state manifold is valid near point #1. It shows how the steady state concentration of species B in the region is affected by the parameters k_0, B_0 and k_2. Other abscissa parameters have no effect on B in the region. A similar treatment can be used to obtain an equation for species A.

2.4.3 Dominant extreme current approximation

Why are there linear regions in log – log plots of the steady state manifold? This can be explained by using the concept of *dominant extreme currents*. In each linear region of the steady state manifold, there exist a small number of extreme

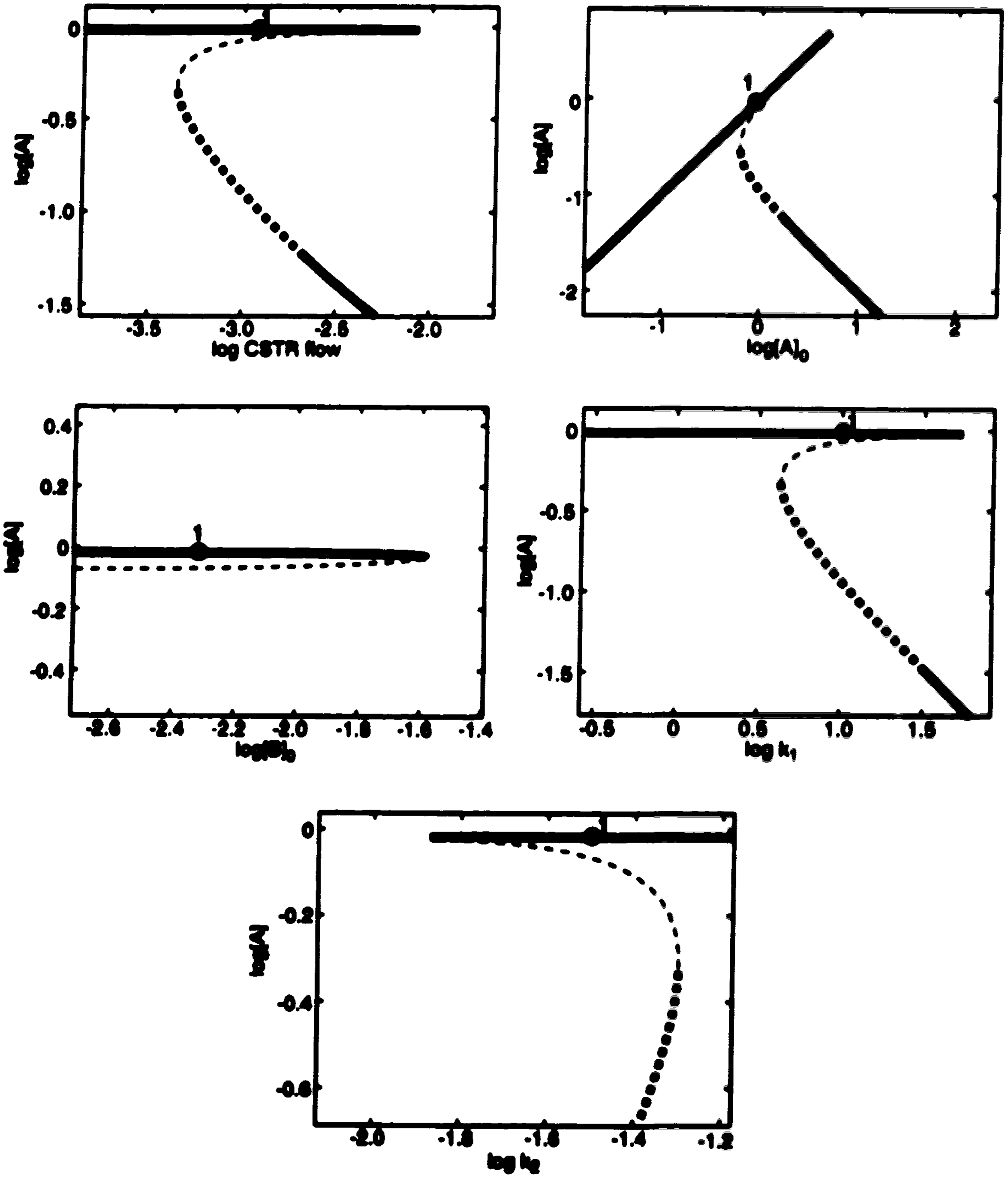

Fig. 5 Cross-sections through the steady state manifold of the Gray-Scott network. Five different abscissa parameters are shown. All cross-sections pass through the point #1 (large dot) mentioned in the text. Line patterns represent various stability properties of the steady states, which will be discussed later. More graphs on the next page.

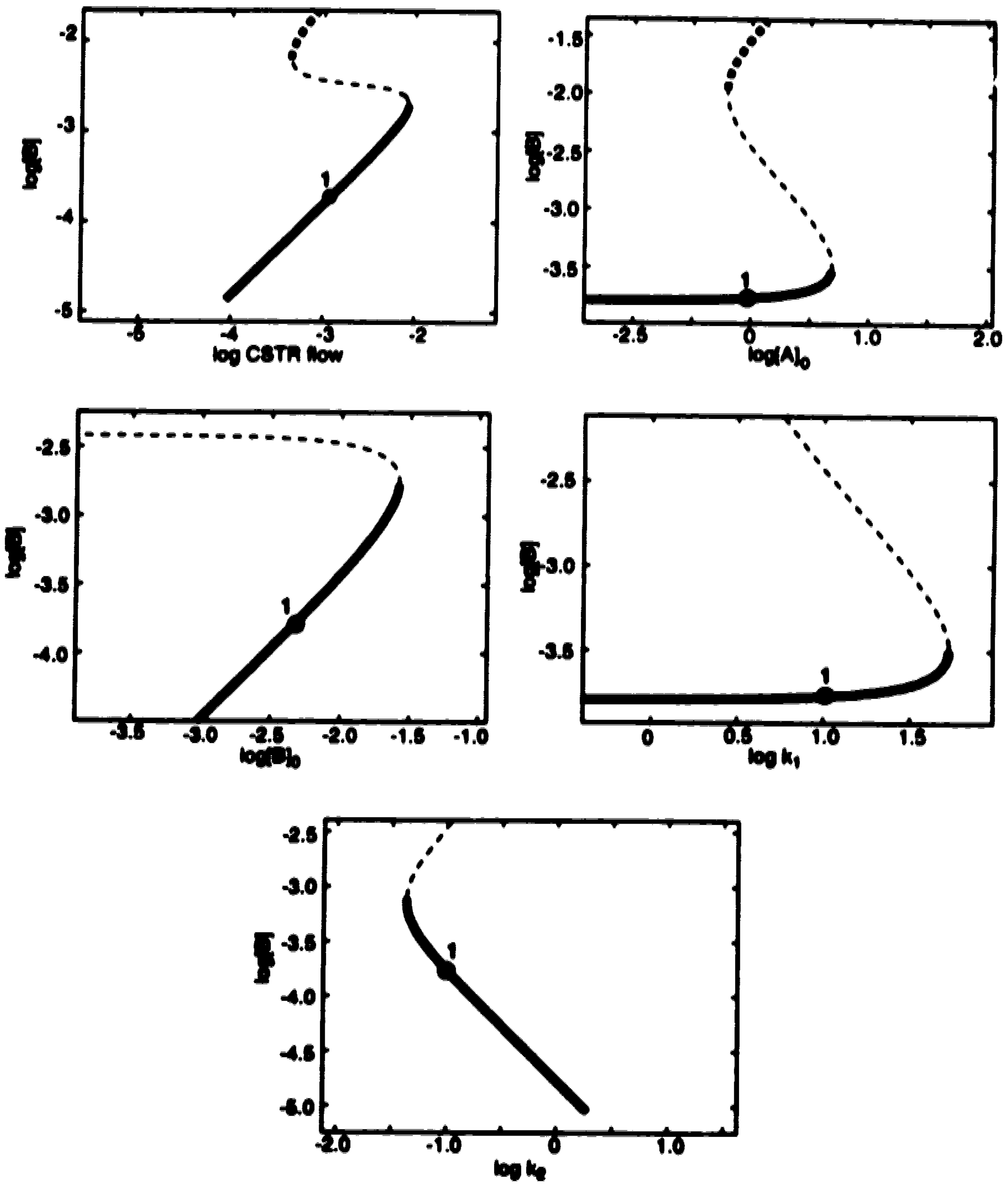

Fig. 5 Continued from the previous page

currents whose contributions to the steady states are often much bigger than other extreme currents. In some cases, one extreme current dominates in each reaction. Using only the dominant extreme current for each reaction is an approximation which can greatly simplify treatment of the network and produce approximate analytical solutions for the steady state manifold.

At a steady state, reaction rates $\mathbf{v}^0$ can be calculated from the $(\mathbf{h}, \mathbf{j})$ parameters using

$$\mathbf{v}^0 = \mathbb{E}\mathbf{j}$$

For the i-th reaction, the reaction rate v_i^0 is

$$v_i^0 = \sum_{l=1}^{r-d} \epsilon_{il} j_l, \tag{21}$$

where ϵ_{il} is the i-th row, l-th column element of the extreme current matrix $\mathbb{E}$; j_l is the rate of extreme current l at the steady state; and $r - d$ is the dimension of the current cone. In the dominant extreme current approximation, only the most significant contribution from a single extreme current is considered for each reaction. That is to say, only the largest term on the right-hand side of equation (21) is retained. If the largest contribution to the v_i^0 comes from the m-th extreme current, then equation (21) becomes

$$v_i^0 = \epsilon_{im} j_m,$$

Note that m depends on i. In vector form

$$\mathbf{v}^0 = \mathbb{E}^0\mathbf{j}. \tag{22}$$

where $\mathbb{E}^0$ is the *dominant extreme current matrix*, in which each row contains only one nonzero element coming from the dominant extreme current of the reaction.

The simplified equations for steady states can be expressed in terms of steady state concentrations using

$$\mathbf{E}^0\mathbf{j} = \mathrm{diag}(\mathbf{k})\mathbf{X}_0{}^{\mathbf{K}}. \tag{23}$$

If there are no conservation conditions, $n = d$, and the i-th equation of the system (23) is

$$\varepsilon_{im} j_m = k_i X_1^{\kappa_{1i}} X_2^{\kappa_{2i}} \cdots X_d^{\kappa_{di}}.$$

Note $\mathbf{K} = (\kappa_{ij})$, where κ_{ij} is the order of reaction j in X_i. Taking the logarithm gives

$$\log \varepsilon_{im} + \log j_m = \log k_i + \kappa_{1i} \log X_1 + \kappa_{2i} \log X_2 + \cdots + \kappa_{di} \log X_d,$$

and rearranging gives

$$\kappa_{1i} \log X_1 + \kappa_{2i} \log X_2 + \cdots + \kappa_{di} \log X_d - \log j_m = -\log k_i + \log \varepsilon_{im}. \tag{24}$$

The left side contains r unknowns

$$(\log X_1, \log X_2, \cdots, \log X_d, \log j_1, \log j_2, \cdots, \log j_{r-d}).$$

This system of equations has one equation for each of the r reactions. Hence, it is a system of r linear equations in r unknowns which can always be solved analytically provided the equations are independent.

2.4.4 Example: dominant extreme current approximation for steady state manifold of the Gray-Scott network

Let us take the Gray-Scott network as an example again to see the procedures for using the dominant extreme current approximation to determine analytical equations for steady state manifolds. The algorithm CORRALFRAME[46] calculated the following extreme current matrix for the Gray-Scott network,

$$\mathbb{E} = \begin{pmatrix} 1 & 0 & 0 & 1 & 0 \\ 1 & 1 & 0 & 0 & 0 \\ 0 & 0 & 1 & 0 & 0 \\ 0 & 0 & 0 & 1 & 1 \\ 1 & 0 & 1 & 1 & 0 \\ 0 & 1 & 0 & 0 & 1 \end{pmatrix}.$$

Because there are six reactions ($r = 6$) and two independent intermediates ($d = 2$), the dimension of the current cone is $r - d = 4$. Therefore, only four columns of $\mathbb{E}$ are needed to specify any one steady state.

Let us consider as an example the region of parameter space where $j_5 = 0$ and where following inequalities hold

$$j_3 > j_2 > j_1 > j_4.$$

These inequalities apply to point #1 used to illustrate the hyperplane approximation. The most important extreme current in this region is current 3. Current 4 is the least important. Therefore, keeping only the largest element for each row of the matrix $\mathbb{E}$ gives the dominant extreme current matrix

$$\mathbb{E}^0 = \begin{pmatrix} 1 & 0 & 0 & 0 & 0 \\ 0 & 1 & 0 & 0 & 0 \\ 0 & 0 & 1 & 0 & 0 \\ 0 & 0 & 0 & 1 & 0 \\ 0 & 0 & 1 & 0 & 0 \\ 0 & 1 & 0 & 0 & 0 \end{pmatrix}.$$

Substituting this matrix into equation (22) gives a ***simplified steady state reaction rate vector*** $\mathbf{v}^0$ expressed in terms of j_i,

$$\mathbf{v}^0 = (j_1, j_2, j_3, j_4, j_3, j_2)^t.$$

According to equations (22) and (23),

$$\mathbf{v}^0 = \mathbf{E}^0\mathbf{j} = \mathrm{diag}(\mathbf{k})\mathbf{X}_0{}^{\mathsf{K}}.$$

Note that the simplified steady state reaction rate vector is the left-hand side of this equation. The equation can be written explicitly in terms of $\mathbf{j}$ as follows

$$\begin{aligned} j_1 &= k_1 A B^2 \\ j_2 &= k_2 B \\ j_3 &= k_0 A \\ j_4 &= k_0 B \\ j_3 &= k_0 A_0 \\ j_2 &= k_0 B_0, \end{aligned}$$

which corresponds to the system of linear equations

$$\begin{aligned} \log A + 2\log B - \log j_1 &= -\log k_1 \\ \log B - \log j_2 &= -\log k_2 \\ \log A - \log j_3 &= -\log k_0 \\ \log B - \log j_4 &= -\log k_0 \\ -\log j_3 &= -\log(k_0 A_0) \\ -\log j_2 &= -\log(k_0 B_0) \end{aligned}$$

in the six unknowns $(\log A, \log B, \log j_1, \log j_2, \log j_3, \log j_4)$.

Solving this system gives approximate equations for the steady state manifold:

$$\log A = \log A_0$$

$$\log B = \log k_0 + \log B_0 - \log k_2$$

$$\log j_1 = \log k_1 + 2\log k_0 + \log A_0 + 2\log B_0 - 2\log k_2$$

$$\log j_2 = \log k_0 + \log B_0$$

$$\log j_3 = \log k_0 + \log A_0$$

$$\log j_4 = 2\log k_0 + \log B_0 - \log k_2.$$

The equivalent non-log equations are

$$A = A_0$$

$$B = \frac{k_0 B_0}{k_2}$$

$$j_1 = \frac{k_1 k_0^2 A_0 B_0^2}{k_2^2}$$

$$j_2 = k_0 B_0$$

$$j_3 = k_0 A_0$$

$$j_4 = \frac{k_0^2 B_0}{k_2}.$$

Comparing the expression for B with equation (20) obtained using the hyperplane approximation method, we see that the concentration expressions are almost the same except for the numerical factor. This difference is caused by keeping only one element in each row of the $\mathbf{E}$ matrix and ignoring all other elements.

If we only want to get steady state concentration expressions and are not interested in the $\log j_i$ expressions, the dominant extreme current approximation can be simplified further in many situations. We may use only two columns, which correspond to the two most important extreme currents. The dominant extreme current matrix in the above example can be constructed by considering only extreme currents 2 and 3

$$\mathbf{E}^{00} = \begin{pmatrix} 0 & 0 \\ 1 & 0 \\ 0 & 1 \\ 0 & 0 \\ 0 & 1 \\ 1 & 0 \end{pmatrix}.$$

Using the equation

$$\mathbf{E}^{00}\mathbf{j} = \mathrm{diag}(\mathbf{k})\mathbf{X}^{0^{\mathsf{K}}}$$

gives

$$j_2 = k_2 B$$

$$j_3 = k_0 A$$

$$j_3 = k_0 A_0$$

$$j_2 = k_0 B_0$$

or in log space

$$\log B - \log j_2 = -\log k_2$$

$$\log A - \log j_3 = -\log k_0$$

$$-\log j_3 = -\log(k_0 A_0)$$

$$-\log j_2 = -\log(k_0 B_0)$$

Eliminating $\log j_2$ and $\log j_3$ produces the expressions for $\log A$ and $\log B$ obtained previously.

In this section, I have used the region near point #1 as an example to show the procedure for deriving approximate steady state equations. The same procedure can also be applied to other regions of the steady state manifold. In fact, it is a necessary step to divide the whole steady state manifold into many small regions and apply the procedure to all the regions in order to derive equations for stability boundaries. This subject will be discussed in detail in chapter IV.

III. Steady state bifurcations and stability boundaries

Steady states are states at which the rates of concentration change for all dynamic intermediates are zero. In experiments, some steady states may be extremely vulnerable to small perturbations in experimental conditions and may never be achieved. Such steady states are unstable. We want to divide parameter space into regions where steady states exhibit different stability behaviour, and to find how the dynamical features of reaction networks change with experimental $(\mathbf{k}, \mathbf{C})$ parameters or $(\mathbf{h}, \mathbf{j})$ parameters. This chapter uses Hurwitz determinants to analyze the stability of steady states. I will also introduce mathematical ideas based on the Routh array and Orlando's theorem. They will be used to calculate stability boundaries which have very interesting structures. They can also help explain dynamical features of chemical reaction networks.

3.1 Stability of steady states

3.1.1 Characteristic equations, eigenvalues and stability

A steady state is *stable* if there is an arbitrarily small region containing the steady state with the property that all trajectories that start within the region remain within this region forever. Otherwise the steady state is *unstable*. It is *asymptotically stable* if all such trajectories return to the steady state. In this thesis, for simplicity, the word 'stable' will be used to mean 'asymptotically stable' unless otherwise indicated.

For a chemical reaction network, if all possible steady states for all parameter values are stable, we say that the network is a *stable network*. A network is an *unstable network* if there are parameter values for which unstable steady states are present.

The dynamics of concentration vector $\mathbf{X}$ near a steady state $\mathbf{X}_0$ can be linearized near the steady state as

$$\frac{d\Delta\mathbf{X}}{dt} = \mathbf{M}\Delta\mathbf{X} + \cdots \tag{25}$$

where $\Delta\mathbf{X} = \mathbf{X} - \mathbf{X}_0$, and the Jacobian matrix $\mathbf{M}$ has the form[37]

$$\mathbf{M} = \mathbf{N}\mathrm{diag}(\mathbf{v}^0)\mathbf{K}^t\mathrm{diag}(\mathbf{X}_0^{-1}). \tag{26}$$

The characteristic equation of the Jacobian matrix is

$$|\mathbf{I}\lambda - \mathbf{M}| = \alpha_0\lambda^n + \alpha_1(\mathbf{p})\lambda^{n-1} + \cdots + \alpha_{n-1}(\mathbf{p})\lambda + \alpha_n(\mathbf{p}) = 0.$$

If there exist some conservation conditions, the stoichiometric matrix $\mathbf{N}$ will have only d linearly independent rows ($d < n$). Accordingly, there are $n - d$ constants of the motion and $n - d$ zero eigenvalues that correspond to changes in these constants of the motion. The last $n - d$ coefficients of the characteristic equation vanish identically, i.e.

$$\alpha_{d+1}(\mathbf{p}) = \alpha_{d+2}(\mathbf{p}) = \ldots = \alpha_n(\mathbf{p}) = 0.$$

Factoring λ^{n-d} out of the characteristic equation gives a polynomial of order d having α_d as the constant term. The characteristic equation becomes

$$|\mathbf{I}\lambda - \mathbf{M}| = \alpha_0\lambda^d + \alpha_1(\mathbf{p})\lambda^{d-1} + \cdots + \alpha_{d-1}(\mathbf{p})\lambda + \alpha_d(\mathbf{p}) = 0. \tag{27}$$

If there are no conservation conditions, $d = n$. Equation (27) is still valid.

The solutions of this equation are the eigenvalues of $\mathbf{M}$. They determine the stability of the steady state designated by the parameter $\mathbf{p}$. When all the eigenvalues have negative real parts, the corresponding steady state is asymptotically stable. When one or more eigenvalues have positive real parts, the steady state is unstable. The situation where the largest eigenvalue has a zero real part is more complicated. It is the transition situation between stable and unstable steady states. The transition occurs on the stability boundaries (or bifurcation sets) which are the subject of this research.

The eigenvalues are determined by the coefficients in the characteristic equation, which are functions of the parameter set $\mathbf{p}$. When $(\mathbf{k}, \mathbf{C})$ parameters are used, the coefficients often cannot be expressed in terms of the parameters using a linear formula. This makes it impossible to analyze steady states analytically. Only numerical approaches can be used. When $(\mathbf{h}, \mathbf{j})$ parameters are employed, the coefficients of the characteristic equation are polynomials in the $(\mathbf{h}, \mathbf{j})$ parameters. Stability analysis can then be conducted analytically. Because of the complexity of the calculation, the analysis must be done on a computer using symbolic algebra.

There is an efficient method for identifying unstable steady states quickly. The method is based on the necessary condition for stable steady states[47]. If one of the steady states for a parameter set $\mathbf{p}$ is stable and not in the transition situation, all coefficients in the characteristic equation must be positive. So, if any coefficients are missing ($= 0$) or negative (< 0), the steady state is either unstable or in the transition situation. If any coefficient is negative, the steady state is unstable.

3.1.2 Hurwitz determinants and stability

The necessary condition for stability is not sufficient. It only helps identify some of the unstable steady states. It cannot identify stable steady states. Necessary and sufficient conditions for stability can be expressed by using the Hurwitz determinants.

The *Hurwitz determinants*[48,49] are defined as

$$\Delta_1 = \alpha_1, \qquad \Delta_2 = \begin{vmatrix} \alpha_1 & \alpha_3 \\ \alpha_0 & \alpha_2 \end{vmatrix}, \qquad \Delta_3 = \begin{vmatrix} \alpha_1 & \alpha_3 & \alpha_5 \\ \alpha_0 & \alpha_2 & \alpha_4 \\ 0 & \alpha_1 & \alpha_3 \end{vmatrix}$$

$$\Delta_d = \begin{vmatrix} \alpha_1 & \alpha_3 & \alpha_5 & \cdots & \alpha_{2d-1} \\ \alpha_0 & \alpha_2 & \alpha_4 & \cdots & \alpha_{2d-2} \\ 0 & \alpha_1 & \alpha_3 & \cdots & \alpha_{2d-3} \\ \vdots & \vdots & \vdots & \ddots & \vdots \\ 0 & 0 & 0 & \cdots & \alpha_d \end{vmatrix} \tag{28}$$

where $\alpha_k = 0$ if $k > d$ or $k < 0$; $\alpha_0, \alpha_1, \ldots, \alpha_d$ are the coefficients of the characteristic equation.

The (i, j)-th element of the Δ_d can be expressed as

$$\Delta_d(i, j) = \alpha_{2j-i} \tag{29}$$

and $\alpha_{2j-i} = 0$ whenever $2j - i > d$ or $2j - i < 0$.

All eigenvalues have negative real parts if and only if all Hurwitz determinants are positive. Hence, steady states whose Hurwitz determinants are all positive are stable; steady states that have any negative Hurwitz determinants are unstable.

3.1.3 Liénard-Chipart stability criteria

The Liénard-Chipart stability criteria[47] give stability conditions based on combinations of α's and Δ's. They eliminate the necessity of calculating all the Δ's in order to determine the stability. The *Liénard-Chipart stability criteria* can be stated as follows:

The necessary and sufficient conditions for the real polynomial

$$f(\lambda) = \alpha_0\lambda^d + \alpha_1\lambda^{d-1} + \cdots + \alpha_d \qquad (\alpha_0 > 0)$$

to have only roots with negative real parts may be expressed in any one of the four following forms:

- a) $a_d > 0, \quad a_{d-2} > 0, \cdots; \quad \Delta_1 > 0, \quad \Delta_3 > 0, \cdots$
- b) $a_d > 0, \quad a_{d-2} > 0, \cdots; \quad \Delta_2 > 0, \quad \Delta_4 > 0, \cdots$
- c) $a_d > 0, \quad a_{d-1} > 0, \quad a_{d-3} > 0 \cdots; \quad \Delta_1 > 0, \quad \Delta_3 > 0, \cdots$
- d) $a_d > 0, \quad a_{d-1} > 0, \quad a_{d-3} > 0 \cdots; \quad \Delta_2 > 0, \quad \Delta_4 > 0, \cdots.$

Steady states that satisfy any of the Liénard-Chipart criteria are stable.

3.1.4 The first column of the Routh array

Sign variations in the first column of an array called the *Routh array*[47] determine the stability of steady states. The first column of the Routh array is a sequence of numbers $(A_0, B_0, C_0, D_0, \cdots)$. The numbers can be calculated from the Hurwitz determinants

$$A_0 = a_0, \qquad B_0 = \Delta_1, \qquad C_0 = \frac{\Delta_2}{\Delta_1}, \qquad D_0 = \frac{\Delta_3}{\Delta_2} \qquad \cdots$$

Therefore, the first column of the Routh array can be written using Hurwitz determinants

$$(1, \Delta_1, \frac{\Delta_2}{\Delta_1}, \frac{\Delta_3}{\Delta_2}, \cdots, \frac{\Delta_d}{\Delta_{d-1}}) \tag{30}$$

when $A_0 = a_0 = 1$.

For non-singular cases, number of characteristic roots with positive real parts equals the number of sign changes in the first column of the Routh array. Therefore, if all numbers in the above sequence are positive, the steady state is stable because there will be no characteristic roots with positive real parts. The steady state is unstable if any one of the numbers in the sequence is negative.

The principal reason for the importance of the first column of the Routh array is that it can help identify various kinds of instability. This subject is discussed in the next section.

3.2 Steady state bifurcations and stability boundaries

3.2.1 Steady state bifurcations and stability boundaries

Steady state bifurcation is a crucial concept relating to stability boundaries. A *bifurcation* means a qualitative change in system behaviour. For steady state manifolds, if a parameter change causes a qualitative change of dynamic behaviour, then we say that a bifurcation has occurred. If the qualitative change in the dynamics occurs close to a steady state, the bifurcation is said to be *local* and is a *steady state bifurcation*. Otherwise the bifurcation is *global*.

The qualitative change in the dynamics could be a stable steady state becoming unstable or a single steady state becoming multiple steady states, and so on. The point in parameter space where the bifurcation occurs is called a *bifurcation point*. The set of bifurcation points constitutes a *bifurcation set*. The bifurcation set for local bifurcations is called the *steady state stability boundary*.

There are two typical steady state bifurcations (stability boundaries) for chemical reaction networks. One is the *saddle-node bifurcation* (SN)[50-52] where two steady states coalesce and disappear. The SN bifurcation appears as a fold of a steady state manifold. Steady states on one branch of the fold are unstable saddle points and are not achievable experimentally. The saddle-node bifurcation is mainly responsible for the bistability between two steady states and for the hysteresis, which is caused by the existence of bistability, observed in chemistry laboratories. Another bifurcation is the *Hopf bifurcation* (Hopf)[50-52] where a stable steady state (a stable focus) loses its stability and changes into an unstable steady state (an unstable focus) surrounded by a periodic solution of limit cycle. Hopf bifurcations are the main reason for chemical oscillations observed in experiments.

3.2.2 General equations for stability boundaries

Saddle-node bifurcation is caused by one real eigenvalue passing through zero when some parameter value is changed. The eigenvalue equals zero on the hypersurface in parameter space where the bifurcation occurs.

The characteristic equation (27) shows that when a real eigenvalue equals zero, the constant term α_d must also equal zero. When α_d equals zero,

$$\begin{aligned} &\alpha_0\lambda^d + \alpha_1(\mathbf{p})\lambda^{d-1} + \cdots + \alpha_{d-1}(\mathbf{p})\lambda \\ &= \lambda\{\alpha_0\lambda^{d-1} + \alpha_1(\mathbf{p})\lambda^{d-2} + \cdots + \alpha_{d-1}(\mathbf{p})\} \\ &= 0. \end{aligned}$$

Then one of the eigenvalues must be zero. Therefore, a saddle-node bifurcation happens if and only if $\alpha_d = 0$.

Combining the above analysis with the steady state definition shown in equation (2), we can write the general equations for the saddle-node bifurcation hypersurfaces

$$\mathbf{N}\mathbf{v}^0 = 0 \qquad \alpha_d = 0. \tag{31}$$

A Hopf bifurcation occurs when a pair of complex conjugate eigenvalues goes across the imaginary axis simultaneously. At a Hopf bifurcation point, real parts of the pair of conjugate complex eigenvalues vanish and the eigenvalues are imaginary.

The location of the Hopf bifurcation hypersurfaces can be calculated using Hurwitz determinants. The theoretical basis is Orlando's theorem[47,53], which states that

$$\Delta_{d-1} = (-1)^{\frac{d(d-1)}{2}} \alpha_0^{d-1} \prod_{j<k}^{1,\ldots,d} (\lambda_j + \lambda_k) \qquad (d \geq 2)$$

where the $\lambda_i (i = 1, 2, \cdots, d)$ are the eigenvalues or roots of the characteristic equation (27), and the product is taken over all pairs of eigenvalues. Hence, $\Delta_{d-1} = 0$ if and only if there is at least one pair of eigenvalues whose sum is zero.

At a Hopf bifurcation point, there is a pair of pure imaginary eigenvalues. Since their sum equals zero, Orlando's theorem says $\Delta_{d-1} = 0$. On the other hand, because one side of the Hopf bifurcation is a stable region, all stability conditions are satisfied. So, $\Delta_{d-1} > 0$. Therefore, the equations for the Hopf bifurcation hypersurface are

$$\mathbf{N}\mathbf{v}^0 = 0 \qquad \Delta_{d-1} = 0 \tag{32}$$

with the restriction that all other stability conditions are satisfied. This means all other

$$\Delta_i > 0 \qquad i = 1, 2, \cdots, d-2, d$$

or any one of the Liénard-Chipart criteria excluding $\Delta_{d-1} > 0$ is satisfied.

All Hopf bifurcation hypersurfaces satisfy equation (32), but not all points satisfying equation (32) are on Hopf bifurcation hypersurfaces. In other words, Δ_{d-1} equals zero at all Hopf bifurcation points, but not all points at which Δ_{d-1} equals zero are Hopf bifurcation points. This is because cancellation of a pair of eigenvalues does not necessarily happen on the imaginary axis. When one or more eigenvalues lie to right half of the complex plane, it is possible that another eigenvalue in left half of the complex plane has the same absolute value but is opposite in sign to a right-half plane eigenvalue. The cancellation of this pair of eigenvalues also causes

$\Delta_{d-1} = 0$ according to the Orlando's theorem. One kind of hypersurface produced by this cancellation gives us very useful information on geometrical structures of stability boundaries. It will be called the *symmetrical eigenvalue hypersurfaces* (SE) and be discussed later.

3.2.3 Numerical calculation of stability boundaries

Equations (31) and (32) have been used to calculate stability boundaries numerically. The algorithm is a 2-parameter numerical continuation method which is similar to that used for the numerical calculation of steady state manifolds discussed in section 2.3. We use one more parameter. Continuation methods had not previously been developed for the calculation of stability boundaries. My method is based on the explicit equations for stability boundaries. It is conceptually clear and straight forward.

Besides the algorithm used in calculation of steady state manifold, there are two more issues to be addressed for the calculation of stability boundaries.

One is the determination of a starting point for the two parameter continuation. The objective is to find a point on the steady state manifold where the number of eigenvalues with positive real parts changes. For the Hopf bifurcations, this number changes from zero to two. For the SN bifurcations, the number changes from zero to one.

According to the theory introduced in section 3.1.4, the sign pattern for the first column of the Routh array is

$$(+, +, \dots, +, +)$$

for a stable region. This ensures that all eigenvalues have negative values only. When a point goes across a SN point, a sign change in α_d causes the sign of Δ_d to change because $\Delta_d = \Delta_{d-1}\alpha_d$. The sign pattern for the above sequence becomes

$$(+, +, +, +, \cdots, +, +, -).$$

There is one sign change in the above sequence. When a point goes across a Hopf point, the Δ_{d-1} changes sign. The sign pattern becomes

$$(+, +, +, +, \cdots, +, -, +).$$

There are two sign changes in the sequence.

To find a starting point for the 2-parameter continuation, the first column of the Routh array is calculated numerically at each point on the steady state manifold. By counting number of sign changes at each point, the SN and Hopf bifurcation points may be found. These can be used as starting points for calculating stability boundaries.

The second issue is the difficulty in handling the large numerical values of the Hurwitz determinants for certain parameter values of large experimental networks. The numbers can easily overflow the machine limit without proper handling. A solution is to reduce the magnitude of the Hurwitz determinants while keeping their signs unchanged. The mathematical justification is

$$\Delta_i = \begin{vmatrix} \alpha_1 & \alpha_3 & \alpha_5 & \cdots & \alpha_{2i-1} \\ \alpha_0 & \alpha_2 & \alpha_4 & \cdots & \alpha_{2i-2} \\ 0 & \alpha_1 & \alpha_3 & \cdots & \alpha_{2i-3} \\ \vdots & \vdots & \vdots & \ddots & \vdots \\ 0 & 0 & 0 & \cdots & \alpha_i \end{vmatrix} = p^i \begin{vmatrix} \alpha'_1 & \alpha'_3 & \alpha'_5 & \cdots & \alpha'_{2i-1} \\ \alpha'_0 & \alpha'_2 & \alpha'_4 & \cdots & \alpha'_{2i-2} \\ 0 & \alpha'_1 & \alpha'_3 & \cdots & \alpha'_{2i-3} \\ \vdots & \vdots & \vdots & \ddots & \vdots \\ 0 & 0 & 0 & \cdots & \alpha'_i \end{vmatrix} = p^i \Delta'_i.$$

Since Δ_i and Δ'_i change signs at the same time, we can use a smaller Δ'_i to replace the larger Δ_i by reducing the α_i to $\alpha'_i = \alpha_i/p$. The factoring constant p can be set according to specific needs. A good choice of p is

$$p = 10^{\frac{\sum_{i=1,\alpha_i \neq 0}^{d} \log|\alpha_i|}{d}}.$$

If necessary, the original Δ_i value can be calculated from Δ_i' using

$$\log \Delta_i = i \log p + \log \Delta_i'.$$

3.3 *Structures of stability boundaries*

3.3.1 Symbols for marking stability regions

A point on a steady state manifold lies in a *saddle node region* if $\alpha_d < 0$. When the folding of the steady state manifold produces multiple steady states, saddle node regions are interleaved between non-saddle node regions. We propose to mark all non-saddle node regions with symbols which are stacked above one another in the proper order. The number of symbols in a stack tells us how many non-saddle node region steady states were produced by the folding.

There are two types of non-saddle node region steady states. One type is stable and will have various symbols to classify it as "upper" or "lower". The second type is unstable and lies in a *Hopf region* where $\Delta_i < 0$ for $i = 1, 2, \cdots, d-1$. The possibilities with one or two non-saddle node region steady states are given in Figure 6.

If the Hopf bifurcation is supercritical, a limit cycle attractor is usually associated with every steady state in a Hopf region. The region of oscillation corresponds exactly to the Hopf region. In this situation, the Hopf region symbol (a circle with horizontal line) is replaced by a limit cycle oscillation symbol (a circle).

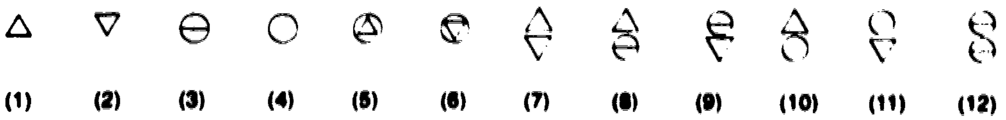

Fig. 6 Symbols used to mark stability regions. Their meanings are: (1) unique upper stable steady state (sss) ; (2) unique lower sss; (3) Hopf region state; (4) oscillatory state; (5) coexistence of upper sss and its surrounding oscillatory state; (6) coexistence of lower sss and its surrounding oscillatory state; (7) bistability between two stable steady states; (8) coexistence of upper sss and lower Hopf region state; (9) coexistence of upper Hopf region state and lower sss; (10) coexistence of upper sss and lower oscillatory state; (11) coexistence of upper oscillatory state and lower sss; (12) coexistence of upper Hopf region state and lower Hopf region state.

When a Hopf bifurcation is subcritical, a limit cycle can coexist with a stable steady state without folding the steady state manifold. This situation is represented by a circle which surrounds a stable steady state symbol. This convention enables us to indicate the presence of two attractors without stacking symbols. Thus, the number of stacked symbols still indicates the number of non-saddle node region steady states produced by the folding of steady state manifold.

3.3.2 Structural elements of stability boundaries

All calculated and experimental stability boundaries are composed of structural elements. *Structural elements* include pieces of stability boundaries, structural centres and cusp points on the stability boundaries. Structure elements are hypersurfaces in a multi-dimensional parameter space and are line segments or points in normal two-dimensional subspaces. I will illustrate the ideas for two-dimensional stability boundaries.

Phase diagram stability boundaries can contain roughly six different types of structural elements. Among them, saddle node (SN), saddle node plus (SN^+), and Hopf are all pieces of stability boundaries. Symmetrical eigenvalue (SE) curves are special structure elements whose meaning will become clear later. Double zero (DZ) points are structural centres. Cusp points are second order singular points on the steady state manifold. Different arrangements and organizations among these structural elements can produce many different types of phase diagrams, which can be understood in terms of these structural elements and their relationships to each other.

Section 3.2.2 discussed equations for saddle node bifurcation hypersurfaces. These include two subcases called SN and SN^+ bifurcations. A SN bifurcation is a boundary between stable steady states and unstable saddle-shaped steady states. Geometrically they are folding points between a stable branch and an unstable branch. At a SN point, all eigenvalues have negative real parts except one eigenvalue equals zero. Since one side of a SN point is a stable region, all stability conditions must hold except $\alpha_d = 0$ at the SN point. A SN^+ is similar to a SN in that it is also a geometrical folding point and it obeys the same equation $\alpha_d = 0$. However, a SN^+ point also has a real positive eigenvalue. Steady states on both sides of a SN^+ are unstable.

The difference between a SN and a SN^+ can be seen from Fig. 7. On the figure, there is a SN point between the upper branch and the middle branch. On one side of the SN point, all steady states on the upper branch are stable. All Δ's are positive, all numbers in the first column of the Routh array are positive and hence all eigenvalues have negative real parts. When a point A on the upper branch approaches the SN point along the curve, the positive α_d at the point A becomes smaller and smaller until it reaches zero at the SN point. Since $\Delta_d = \alpha_d \times \Delta_{d-1}$ while Δ_{d-1} is still greater than zero at the SN, the Δ_d becomes zero at the SN and becomes a negative number after the point A gets into the middle branch. The sign pattern of the Hurwitz determinants changes to $(+,+,\ldots,+,+,-)$ and the first column of the Routh array also becomes $(+,+,\ldots,+,+,-)$, which means that one eigenvalue has become positive.

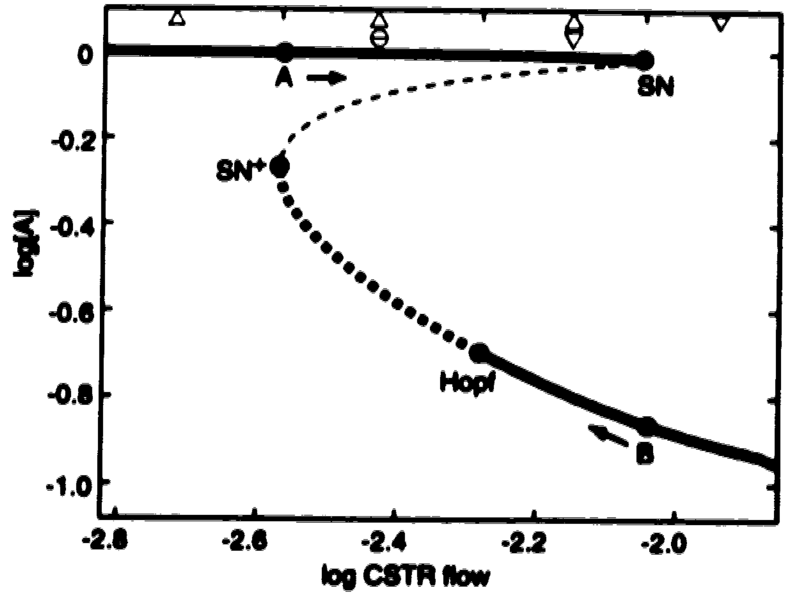

Fig. 7 SN and SN^+ bifurcation points. In addition to negative eigenvalues, there is only one zero eigenvalue at a SN point, but there are one zero eigenvalue AND one positive eigenvalue at a SN^+ point. (The graph is calculated using the Gray-Scott network.)

There is also a SN^+ point on the same graph. It occurs between the lower branch and the middle branch of the fold. Both sides of the SN^+ point are unstable regions. When a point B on the lower branch moves from the stable region on the far-right part of the lower branch toward the SN^+ point, it first passes through a Hopf point where $\Delta_{d-1} = 0$. After passing this point, a pair of conjugate complex eigenvalues changes signs of their real parts to positive numbers. The pair of eigenvalues then approaches the real axis from opposite directions until their imaginary parts become zero. The pair of complex conjugates becomes two real eigenvalues. One of the eigenvalues approaches zero moving along the curve towards the SN$^+$. It becomes zero at the SN$^+$ while the other eigenvalue is still positive. At the SN$^+$ point, $\alpha_d = 0$ while at least one $\Delta_i < 0$, for $i = 1, \ldots, d-1$. After the point gets into the middle branch, there is only one positive eigenvalue and only one sign change in the first column of the Routh array.

The difference between a Hopf and a SE point is illustrated in Fig. 8. In Fig. 8(a), the Hopf point is a point where all Hurwitz determinants are positive except $\Delta_{d-1} = 0$. α_d is also positive at a Hopf point. Imagine that we can move the Hopf point toward the fold and let it pass through the SN$^+$ point. Then it becomes the point SE in Fig. 8(b). When we check the signs of Δ_{d-1} starting from the stable region on the lower-left part of the curve, we find that the Hopf or the SE point is the first occurrence of $\Delta_{d-1} = 0$ in both cases. The difference is that $\alpha_d > 0$ at a Hopf point and $\alpha_d < 0$ at a SE point.

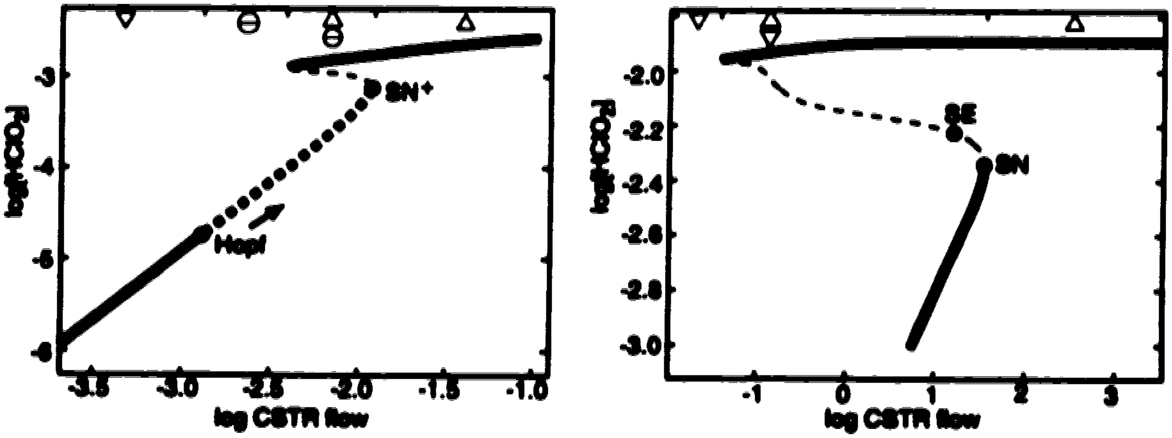

(a)

(b)

Fig. 8 Hopf and SE points. (a) $\alpha_d > 0$ at a Hopf point; (b) $\alpha_d < 0$ at a SE point. After a Hopf point moves across a SN$^+$ point, it becomes a SE point and the SN$^+$ becomes a SN point. (The graph is calculated using the chlorite-iodide network[34].)

Double zero points (DZ), also known as *Takens-Bogdanov points*[26,54–55], are codimension 2 bifurcations where two eigenvalues are simultaneously zero. They are the hypersurfaces which are one dimension lower than stability boundaries in a general multi-dimensional space. As I will explain in the following sections, they are places where different types of stability boundaries meet. Using a DZ point as a centre, SN, SN$^+$ and Hopf curves form Y-shaped structures. A DZ point is also the crossing point of a curve composed of (SN,SN$^+$) bifurcations and a curve composed of (Hopf,SE) bifurcations. SN and SN$^+$ curves join at DZ points. Similarly, Hopf and SE curves join at DZ points.

Cusp points are higher order singular points on the stability boundaries. Three steady states collapse to one steady state and the fold disappears at a cusp point. It is seen as a tip or a sharp turning point on stability boundary or phase diagrams.

Fig. 9 gives a summary of the relationships between Hopf, SE, SN, SN$^+$ and DZ hypersurfaces when the steady state manifold is flattened out in the $(\mathbf{h}, \mathbf{j})$ space. At the left is the Hopf region which is defined as the region where some $\Delta_i < 0$ for $i = 1, \ldots, d-1$. At the right is the region where $\alpha_d < 0$. Outside these regions the steady states are stable and inside they are unstable. Thus, the boundary of the combined region separates stable and unstable steady states with Hopf and SN bifurcation curves as marked on the figure. When the Hopf region overlaps the region where $\alpha_d < 0$, DZ points and two new curves called the SN$^+$ curve and the SE curve appear. The SE curve is the subset of the boundary of the Hopf region where $\Delta_i < 0$ for some $i = 1, \ldots, d-1$, which lies in the region $\alpha_d < 0$. Note that the SE curve is the continuation of the Hopf bifurcation boundary inside the set $\alpha_d < 0$.

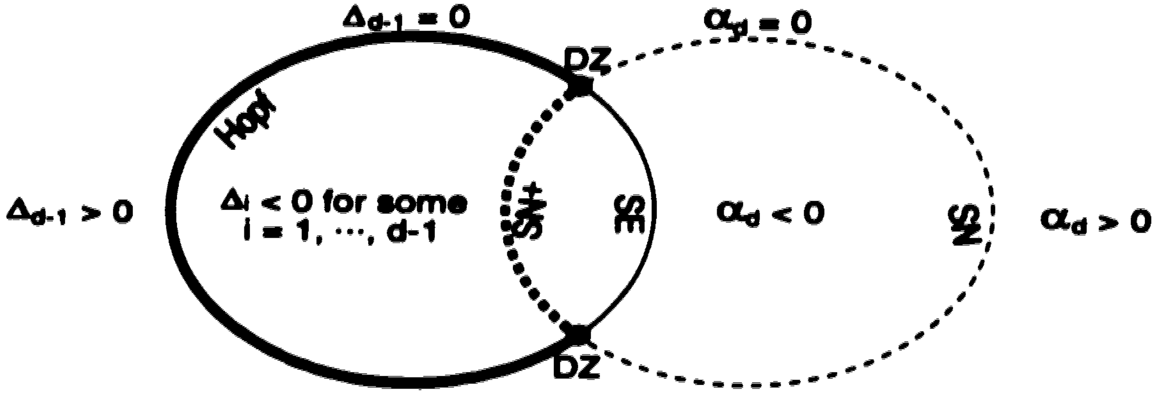

Fig. 9 Relationships between Hopf, SE, SN, SN$^+$ and DZ hypersurfaces. The relationships as shown here are valid inside the steady state manifold when it is flattened out in the $(\mathbf{h}, \mathbf{j})$ space.

These structural elements will enable us to understand most theoretical and experimental stability boundaries or phase diagrams. The bifurcation structures revealed by these diagrams are very useful information for explaining experimental results and exploring reaction mechanisms.

3.3.3 Y-shaped structures formed by SN, SN$^+$ and Hopf curves

The Y-shaped structures mentioned in the last section are formed by SN, SN$^+$ and Hopf curves. There are two types of Y-shaped structures shown in Fig. 10 and Fig. 11.

Fig. 10(a) represents one type of steady state manifold near a DZ point. An unstable region exists between the Hopf point and the SN$^+$ point on the graph. If a second parameter is changed, the unstable region can become either larger or smaller depending on the direction of the parameter change. If the unstable region gets smaller, we can imagine that the net effect of changing the second parameter is to push the Hopf point toward the SN$^+$ point. When the Hopf meets the SN$^+$

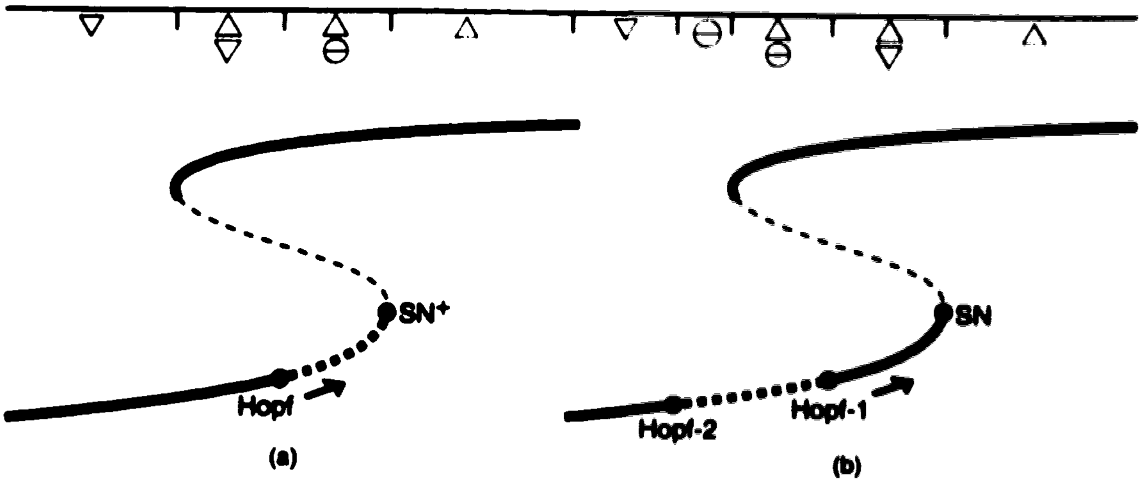

Fig. 10 Steady state manifolds near the Y-shaped structures. (a) near a type I Y-structure; (b) near a type II Y-structure.

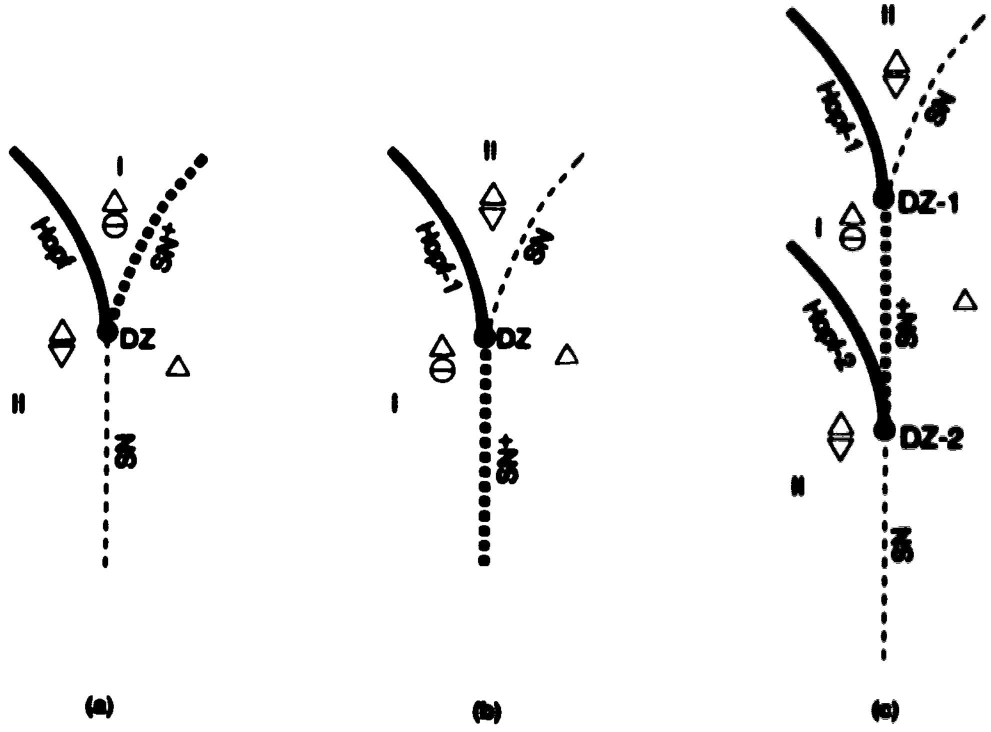

Fig. 11 The topological Y-shaped structures. (a) the type I Y-structure; (b) the type II Y-structure; (c) a combination of type I and type II structures.

at the folding point, two eigenvalues equal zero and this is a DZ point. At the DZ point, both Δ_{d-1} and a_d are zero. If we push the Hopf point further, it will become a SE point and the SN^+ point changes into a SN point. Stability boundaries formed this way appear Y-shaped and are shown in Fig. 11(a). On the graph, the first and the second parameters are plotted as horizontal and vertical axes respectively. We call this Y-shaped structure the *type I Y-structure*. In parameter space, the region between the Hopf and the SN^+ curves (region I in Fig. 11(a)) within the type I Y-structure is the region where oscillations could be found. If the Hopf bifurcation is supercritical, region I is the only possible oscillatory region. The region on the left side of the Hopf and the SN curves is named region II on the graph. This is the region where bistability is usually found. If the Hopf bifurcation is subcritical, it is also possible to find oscillations on the upper part (the part where the second parameter is higher than that of the DZ point) of the region. The oscillations could coexist with one or two stable steady states. Real final states of the system are determined by initial system states in these situations.

Fig. 10(b) represents another type of steady state manifold near a DZ point. On the lower branch of the curve, there is an unstable region between two Hopf bifurcation points marked 'Hopf-1' and 'Hopf-2'. There is also a SN point between the middle and the lower branches. When we push the point Hopf-1 toward the SN point by changing a second parameter (the position of the Hopf-2 point may also change at the same time, but we do not consider this change at the moment), the region between the Hopf-1 and the SN points becomes smaller and smaller. Eventually the Hopf-1 and the SN points will coincide and a DZ point is formed. Pushing the Hopf-1 point even further will produce a SN^+ point. The stability boundaries formed this way also possess a topological Y-shaped structure shown in Fig. 11(b). This is the *type II Y-structure*. Notice that the regions I and II in Fig. 11(a) have exchanged their positions in Fig. 11(b).

After the Y-structure in Fig. 11(b) is obtained, if the point Hopf-2 in Fig. 10(b) is pushed toward the SN$^+$ by changing the second parameter, another Y-structure of type I will be formed. The combination of the two Y-structures gives stability boundaries shown in Fig. 11(c). The unstable regions caused by the two combined Y-structures are marked II, I, II respectively. The region number I and II have the same meaning as I discussed above. The symbols DZ-1 and DZ-2 indicate two DZ points.

Fig. 11 is a qualitative illustration of the topological Y-shaped structures. For a specific network and some specified parameters, real shapes of the Y-structures could be bent. Slopes of the curves could also be different from that shown in the figure. But the topological structures are always held.

Y-shaped structures are seen on many phase diagrams. While the type I Y-structures are quite common (such as the Gray-Scott network and the SNB network to be discussed later), the type II Y-structures have also been observed in chemical networks such as the Willamowski-Rössler model[56,57]. Our research shows that in the neighbourhood of a DZ point, distance between two approaching Hopf and SN (or SN$^+$) curves are usually very small. That is to say that α_d and Δ_{d-1} become equal to zero almost simultaneously. On diagrams showing stability boundaries, they often appear to overlap on each other. But no matter how close they are, the Y-shaped structures discussed previously always exist. A grasp of the structures can help us understand experimental and theoretical results clearly.

3.3.4 DZ as the crossing point of SN, SN$^+$, Hopf, SE curves

In the previous section, we saw that a DZ point is a crossing point in the Y-shaped structures. This section shows that the symmetric eigenvalue (SE) curve also meets the DZ point. To see this, the location of the SE point could be added to Figure 10 and its location plotted on Figure 11.

After a Hopf point passes through a folding point SN or SN$^+$, it goes into the middle unstable branch of the fold and becomes a SE point. The SN or the SN$^+$ point changes into a SN$^+$ or a SN point accordingly. Further change of the second parameter will push the SE point away from the newly formed SN$^+$ or the SN point. Resulted stability boundaries look like one of the DZ point-centered (or DZ-centered) structures shown in Fig. 12.

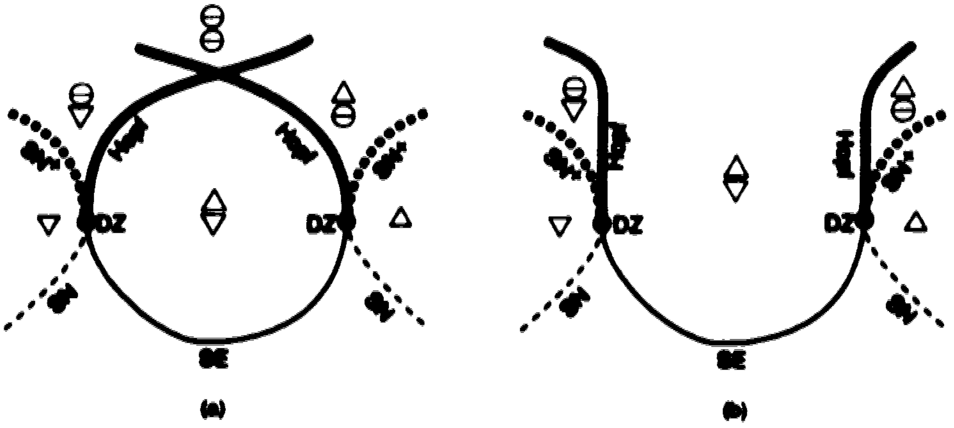

Fig. 12 One SE curve connects two DZ-centered structures. (a) Hopf curves belonging to the two DZ-centered structures cross over on a two-dimensional parameter plane; (b) The Hopf curves do not cross over on the parameter plane. Only topological structures are shown on the graphs.

Each of the two graphs in Fig. 12 contains two DZ-centered structures. Every single DZ-centered structure in Fig. 12 is composed of two curves defined by equation (31) and equation (32) without other restrictions. Using equation (31) and choosing any SN or SN$^+$ point as a starting point, we can calculate a curve composed of SN and SN$^+$ segments. Using equation (32) and choosing a Hopf point as a starting point, we can calculate a curve composed of Hopf and SE segments. These two curves meet at a DZ point. Within the steady state manifold the curves cross at the DZ point. However, because the manifold is folded along the SN-SN^+ curve the curves appear to meet tangentially rather than cross on the phase diagram.

It is not uncommon to see two such crossing structures (Y-shaped structures are part of the crossing structures) on a stability boundary or a phase diagram. The two crossing structures are often connected in one of the two ways. If there exists a cusp point on the (SN,SN^+) curve, then the (SN,SN^+) curve will be in a position of joining the two crossing structures. If no cusp points exist, the two crossings are usually connected by a SE curve, as shown in Fig. 12. The two double zero points are usually located on the upper and the lower branches of a fold, respectively. So are the two Hopf bifurcations. On a two-dimensional parameter plane, the two Hopf bifurcation curves can cross over on each other on a two-dimensional phase diagram (Fig. 12(a)). However, they really do not touch at any point since they are on different branches of a fold. It is also possible that the two Hopf curves do not cross over at all as shown in Fig. 12(b). For both cases, the two Hopf bifurcation curves are connected by a SE curve. The SE curve serves as a bridge between the two Hopf curves and between the two branches of a fold.

The SE curves shown in Fig. 12 have had a significant impact on our studies of nonlinear chemical dynamics. They reveal connections between the two crossing structures centred at two DZ points. They also connect two seemingly separated Hopf bifurcation curves. By following a SE curve, we can quickly find new bifurcation structures on new parameter regions that could be very important to the understanding of the chemical systems. Because cusp points do not always exist on a 2-dimensional phase diagram, the whole bifurcation structure could appear only in pieces without the SE curves. Since a numerical continuation method can only calculate continuous steady state manifolds or continuous stability boundaries, it could restrict our investigations only on a small piece of a bifurcation structure or only in a small region of the parameter space. The discovery of SE curves provides an effective solution to this problem.

3.3.5 Onion structure of the $\Delta_{d-1} = 0$ hypersurfaces

In a previous section, we saw that the Hopf and SE bifurcation sets are hypersurfaces of $\Delta_{d-1} = 0$ in multi-dimensional parameter space. They are curves of $\Delta_{d-1} = 0$ in a two-dimensional subspace. Actually, not all $\Delta_{d-1} = 0$ hypersurfaces are Hopf or SE bifurcation sets. The hypersurfaces can form a multi-layered structure similar to an onion.

Fig. 13 shows a representative steady state manifold containing multiple $\Delta_{d-1} = 0$ points (the curve is calculated using the SNB model[38]). Four $\Delta_{d-1} = 0$ points are marked as A, B, C and D. Among them, A and D are two points on a SE curve, which is connected to a Hopf curve at a DZ point. The points B, C also satisfy the equation $\Delta_{d-1} = 0$. But the hypersurface they belong to is different from the Hopf hypersurface. Points B and C are not a part of the SE curve defined in this thesis.

When we examine all points along a steady state manifold curve, the first and the last $\Delta_{d-1} = 0$ points are Hopf or SE points. As soon as Δ_{d-1} becomes negative after we find a Hopf or a SE point, its sign can change back into positive and change back again many times. Other Δ_i, for $i \neq d-1$, will change accordingly so that the first column of the Routh array still provides right number of sign changes. A qualitative stability boundary diagram is shown in Fig. 14. Fig. 13 that

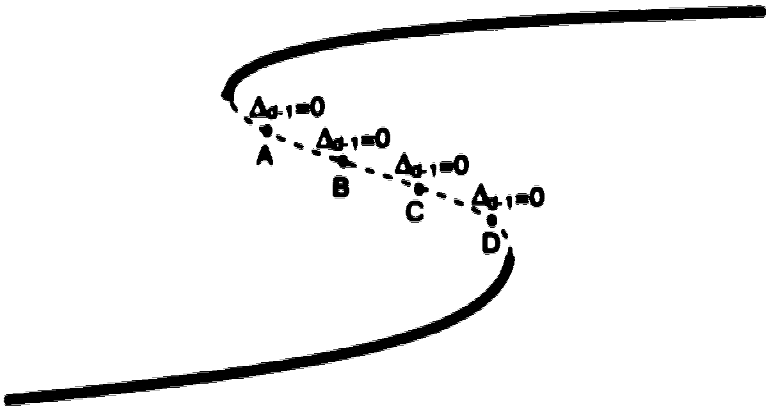

Fig. 13 A steady state manifold with multiple $\Delta_{d-1} = 0$ points. Among four such points marked by A,B,C,D, the points A and D are on the SE curve defined in this thesis while the points B,C are not.

we saw before was a steady state manifold at a cross section of Fig. 14.

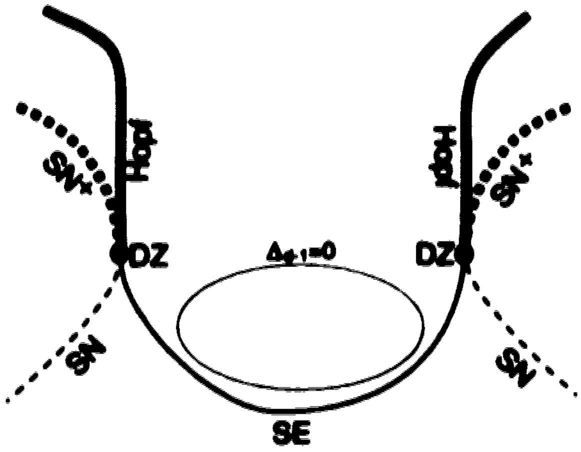

Fig. 14 A qualitative stability boundary diagram including an onion structure formed by $\Delta_{d-1} = 0$ hypersurfaces. For simplicity, only two layers of an onion structure are plotted even though a real structure may contain many more layers.

Distances between the $\Delta_{d-1} = 0$ hypersurfaces could be very small in some networks. When we calculate a steady state manifold numerically, a step size that is not small enough could make it easy for the algorithm to jump over one or more

$\Delta_{d-1} = 0$ hypersurfaces. This could lead to misinterpretations of sign changes in Δ_{d-1} along the steady state manifold. Understanding the onion structures solves this problem.

3.3.6 Stability boundaries viewed from within the steady state manifold

We have seen crossing structures of stability boundaries where a DZ point sits at the centre of a (SN,SN$^+$) curve and (Hopf,SE) curve crossing. Based on this structure, we can design a new coordinate system to describe relationships between stability boundaries, stability regions and signs of (Δ_{d-1}, α_d) pairs. In this coordinate system, the steady state manifold will be flattened so that (SN,SN$^+$) and (Hopf,SE) curves exhibit a true crossing.

Fig. 15 shows the flattened view of the steady state manifold on the coordinate system. In the first quadrant, (Δ_{d-1}, α_d) sign patterns are $(+,+)$. Steady states are all stable in this parameter region. In other quadrants, either Δ_{d-1} or α_d is negative, these are unstable regions.

The coordinate system can be used as a tool for understanding stability properties of steady states on various parts of a steady state manifold. It brings steady states, stability boundaries and signs of (Δ_{d-1}, α_d) pairs all together. For example, existence of onion-structured $\Delta_{d-1} = 0$ hypersurfaces can be presented as in Fig. 16. The steady state manifold shown in Fig. 13 is qualitatively seen as two thick solid line segments and one thin dashed line segment. The original fold has been unfolded and stabilities of steady states are clearly seen. The curve starts from the stable quadrant, goes across a SN boundary (thin-dashed part of the horizontal axis) and a SE boundary (thin-solid part of the vertical axis), then passes through another $\Delta_{d-1} = 0$ boundary in quadrant III twice. Finally it goes across the SE

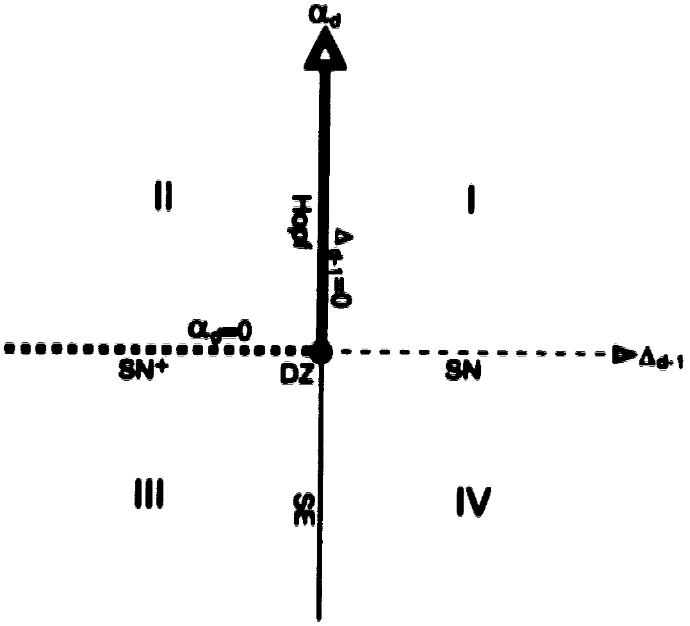

Fig. 15 Flattened view of the steady state manifold. The mapping onto a plane has been chosen such that the curve Δ_{d-1} =0 is the y-axis and the curve $\alpha_d = 0$ is the x-axis.

and the SN boundaries again and comes back to the stable quadrant.

Fig. 13 and Fig. 16 show only two layers of $\Delta_{d-1} = 0$ hypersurfaces in an onion structure. Theoretically, there may be many layers of the $\Delta_{d-1} = 0$ surfaces. The number of layers depends on the network and the parameters. Distances between the layers also vary quite substantially. When the distance between two layers is very small, extra care is needed in determining stability properties of steady states. When the distance between a SE and its closest $\Delta_{d-1} = 0$ surfaces is extremely small, it can be difficult to calculate the SE curve using a conventional numerical continuation method.

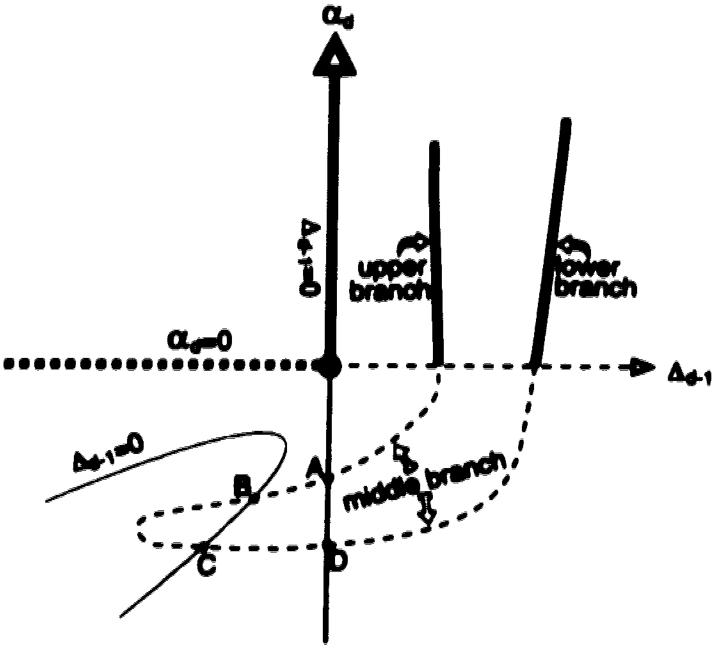

Fig. 16 Flattened view of a steady state manifold with onion-structured $\Delta_{d-1} = 0$ hypersurfaces. Meanings of elements in the coordinate system are shown in Fig. 15.

IV. Dependence of stability boundaries on experimental parameters

From both experimental and a theoretical points of view, it is very important to understand how stability boundaries are affected by various experimental parameters. As mentioned earlier, stability boundaries are hypersurfaces in a multi-dimensional parameter space. Generally speaking, it is impossible to derive analytical formulas for these boundaries in the whole parameter space because of the nonlinear nature of the stability boundaries.

The situation is not totally hopeless. After we worked with many different stability boundaries, we realized that it is possible to derive analytical formulas for many stability boundaries in specific parameter regions. These locally valid formulas can guide us in the investigation of nonlinear features. For the situations where explicit analytical formulas cannot be derived, we can use other techniques to qualitatively analyze how experimental parameters affect the stability boundaries.

In this chapter, I will discuss four methods that can be used in different situations. The first three give explicit analytical formulas for stability boundaries. The last one finds how stability boundaries shift when experimental parameters are changed. Techniques for adjusting experimental parameters to fit experimental results will be discussed.

4.1 Analytical boundaries using the hyperplane approximation

In section 2.4.1, I discussed the hyperplane approximation in log space for deriving analytical formulas of steady state manifolds. An extension of the method can yield analytical formulas for SN and SN$^+$ stability boundaries.

The key idea is based on the fact that SN and SN$^+$ hypersurfaces are at the intersections of two neighbouring branches of a fold. Therefore, the concentrations of all chemical species at a point on a SN or a SN$^+$ hypersurface must satisfy both equations for the neighbouring branches. If we already know equations for the two neighbouring branches, then moving a specific concentration variable to the left side of each equation and letting the right sides of the two equations be equal to each other will produce equations for the SN or the SN$^+$ stability boundary.

Consider the general forms of two hyperplane approximations as in Chapter 2:

$$\log \mathbf{X} = \mathbf{S}^1 \log \mathbf{a} + \mathbf{c}^1$$

$$\log \mathbf{X} = \mathbf{S}^2 \log \mathbf{a} + \mathbf{c}^2$$

where the superscripts 1 and 2 distinguish between the hyperplanes. When the two hyperplanes intersect, both equations give the same **X** so

$$\mathbf{S}^1 \log \mathbf{a} + \mathbf{c}^1 = \mathbf{S}^2 \log \mathbf{a} + \mathbf{c}^2$$

and

$$(\mathbf{S}^1 - \mathbf{S}^2) \log \mathbf{a} + (\mathbf{c}^1 - \mathbf{c}^2) = 0.$$

The resulting set of d equations places d restrictions on **a**. Since there can only be one restriction on **a** at a bifurcation hypersurface, all d restrictions should be equivalent. They are sometimes not equivalent because of the approximations which have been made.

Fig. 17 shows linear equations for six regions of a steady state manifold of the Gray-Scott network. They were obtained using the same procedures as those used in section 2.4.1. Letting $\log B = \log B$ for every pair of neighbouring regions yields analytical formulas of the three SN and one SN$^+$ stability boundaries listed in Table 1. These boundary equations are hyperplanes in a 5-dimensional log space. Their corresponding non-log forms are also given in the table.

Table 1. SN & SN$^+$ Stability Boundaries of the GS Network
(produced by the hyperplane approximation)

No.	Expressions
SN$_1$	$1.16 \log k_0 + \log B_0 + 1.26(\log A_0 + \log k_1) - 2.48 \log k_2 - 0.42 = 0$
	$k_0^{1.16} B_0 (A_0 k_1)^{1.26} k_2^{-2.48} = 2.6$
SN$^+$	$1.16 \log k_0 + 2.26 \log A_0 + 1.26 \log k_1 - 2.48 \log k_2 - 0.57 = 0$
	$k_0^{1.16} A_0^{2.26} k_1^{1.26} k_2^{-2.48} = 3.7$
SN$_2$	$1.19 \log k_0 - 2.26 \log A_0 - 1.26 \log k_1 + 0.27 = 0$
	$k_0^{1.19} A_0^{-2.26} k_1^{-1.26} = 0.53$
SN$_3$	$1.19 \log k_0 - \log B_0 - 1.26 \log A_0 - 1.26 \log k_1 + 0.13 = 0$
	$k_0^{1.19} B_0^{-1} (A_0 k_1)^{-1.26} = 0.75$

4.2 Analytical stability boundaries based on the DECA

The dominant extreme current approximation (DECA) presented in section 2.4.3 can also be used to derive analytical stability boundary equations. For a given ordering of the J parameters we can derive the steady state manifold equations using the DECA method. The intersection of two hyperplanes gives SN and SN$^+$ stability boundary equations as discussed in the previous section. The formulas are usually only valid in the region of the parameter space where the J parameters have the

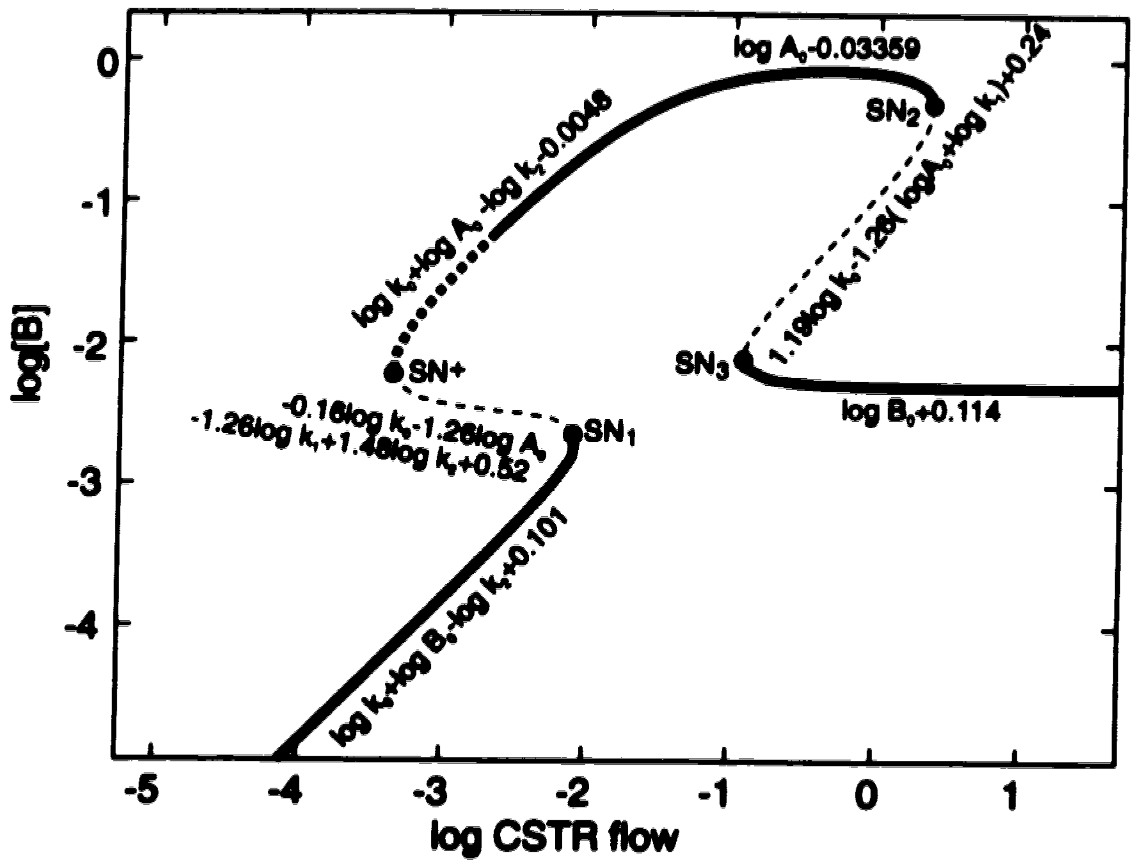

Fig. 17 Steady state manifold equations of the Gray-Scott network, produced by the hyperplane approximation. Parameters: $\log A_0 = -1.727 \times 10^{-2}; \log B_0 = -2.310; \log k_1 = 1.010; \log k_2 = -1.494$.. Left sides of the equations are all $\log B$, i.e.,

Region #1: $\log B = \log k_0 + \log B_0 - \log k_2 + 0.101$

Region #2: $\log B = -0.16 \log k_0 - 1.26(\log A_0 + \log k_1) + 1.48 \log k_2 + 0.52$

Region #3: $\log B = \log k_0 + \log A_0 - \log k_2 - 0.0048$

Region #4: $\log B = \log A_0 - 0.03359$

Region #5: $\log B = 1.19 \log k_0 - 1.26(\log A_0 + \log k_1) + 0.24$

Region #6: $\log B = \log B_0 + 0.114$

order used. However, the method can be generalized to cover all of the parameter space by dividing the current polytope into simplices with every possible ordering of the currents. Since $r - d$ currents are used, there are $(r - d)!$ orderings. For the Gray-Scott network, $r - d = 4$ and there are 24 orderings.

Equations in the $(\mathbf{h}, \mathbf{j})$ parameters for the SN, SN^+ and Hopf stability boundaries can be derived using the standard approach of SNA. They may be converted to the equations in experimental parameters using the dominant extreme current approximation. The complete method includes five steps, which will be illustrated using the Gray-Scott network again as an example.

Step 1. *Decomposing a current polytope into simplices*

Section 2.2 showed that the set of steady states of a reaction network constitutes a current polytope in which each point represents a single steady state. Fig. 18(a) is the current polytope of the Gray-Scott network. It is a square pyramid in a three-dimensional space. Its five vertices correspond to the five extreme currents of the network. We now want to decompose the current polytope into simplices.

In a three-dimensional parameter space, simplices are tetrahedrons with four vertices. There are two ways to decompose the current polytope of the Gray-Scott network into simplices. One is to decompose the polytope into tetrahedrons (1,2,3,4) and (2,3,4,5), where the numbers in the parentheses represent the vertices (Fig. 18(b)). The other way is to decompose the polytope into tetrahedrons (1,2,3,5) and (1,3,4,5) as shown in Fig. 18(c). Either decomposition can serve our needs. I will use the first decomposition and carry out stability analysis for the simplices (1,2,3,4) and (2,3,4,5) in the $(\mathbf{h}, \mathbf{j})$ space.

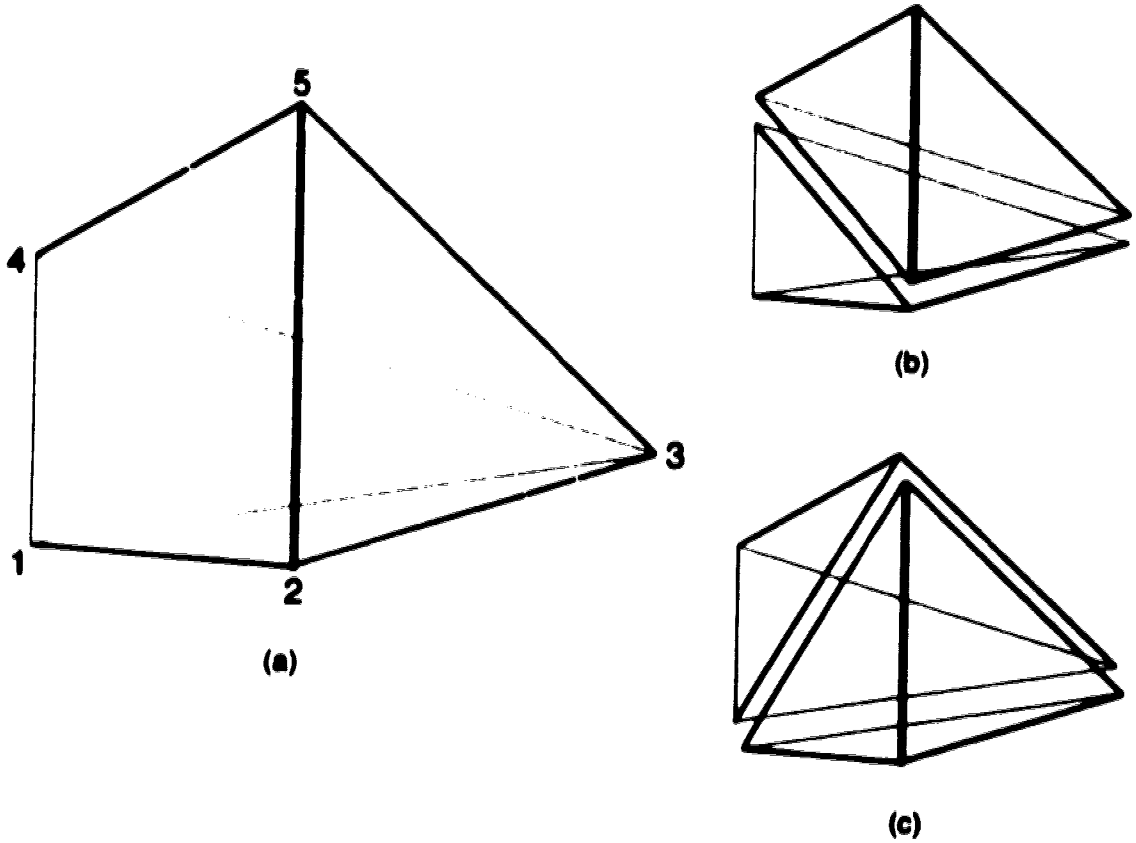

Fig. 18 The current polytope of the Gray-Scott network and two ways to divide it into simplices. (a) The current polytope of the Gray-Scott network, which is a three-dimensional square pyramid; (b) Decomposition of the current polytope into simplices (1,2,3,4) and (2,3,4,5); (c) Decomposition of the current polytope into simplices (1,2,3,4) and (2,3,4,5)

Step 2. *Calculating systems of inequalities for unstable regions in the* $(\mathbf{h},\mathbf{j})$ *parameter space*

The Jacobian matrix (equation (26)) in $(\mathbf{h},\mathbf{j})$ parameters has the form [28]

$$\mathbf{M} = \mathbf{N}\mathrm{diag}(\mathbf{E}\mathbf{j})\mathbf{K}^t\mathrm{diag}(\mathbf{h}). \tag{33}$$

The coefficients α_i of the corresponding characteristic equation (27) are polynomials in the $(\mathbf{h},\mathbf{j})$ parameters. The Hurwitz determinants built from the α_i are also polynomials in these parameters. Analyzing the polynomials using exponent polytopes[28] gives systems of inequalities for unstable regions in the $(\mathbf{h},\mathbf{j})$ parameter space. The results of a stability analysis for the Gray-Scott network using current polytope simplices (1,2,3,4) and (2,3,4,5) are given in Table 2.

Table 2. Unstable Regions of the Gray-Scott Network

Currents#	Oscillation Regions	Bistable Regions
1,2,3,4	$h_2 > h_1$ $j_1 > j_2$ $j_1 > j_4$ $j_1h_2 > j_3h_1$	$j_1 > j_2$ $j_3 > j_1$ $j_1 > j_4$
	$h_2 > h_1$ $j_4 > j_1$ $j_4 > j_2$ $j_4h_2 > j_3h_1$	$j_4 > j_1$ $j_4 > j_2$ $j_3 > j_4$
2,3,4,5	$h_2 > h_1$ $j_4 > j_2$ $j_4 > j_5$ $j_4h_2 > j_3h_1$	$j_4 > j_2$ $j_3 > j_4$ $j_4 > j_5$

Each system of inequalities in Table 2 is enclosed in a box. A system corresponds to an unstable region in the $(\mathbf{h},\mathbf{j})$ space. For the Gray-Scott network, there are three systems of inequalities for the oscillation regions and another three systems of inequalities for the bistable regions. In the next step, we will analyze these systems of inequalities and find the relative importance of the extreme currents for each system.

Step 3. *Finding all possible j-orderings consistent with a system of inequalities*

Most inequality systems contain inequalities involving the **j** parameters. They indicate the relative importance of certain extreme currents in the unstable region. Only certain orderings of the **j** parameters are consistent with these inequalities.

For example, the first system of inequalities for the oscillation region in Table 2 requires

$$j_1 > j_2, \qquad j_1 > j_4.$$

These two inequalities are consistent with only 8 of the 24 possible orderings of j_1, j_2, j_3, j_4. The acceptable orderings are:

$$j_1 > j_2 > j_3 > j_4, \qquad j_1 > j_2 > j_4 > j_3$$

$$j_1 > j_3 > j_2 > j_4, \qquad j_1 > j_3 > j_4 > j_2$$

$$j_1 > j_4 > j_2 > j_3, \qquad j_1 > j_4 > j_3 > j_2$$

$$j_3 > j_1 > j_2 > j_4, \qquad j_3 > j_1 > j_4 > j_2.$$

For the simplex (2,3,4,5), there are also 24 possible orderings of j_2, j_3, j_4, j_5. The unstable region inequalities in Table 2 must be evaluated in each of the 48 j-orderings for both simplices. Similarly, if we decompose the current polytope into the two simplices (1,2,3,5) and (1,3,4,5), we also get 48 different j-orderings. This means we can divide unstable regions into 48 small regions. In any small region the relative importance of the extreme currents has a specific order. The dominant extreme current approximation method discussed in section 2.4.3 will now be applied to each small region. This will give an analytical mapping between the (**h**, **j**) parameters and the (**k**, **C**) parameters, which can be used to convert the inequalities in Table 2 into inequalities in the (**k**, **C**) parameters.

Step 4. *Dominant extreme current approximation*

For the set of $(\mathbf{h},\mathbf{j})$ parameters using currents j_1, j_2, j_3, j_4, there are 24 orderings of the $\mathbf{j}$ parameters. The dominant extreme current approximation discussed in Sections 2.4.3 and 2.4.4 can be applied to each possible ordering. For example, the ordering $j_1 > j_2 > j_3 > j_4$ yields the simplified current matrix

$$\mathbf{E}_0 = \begin{pmatrix} 1 & 0 & 0 & 0 & 0 \\ 1 & 0 & 0 & 0 & 0 \\ 0 & 0 & 1 & 0 & 0 \\ 0 & 0 & 0 & 1 & 0 \\ 1 & 0 & 0 & 0 & 0 \\ 0 & 1 & 0 & 0 & 0 \end{pmatrix}$$

and the simplified steady state reaction rate vector

$$\mathbf{v}^0 = (j_1, j_1, j_3, j_4, j_1, j_2)^t.$$

Using this reaction rate vector as the left side of equation (23) gives

$$j_1 = k_1 A B^2$$

$$j_1 = k_2 B$$

$$j_3 = k_0 A$$

$$j_4 = k_0 B$$

$$j_1 = k_0 A_0$$

$$j_2 = k_0 B_0,$$

which produces the mapping

$$A = \frac{k_2^2}{k_0 k_1 A_0}$$

$$B = \frac{k_0 A_0}{k_2}$$

$$j_1 = k_0 A_0$$

$$j_2 = k_0 B_0$$

$$j_3 = \frac{k_2^2}{k_1 A_0}$$

$$j_4 = \frac{k_0^2 A_0}{k_2}.$$

The mapping is determined by the simplified steady state reaction rate vector $\mathbf{v}^0$. Several j-orderings could produce the same simplified steady state reaction rate vectors, and hence the same mapping. For the Gray-Scott network, I have found that the 24 orderings of j_1, j_2, j_3, j_4 and 24 orderings of j_2, j_3, j_4, j_5 produce 16 different simplified steady state reaction rate vectors $\mathbf{v}^0$. Therefore, there are 16 different mappings between the $(\mathbf{h}, \mathbf{j})$ and the $(\mathbf{k}, \mathbf{C})$ parameters. All steady state reaction rate vectors, their corresponding j-orderings, and the resulting mappings are given in Appendix 2.

Sometimes the system of six equations in the six $(\mathbf{h}, \mathbf{j})$ parameters $(A, B, j_1, j_2, j_3, j_4)$ is not solvable unless certain relationships among the $(\mathbf{k}, \mathbf{C})$ parameters hold. Examples appear in the tables of Appendix 2.

Step 5. *Substituting the mapping into the systems of inequalities*

When all mappings are substituted into each of the six systems of inequalities in Table 2, certain combinations have no solutions. The combinations with solutions yield two bistable regions and two oscillation regions in the $(\mathbf{k}, \mathbf{C})$ parameter space. The two bistable regions are

$$1. \quad \begin{cases} k_0 > k_2 \\ k_0 > k_1 A_0 B_0 \\ k_1 A_0^2 > k_0 \end{cases}$$

$$2. \quad \begin{cases} k_2^2 > k_0 k_1 A_0 B_0 \\ k_0 k_1 A_0^2 > k_2^2 \\ k_2 > k_0. \end{cases}$$

The two oscillation regions are

$$1. \quad \begin{cases} k_2^3 > k_0^2 k_1 A_0^2 \\ A_0 > B_0 \\ k_2 > k_0 \\ k_0 k_1 A_0^2 > k_2^2 \end{cases}$$

$$2. \quad \begin{cases} k_1 A_0^2 > k_2 \\ k_2^2 > k_0 k_1 A_0 B_0 \\ k_2 > k_0 \\ k_0 k_1 A_0^2 > k_2^2. \end{cases}$$

Fig.19 shows the accurate stability boundaries and the approximate stability boundaries. They are qualitatively very similar. Even though the analytical stability boundaries do not exactly match the accurate stability boundaries, the approach has some unique advantages. The accurate stability boundaries can only be calculated in a low dimensional subspace (usually two-dimensional), but the analytical formulas are valid in the full high dimensional parameter space. They can answer questions that cannot be answered by the numerical stability boundaries, such as how various two-dimensional stability boundaries are affected by all the other experimental parameters.

The analytical stability boundaries can reveal additional useful facts. For example, the first system of inequalities for the bistable regions in the (**k**, **C**) parameters tells us:

1. The range of k_0 covered by the first bistable region is determined by the parameters A_0, k_1, B_0;
2. When k_1, B_0 are fixed, increasing A_0 will move the bistable regions to a higher k_0 range;
3. When k_1, B_0 are fixed, increasing A_0 will widen the bistable range.

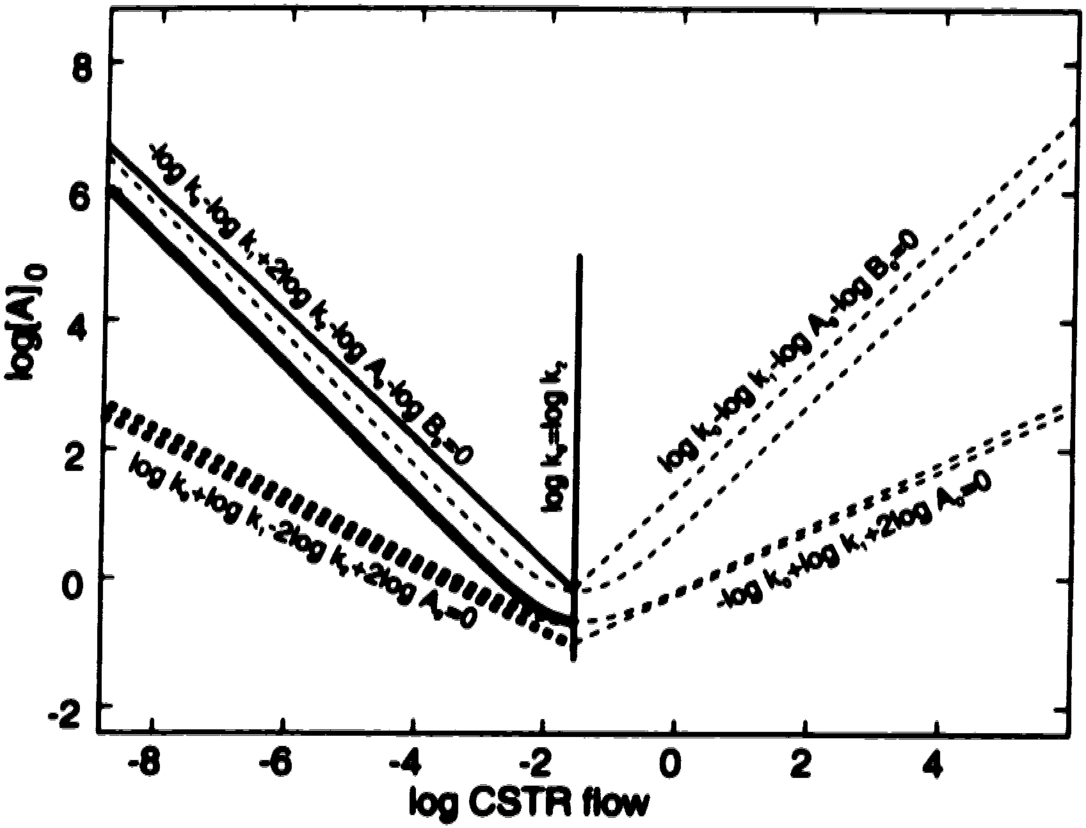

Fig. 19 Stability boundaries of the Gray-Scott network calculated by the numerical continuation (curves without equations) and by the approximated analytical formulas (curves with equations). Parameters: $\log B_0 = -2.310; \log k_1 = 1.010; \log k_2 = -1.494$.

I have examined the Gray-Scott network thoroughly and have confirmed these conclusions.

4.3 Directly derivable analytical stability boundaries

Analytical stability boundaries can sometimes be derived directly from equation (8)

$$\mathbf{Ej} = \mathrm{diag}(\mathbf{k})\mathbf{X}_0^{\mathbf{K}} = \mathrm{diag}(\mathbf{k})\mathbf{h}^{-\mathbf{K}}$$

in combination with a boundary equation in (**h**, **j**) parameters. The boundary equation in the (**h**, **j**) parameters can greatly simplify the process of solving equation (8), which may otherwise be unsolvable.

The Showalter-Noyes-Bar-Eli (SNB) network[38] is a typical network that contains directly derivable analytical stability boundaries. Fig. 20 is the network diagram of the SNB network. Fig. 21(a) is a cross-section of its steady state manifold and Fig. 21(b) is one of its two-dimensional phase diagrams. To explain the procedure for deriving analytical formulas, I will focus on obtaining the formula for the stability boundary near the point P in Fig. 21 (the low Hopf bifurcation surface).

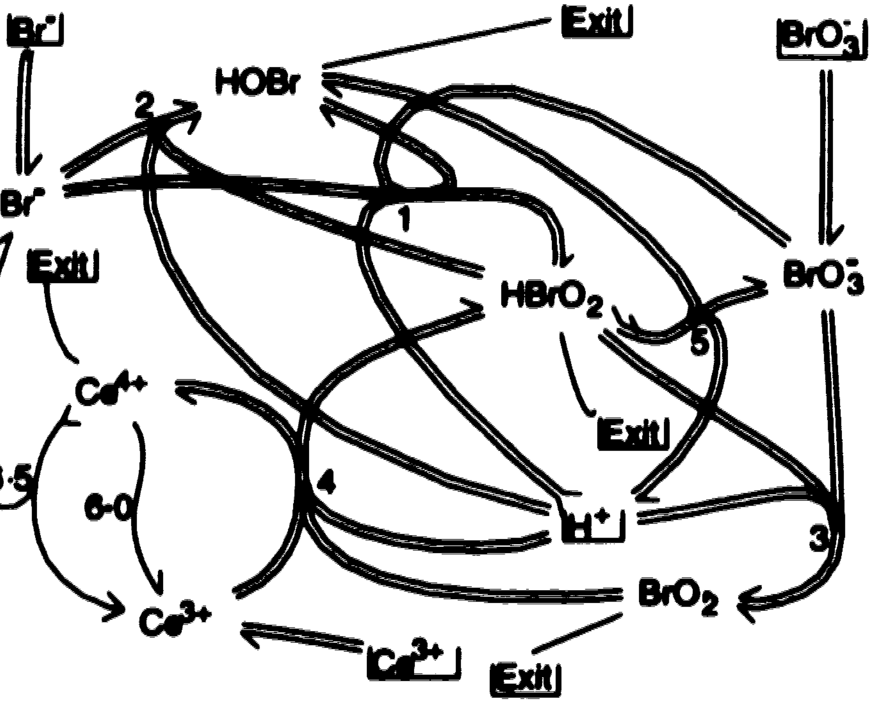

Fig. 20 Network diagram of the SNB reaction network.

Detailed studies[43] found that four of the network's 53 extreme currents, $(\mathbf{E}_1, \mathbf{E}_4, \mathbf{E}_7, \mathbf{E}_{12})$, are necessary for producing the stability boundary at P. The

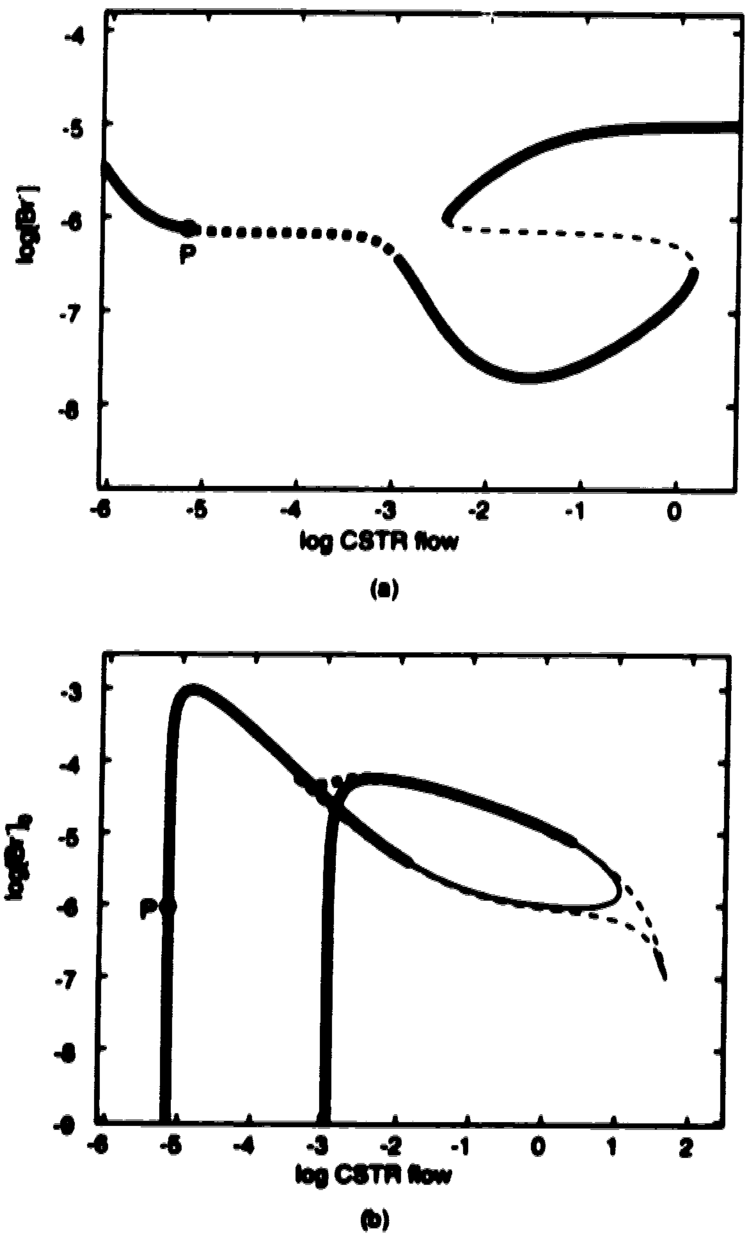

Fig. 21 (a) Steady state manifold of the SNB network on the ($\log[\mathrm{Br}^-]$, $\log k_0$) plane; (b) Stability boundaries of the SNB network on the ($\log[\mathrm{Br}^-]_0$, $\log k_0$) plane.

extreme current submatrix consisting of these four currents is

$$
\mathbf{E} = \begin{array}{c} \\ \mathrm{R}_1 \\ \mathrm{R}_2 \\ \mathrm{R}_3 \\ \mathrm{R}_4 \\ \mathrm{R}_{6.5} \\ \mathrm{I}_1 \\ \mathrm{O}_7 \\ \mathrm{O}_1 \\ \mathrm{R}_{-1} \\ \mathrm{R}_{-4} \end{array}
\begin{array}{c} \begin{array}{cccc} \mathbf{E}_1 & \mathbf{E}_4 & \mathbf{E}_7 & \mathbf{E}_{12} \end{array} \\
\left(\begin{array}{cccc}
1 & 0 & 0 & 0 \\
0 & 0 & 0 & 1 \\
0 & 0 & 0 & 1 \\
0 & 1 & 0 & 2 \\
0 & 0 & 0 & 1 \\
0 & 0 & 1 & 1 \\
0 & 0 & 0 & 2 \\
0 & 0 & 1 & 0 \\
1 & 0 & 0 & 0 \\
0 & 1 & 0 & 0
\end{array} \right) \end{array} .
$$

where reaction numbers $R_1, R_2, \ldots$ stand for reactions 1, 2, ... on the network diagram; I_1, O_1 are the CSTR input and output reactions for BrO_3^-; O_7 is the CSTR output reaction for HOBr. The rate laws for the reactions involved in the four currents are

$$v_1 = k_1[\mathrm{BrO_3^-}][\mathrm{Br^-}][\mathrm{H^+}]^2$$

$$v_2 = k_2[\mathrm{HBrO_2}][\mathrm{Br^-}][\mathrm{H^+}]$$

$$v_3 = k_3[\mathrm{BrO_3^-}][\mathrm{HBrO_2}][\mathrm{H^+}]$$

$$v_4 = k_4[\mathrm{Ce^{3+}}][\mathrm{BrO_2}][\mathrm{H^+}]$$

$$v_{6.5} = k_{6.5}[\mathrm{Ce^{4+}}]^2$$

$$v_{I_1} = k_0[\mathrm{BrO_3^-}]_0$$

$$v_{O_7} = k_0[\mathrm{HOBr}]$$

$$v_{O_1} = k_0[\mathrm{BrO_3^-}]$$

$$v_{-1} = k_{-1}[\mathrm{HBrO_2}][\mathrm{HOBr}]$$

$$v_{-4} = k_{-4}[\mathrm{HBrO_2}][\mathrm{Ce^{4+}}]$$

where the subscripts attached to v's are the reaction numbers. Note that H^+ is treated as a major species in the network, so its concentration is constant.

Substituting $\mathbf{v}^0 = \mathbf{E}\mathbf{j}$ in these rate expressions yields

$$k_1[BrO_3^-][Br^-][H^+]^2 = j_1 \tag{34.1}$$

$$k_2[HBrO_2][Br^-][H^+] = j_{12} \tag{34.2}$$

$$k_3[BrO_3^-][HBrO_2][H^+] = j_{12} \tag{34.3}$$

$$k_4[Ce^{3+}][BrO_2][H^+] = j_4 + 2j_{12} \tag{34.4}$$

$$k_{6.5}[Ce^{4+}]^2 = j_{12} \tag{34.5}$$

$$k_0[BrO_3^-]_0 = j_7 + j_{12} \tag{34.6}$$

$$k_0[HOBr] = 2j_{12} \tag{34.7}$$

$$k_0[BrO_3^-] = j_7 \tag{34.8}$$

$$k_{-1}[HBrO_2][HOBr] = j_1 \tag{34.9}$$

$$k_{-4}[HBrO_2][Ce^{4+}] = j_4. \tag{34.10}$$

The solution of this system of equations is the desired mapping between the $(\mathbf{h}, \mathbf{j})$ and the $(\mathbf{k}, \mathbf{C})$ parameters. Nonlinear systems such as these are typically tedious and often impossible to solve.

The stability boundary of the network is given by one more equation. A stability analysis in the $(\mathbf{h}, \mathbf{j})$ parameters shows that the low Hopf boundary at P in Fig. 21 is

$$j_{12} = 3j_1. \tag{34.11}$$

The introduction of this stability boundary equation greatly simplifies the calculation of the stability boundaries. Combining equations (34.7), (34.9) and (34.11) gives

$$k_0[\mathrm{HOBr}] = 6k_{-1}[\mathrm{HBrO_2}][\mathrm{HOBr}],$$

which can be solved to get

$$[\mathrm{HBrO_2}] = \frac{k_0}{6k_{-1}}. \tag{35}$$

Combining equations (34.1), (34.2) and (34.11) yields

$$3k_1[\mathrm{BrO_3^-}][\mathrm{H^+}] = k_2[\mathrm{HBrO_2}]. \tag{36}$$

Substituting (35) into (36) and rearranging the equation produce

$$[\mathrm{BrO_3^-}] = \frac{k_0 k_2}{18k_1 k_{-1}[\mathrm{H^+}]}. \tag{37}$$

According to equations (34.8) and (37),

$$j_7 = k_0[\mathrm{BrO_3^-}] = \frac{k_0^2 k_2}{18k_1 k_{-1}[\mathrm{H^-}]}.$$

According to equations (34.3), (37) and (35),

$$j_{12} = k_3[\mathrm{BrO_3^-}][\mathrm{HBrO_2}][\mathrm{H^+}] = \frac{k_0^2 k_2 k_3}{108k_1 k_{-1}^2}.$$

Since $k_0[\mathrm{BrO_3^-}]_0 = j_7 + j_{12}$, the low Hopf boundary equation is

$$k_0 = \frac{108k_1 k_{-1}^2[\mathrm{H^+}][\mathrm{BrO_3^-}]_0}{k_2(6k_{-1} + k_3[\mathrm{H^+}])}. \tag{38}$$

Here the j_7 and j_{12} expressions have been used.

Equation (38) represents the vertical line on the $(\log k_0, \log [\mathrm{Br}^-]_0)$ plane shown in Fig. 21. It is nonlinear in other dimensions. Similar procedures were used to derive equations for the other stability boundaries of the SNB network. See Ref. 43 for the detail.

4.4 Slope patterns and stability boundaries

I have discussed three methods for deriving analytical stability boundaries; however, there are still circumstances where analytical formulas cannot be obtained. The stability boundaries might be located in a highly nonlinear region so the hyperplane approximation cannot be used. The extreme currents might have comparable rates, so that approaches based on big differences in j values cannot be used.

Even under these situations, it is often possible to get information on how the experimental parameters affect the stability boundaries. I developed a method based on the slope differences on opposite sides of a bifurcation point. The sign pattern of the slope differences shows how to adjust each parameter in order to move the stability boundaries in any desired direction on the phase diagram.

We need the signs of the coefficients of a tangent hyperplane to the steady state manifold at two points, called #1 and #2. The tangent hyperplane is given by the same equation used for the hyperplane approximation,

$$\log X_i = \sum_{j=1}^{m} s_{ij} \log a_j + c_i .$$

The signs of the coefficients s^1_{ij} and s^2_{ij} at the two points can be obtained from plots of the steady state manifold produced by the SNA software.

The procedure starts with moving the cursor to point #1 on one side of a bifurcation point of interest. Steady state manifold cross-sections with respect to all other experimental parameters are calculated and approximate slopes s^1_{ij} at the cursor point are recorded. Then the cursor is moved to point #2 on the other side of the bifurcation point and the slopes s^2_{ij} are recorded again. It doesn't matter if we cannot measure slopes accurately as long as we can tell the relative magnitudes of the slopes at two sides of the bifurcation point. Put a "+","0" or "−" sign at the corresponding position in the sign pattern if $s^1_{ij} > s^2_{ij}$, $s^1_{ij} = s^2_{ij}$ or $s^1_{ij} < s^2_{ij}$. Only parameters with "+" or "−" signs affect the positions of stability boundaries.

As an example, consider the steady state manifold shown in Fig. 22 of the simplified BSF network[25] called the BSFSN network. (Details on the BSFSN network will be discussed in chapter XI). Two abscissa parameters will be used to illustrate the procedures.

Consider the lower left saddle-node bifurcation point in Fig. 22. Parts (a) and (c) show that the slope is greater than 0 at the point 1 and it is less than 0 at the point 2 when the log CSTR flow rate is used as the abscissa parameter. At the first position in the sign pattern, we write a "+" sign because the slope at the point 1 is greater than the slope at point 2. Similarly, Fig. 22(b) and Fig. 22(d) show that the slope is great than 0 at the point 1 and less than 0 at the point 2 when $\log [SO_3^{2-}]_0$ is used as the abscissa parameter. Then, we write another "+" sign at the second position in the sign pattern. Calculating the steady state manifold using all other abscissa parameters and using the fixed species $\log\ [H^+]$, we can determine all the signs in the sign pattern. The resulting sign pattern is

$$\mathrm{sign}(s^1_{ij} - s^2_{ij}) = \begin{array}{ccccccccc} k_0 & [SO_3^{2-}]_0 & [BrO_3^-]_0 & k_1 & k_2 & k_3 & k_5 & k_6 & k_7 \\ \multicolumn{9}{c}{\left(+, \quad +, \quad -, \quad -, \quad -, \quad 0, \quad +, \quad 0, \quad + \right)} \end{array}$$

2

PM-1 3½"x4" PHOTOGRAPHIC MICROCOPY TARGET
NBS 1010a ANSI/ISO #2 EQUIVALENT

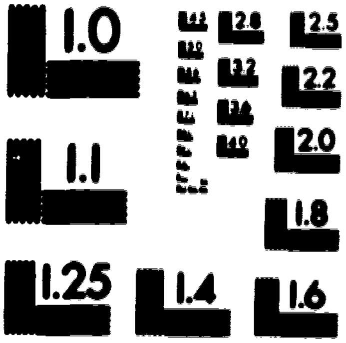

PRECISION℠ RESOLUTION TARGETS

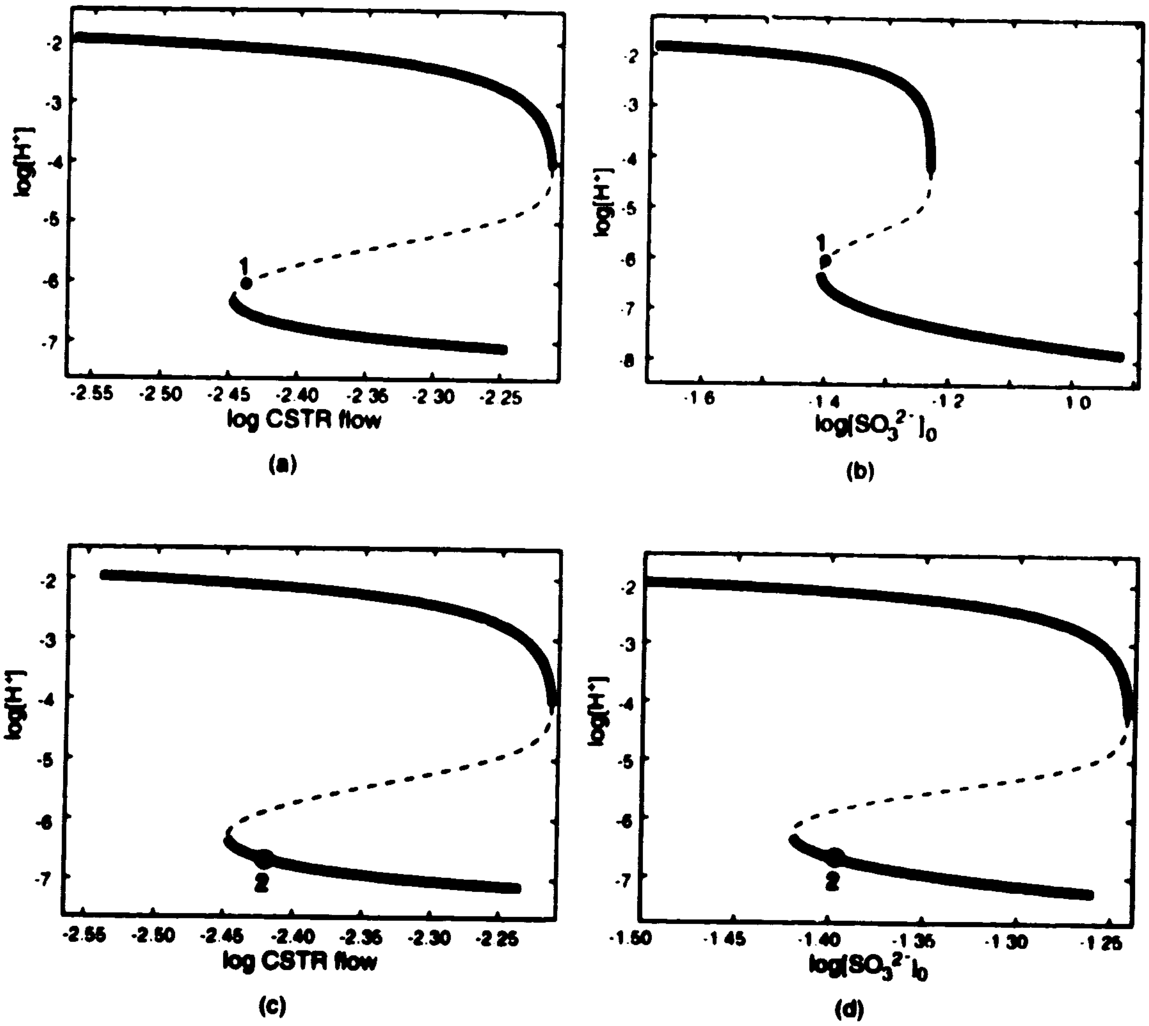

Fig. 22 Steady state manifolds of the BSFSN network. Two abscissa parameters are used here. Please note the slopes at: (a) point 1 with CSTR flow rate as the abscissa parameter; (b) point 1 with log $[SO_3^{2-}]_0$ as the abscissa parameter; (c) point 2 with CSTR flow rate as the abscissa parameter; (d) point 2 with log $[SO_3^{2-}]_0$ as the abscissa parameter. A pattern of slope differences is constructed for this network in order to determine the effects of experimental parameters on the stability boundaries of the network.

The mathematical justification for the method to be used is as follows. At a bifurcation point, we have

$$s_1^1 \log a_1 + s_2^1 \log a_2 + \cdots + s_m^1 \log a_m + c_1$$
$$= s_1^2 \log a_1 + s_2^2 \log a_2 + \cdots + s_m^2 \log a_m + c_2. \tag{39}$$

If we choose the first and the second abscissa parameters to be the independent and the dependent parameters respectively, then equation (39) can be written as

$$\log a_2 = -\frac{s_1^1 - s_1^2}{s_2^1 - s_2^2} \log a_1 - \sum_{i=3}^{m} \left(\frac{s_i^1 - s_i^2}{s_2^1 - s_2^2} \right) \log a_i + C. \tag{40}$$

where C is a constant.

In equation (40), the terms within the summation on the right-hand side determine the intercept of the two-dimensional stability boundary. For the i-th term in the summation, if $\frac{s_i^1 - s_i^2}{s_2^1 - s_2^2} > 0$, then increasing a_i will decrease the $\log a_2$ intercept because of the negative sign ahead of it.

Based on equation (40), we now give a method for constructing a new sign pattern such that a "+" or "-" indicates whether increasing $\log a_i$ increases or decreases the intercept. First we decide which variables will be plotted on the vertical axis (a_2=dependent variable) and the horizontal axis (a_1=independent variable) of the two-dimensional phase diagram. If the sign corresponding to the dependent variable a_2 is "+", reverse all signs in the sign pattern. Otherwise, keep all the signs unchanged. The resulting sign pattern gives the sign of the coefficient of $\log a_i$ in equation (40). Since the dependent variable a_2 does not appear on the right of equation (40), put a blank in the new sign pattern for a_2.

Now let's use these ideas to adjust parameters so the stability boundary in Fig. 22 increases its intercept. If we choose $[SO_3^{2-}]_0$ and k_0 as the dependent and the independent variables for the BSFSN network, the new sign pattern is

$$\begin{array}{ccccccccc} k_0 & [SO_3^{2-}]_0 & [BrO_3^-]_0 & k_1 & k_2 & k_3 & k_5 & k_6 & k_7 \\ \left(-, \right. & , & +, & +, & +, & 0, & -, & 0, & \left. \right) \end{array}.$$

A "+" sign in the new sign pattern indicates that increasing the corresponding variable will increase the intercept of the two-dimensional stability boundary. A "−" sign indicates the opposite.

We can also read from the new sign pattern how to shift the boundary to the left or right. If the sign corresponding to the independent variable a_1 is "+", increasing the intercept means moving the stability boundary to the left. Otherwise, it means moving the stability boundary to the right.

For the BSFSN network, since the sign corresponding to the independent variable k_0 is −, we need to decrease any of the variables whose signs are +, or increase any of the variables whose signs are −, in order to move the two-dimensional stability boundary to the left. That is to say, we need to decrease any of the $[BrO_3^-]_0, k_1, k_2$ or increase any of the k_5, k_7 to move the stability boundary to the left.

This method will be used in section 6.5 to adjust parameter values in order to fit experimental stability boundaries of the BSF network.

4.5 *Adjusting experimental parameters to fit experimental results*

The task of adjusting parameters to fit experimental results is an important task. It may be accomplished using the methods discussed in the previous sections and other features of the new SNA program package. The methods available for parameter adjustment are:

1. If we can derive analytical stability boundary equations using one of the three methods discussed in sections 4.1 to 4.3, we know which experimental variables affect stability boundaries and how to adjust them to move the boundaries in order to fit experiments;

2. If we cannot derive stability boundary equations explicitly, the sign pattern method in section 4.4 can be used to make paramcter adjustments;

3. Another method uses the SNA program package interactively. On the steady state manifold screen, the cursor is put on a bifurcation point. The following procedure moves the stability boundary so that the cursor is in the interior of the unstable region. First have the program calculate another cross-section of the steady state manifold using a different abscissa parameter. On the new cross-section, the cursor is on the same bifurcation point observed in the previous cross-section. Move the cursor into the interior of the unstable region. Recalculate the steady state manifold using the first abscissa parameter. The position of the bifurcation point will have moved so that the cursor in now in the interior of the unstable region.

   The reverse of this procedure will move the boundary in the opposite direction. This procedure has been used for the oxalate-peroxide-sulfite network analysis[37].

V. Stability boundaries of the Gray-Scott network

The Gray-Scott network is a simple, but dynamically rich network. It contains almost all experimentally observed nonlinear features such as oscillations and bistability, except chaos. It is a promising prototype network for modelling nonlinear dynamics of chemical reaction networks.

In their papers, Gray and Scott[15-20] used a set of dimensionless parameters to treat the network analytically. In this chapter, I will do a systematic investigation in the conventional experimental parameter space. I will explain the emergence of various nonlinear dynamical features, the structure of stability boundaries, the phase diagrams and the equations of stability boundaries in terms of chemically familiar concentrations and rate constants. We will see how the important chemical pathways (dominant extreme currents) contribute to various steady states. The new method I will be using can also be applied to large networks, such as the BSF network which I will discuss in the next chapter.

5.1 The Gray-Scott network

The Gray-Scott network includes two chemical species and six reactions. Both species are intermediates and they are dynamical variables. Among the six reactions, only two are real chemical reactions. Two are CSTR inflow reactions that supply the two intermediates from reservoirs. Another two are CSTR outflow reactions that wash the two intermediates out of the system.

Scheme III and Fig. 23 are duplicates of Scheme II and Fig. 4 discussed in chapter II. The real reaction 1 is an auto-catalytic reaction in which B is both a product and a catalyst. It is an essential reaction to bring about instabilities. The real reaction 2 is a reaction that consumes B.

Scheme III:

$R_1=1$	$A+2B\xrightarrow{k_1}3B$	$v_1 = k_1AB^2$
$R_2=2$	$B\xrightarrow{k_2}$	$v_2 = k_2B$
R_3=A exit	$A\xrightarrow{k_0}$	$v_3 = k_0A$
R_4=B exit	$B\xrightarrow{k_0}$	$v_4 = k_0B$
R_5=A inflow	$\xrightarrow{k_0A_0} A$	$v_5 = k_0A_0$
R_6=B inflow	$\xrightarrow{k_0B_0} B$	$v_6 = k_0B_0.$

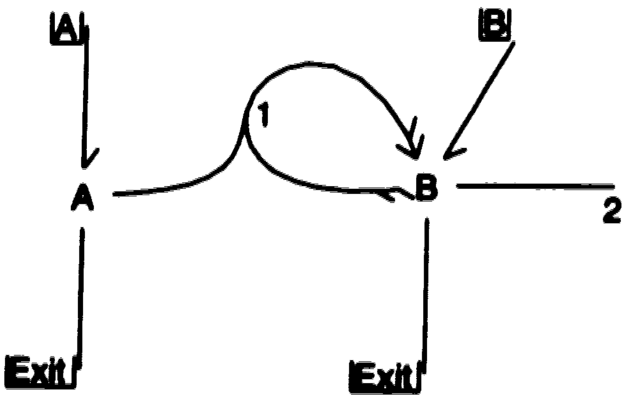

Fig. 23 The Gray-Scott reaction network.

Steady states of the intermediate A are determined by three reactions. The CSTR inflow reaction labeled by an A reservoir symbol provides A, while the real chemical reaction 1 and the CSTR outflow reaction consume A. When the rate of production of A equals the rate of consumption of A, A is at a steady state.

Four reactions affect the steady states of B. The CSTR inflow reaction labeled by a B reservoir symbol produces B. Real reaction 1 not only consumes but also produces B. Since the reaction 1 consumes only two B molecules in the reaction and produces three B molecules at the [illegible] effect of the reaction 1 is to produce B. The other two reaction [illegible] STR outflow reaction and the real reaction 2, consume B. B is at a [illegible] rate of production equals its rate of consumption. When both [illegible] steady state, the network is at a steady state.

The Gray-Scott network has [illegible] currents, i.e., there are five basic chemical pathways for the network [illegible] steady states. Fig. 24 shows the five extreme currents as thick lines. Currents $\mathbf{E}_1$, $\mathbf{E}_2$ and $\mathbf{E}_4$ involve real chemical reactions while currents $\mathbf{E}_3$ and $\mathbf{E}_5$ are simply *CSTR flow-through currents* with no real chemical reactions involved. The set of these five extreme currents constitutes the extreme current matrix $\mathbf{E}$

$$\mathbf{E} = \begin{pmatrix} 1 & 0 & 0 & 1 & 0 \\ 1 & 1 & 0 & 0 & 0 \\ 0 & 0 & 1 & 0 & 0 \\ 0 & 0 & 0 & 1 & 1 \\ 1 & 0 & 1 & 1 & 0 \\ 0 & 1 & 0 & 0 & 1 \end{pmatrix}.$$

Each column of the $\mathbf{E}$ matrix represents an extreme current and each row corresponds to a reaction in the sequence listed in Scheme III.

The five extreme currents are the five vertexes of the current polytope (see Fig. 18). They are five special steady states of the network. Any linear combinations of the five extreme currents with nonnegative coefficients (j values) are also steady states, and the whole set of steady states constitutes the steady state manifold. We know that some steady states are stable while some are unstable. We want to find the boundaries between the stable and unstable regions and to understand the structures of the stability boundaries.

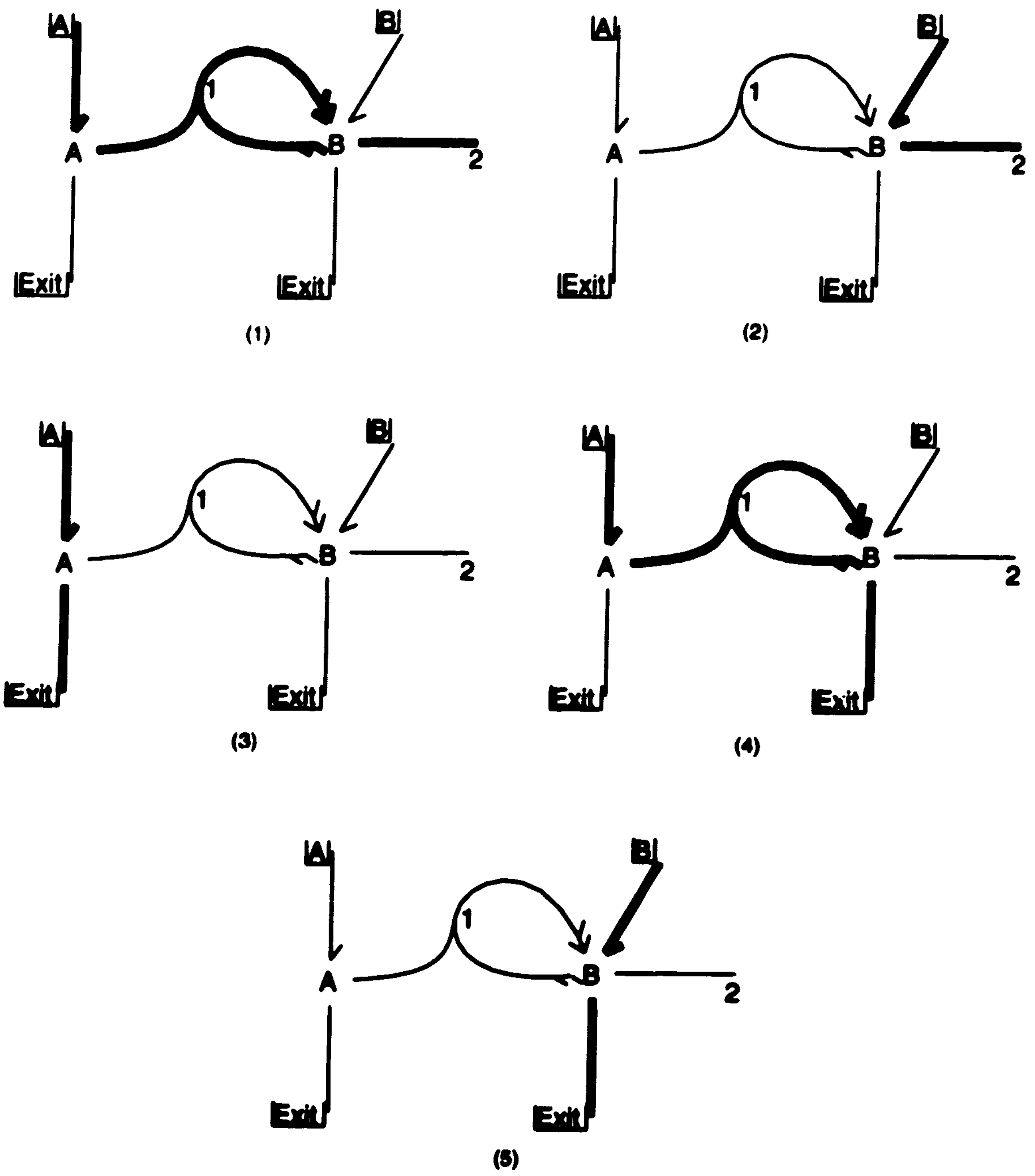

Fig. 24 Five extreme currents of the Gray-Scott reaction network.

5.2 *A complete stability analysis in the* (h,j) *parameter space*

Because of the simplicity of the Gray-Scott network, it is not difficult to do a complete stability analysis in the (h,j) parameter space. A *complete stability* *analysis* means that we do the stability analysis using all combinations of extreme currents. It provides us with complete information on the stability regions of the whole parameter space.

Table 3 summarizes the results of the complete stability analysis. In the table, j_i is the rate of the i-th extreme current. h_1 and h_2 are the reciprocal steady state concentrations of the intermediates A and B. The "conditions for $\Delta_1 < 0$" gives the regions bounded by Hopf bifurcation hypersurfaces. They are usually oscillation regions. The "conditions for $\alpha_2 < 0$" gives the regions surrounded by the SN or the SN^+ bifurcation hypersurfaces. Steady states in these regions are on middle branches of the folds. These regions are usually bistable. A "Yes" in the column "$\alpha_1 \equiv 0$" or "$\alpha_2 \equiv 0$" indicates that the corresponding α_i is identically zero for the combination of extreme currents. A "Yes" in the column "$\alpha_1 > 0$" or "$\alpha_2 > 0$" tells that the corresponding α_i is always positive for any chosen parameters.

Table 3. Stability Analysis of the GS Network in (h, j) Space

Currents#	conditions for $\Delta_1 < 0$	$\alpha_1 \equiv 0$	$\alpha_1 > 0$	conditions for $\alpha_2 < 0$	$\alpha_2 \equiv 0$	$\alpha_2 > 0$
1	$h_2 > h_1$					Yes
2			Yes		Yes	
3			Yes		Yes	
4	$h_2 > h_1$					Yes
5			Yes		Yes	
1,2	$h_2 > h_1$ $j_1 > j_2$					Yes
1,3	$h_2 > h_1$ $j_1 h_2 > j_3 h_1$			$j_3 > j_1$		
1,4	$h_2 > h_1$					Yes
1,5	$h_2 > h_1$ $j_1 > j_5$					Yes
2,3			Yes			Yes
2,4	$h_2 > h_1$ $j_4 > j_2$					Yes
2,5			Yes			Yes
3,4	$h_2 > h_1$ $j_4 h_2 > j_3 h_1$			$j_3 > j_4$		
3,5			Yes			Yes
4,5	$h_2 > h_1$ $j_4 > j_5$					Yes
1,2,3	$h_2 > h_1$ $j_1 > j_2$ $j_1 h_2 > j_3 h_1$			$j_1 > j_2$ $j_3 > j_1$		

* to be continued ...

Table 3. Stability Analysis of the GS Network in $(\mathbf{h},\mathbf{j})$ Space (continued)

Currents#	conditions for $\Delta_1 < 0$	$\alpha_1 \equiv 0$	$\alpha_1 > 0$	conditions for $\alpha_2 < 0$	$\alpha_2 \equiv 0$	$\alpha_2 > 0$
1,2,4	$h_2 > h_1$ $j_4 > j_1$ $j_4 > j_2$					Yes
	$h_2 > h_1$ $j_1 > j_2$ $j_1 > j_4$					
1,2,5	$h_2 > h_1$ $j_1 > j_5$ $j_1 > j_2$					Yes
1,3,4	$h_2 > h_1$ $j_4 > j_1$ $j_4h_2 > j_3h_1$			$j_4 > j_1$ $j_3 > j_4$		
	$h_2 > h_1$ $j_1 > j_4$ $j_1h_2 > j_3h_1$			$j_1 > j_4$ $j_3 > j_1$		
1,3,5	$h_2 > h_1$ $j_1 > j_5$ $j_1h_2 > j_3h_1$			$j_3 > j_1$ $j_1 > j_5$		
1,4,5	$h_2 > h_1$ $j_4 > j_1$ $j_4 > j_5$					Yes
	$h_2 > h_1$ $j_1 > j_4$ $j_1 > j_5$					
2,3,4	$h_2 > h_1$ $j_4 > j_2$ $j_4h_2 > j_3h_1$			$j_4 > j_2$ $j_3 > j_4$		
2,3,5			Yes			Yes

* to be continued ...

Table 3. Stability Analysis of the GS Network in $(\mathbf{h},\mathbf{j})$ Space (continued)

Currents#	conditions for $\Delta_1 < 0$	$\alpha_1 \equiv 0$	$\alpha_1 > 0$	conditions for $\alpha_2 < 0$	$\alpha_2 \equiv 0$	$\alpha_2 > 0$
2,4,5	$h_2 > h_1$ $j_4 > j_2$ $j_4 > j_5$					Yes
3,4,5	$h_2 > h_1$ $j_4 > j_5$ $j_4h_2 > j_3h_1$			$j_3 > j_4$ $j_4 > j_5$		
1,2,3,4	$h_2 > h_1$ $j_4 > j_1$ $j_4 > j_2$ $j_4h_2 > j_3h_1$			$j_4 > j_1$ $j_4 > j_2$ $j_3 > j_4$		
	$h_2 > h_1$ $j_1 > j_2$ $j_1 > j_4$ $j_1h_2 > j_3h_1$			$j_1 > j_2$ $j_3 > j_1$ $j_1 > j_4$		
1,2,3,5	$h_2 > h_1$ $j_1 > j_2$ $j_1 > j_5$ $j_1h_2 > j_3h_1$			$j_1 > j_2$ $j_3 > j_1$ $j_1 > j_5$		
1,2,4,5	$h_2 > h_1$ $j_4 > j_1$ $j_4 > j_2$ $j_4 > j_5$					Yes
	$h_2 > h_1$ $j_1 > j_2$ $j_1 > j_4$ $j_1 > j_5$					

* to be continued ...

Table 3. Stability Analysis of the GS Network in $(\mathbf{h}, \mathbf{j})$ Space (continued)

Currents#	conditions for $\Delta_1 < 0$	$\alpha_1 \equiv 0$	$\alpha_1 > 0$	conditions for $\alpha_2 < 0$	$\alpha_2 \equiv 0$	$\alpha_2 > 0$
1,3,4,5	$h_2 > h_1$ $j_1 > j_4$ $j_1 > j_5$ $j_1 h_2 > j_3 h_1$			$j_3 > j_1$ $j_1 > j_4$ $j_1 > j_5$		
	$h_2 > h_1$ $j_4 > j_1$ $j_4 > j_5$ $j_4 h_2 > j_3 h_1$			$j_4 > j_1$ $j_3 > j_4$ $j_4 > j_5$		
2,3,4,5	$h_2 > h_1$ $j_4 > j_2$ $j_4 > j_5$ $j_4 h_2 > j_3 h_1$			$j_4 > j_2$ $j_3 > j_4$ $j_4 > j_5$		
1,2,3,4,5	$h_2 > h_1$ $j_1 > j_2$ $j_1 > j_4$ $j_1 > j_5$ $j_1 h_2 > j_3 h_1$			$j_1 > j_2$ $j_3 > j_1$ $j_1 > j_4$ $j_1 > j_5$		
	$h_2 > h_1$ $j_4 > j_1$ $j_4 > j_2$ $j_4 > j_5$ $j_4 h_2 > j_3 h_1$			$j_4 > j_1$ $j_4 > j_2$ $j_3 > j_4$ $j_4 > j_5$		

According to table 3, current $\mathbf{E}_2$ and the two CSTR flow-through currents $\mathbf{E}_3$, $\mathbf{E}_5$ are stable currents. All combinations of these currents are also stable. Currents $\mathbf{E}_1$ and $\mathbf{E}_4$ include the auto-catalytic reaction 1. They are unstable currents. All combinations of currents containing either one or both of them are unstable.

Unstable currents $\mathbf{E}_1$ or $\mathbf{E}_4$ can cause oscillations by themselves because the condition $\Delta_1 < 0$ occurs. α_2 is always positive under these circumstances. A combination of the two unstable currents also possesses oscillatory features but cannot be bistable. Bistable regions exist if and only if one or both unstable currents combine with stable current $\mathbf{E}_3$, which is the CSTR flow-through current for the species A. All combinations of currents that contain bistability exhibit oscillatory dynamics. Current combinations that are oscillatory do not necessarily have bistability.

There is one common inequality for all unstable combinations of currents. It is $h_2 > h_1$. In other word, [B] < [A]. A steady state can only be unstable if the steady state concentration of B is lower than A. This is a universal conclusion for the whole network.

For the Gray-Scott network, α_1 is never identically zero. But there are three 1-current cases for $\mathbf{E}_2$, $\mathbf{E}_3$ and $\mathbf{E}_5$ where α_2 are identically zero. In each case, one of the species A or B is isolated. In $\mathbf{E}_2$ or $\mathbf{E}_5$, A is isolated. Hence [A] is constant. In $\mathbf{E}_3$, B is isolated. Hence [B] is constant. Therefore, in these cases $d = 1$ and $\alpha_2 \equiv 0$. In $\mathbf{E}_2$ or $\mathbf{E}_5$, we cannot have $k_0 = 0$ because B enters. So, we must have $[A]_0 = 0$. In $\mathbf{E}_3$, A enters so $[B]_0 = 0$.

5.3 Extreme currents and mushroom-shaped steady state manifold

Now let's examine some relationships between the extreme currents of the

Gray-Scott network and its steady state manifold in the experimental parameter space.

Fig. 25 is a steady state manifold of the Gray-Scott network. The curve's line patterns indicate the stability of the steady states. Solid lines and dashed lines represent stable and unstable steady states respectively. Among the unstable steady states, thin dashed lines stand for middle unstable branches of the folds. There is only one positive eigenvalue for each steady state on this branch. Thick dashed lines correspond to Hopf regions, where there exist two eigenvalues with positive real parts for each steady state.

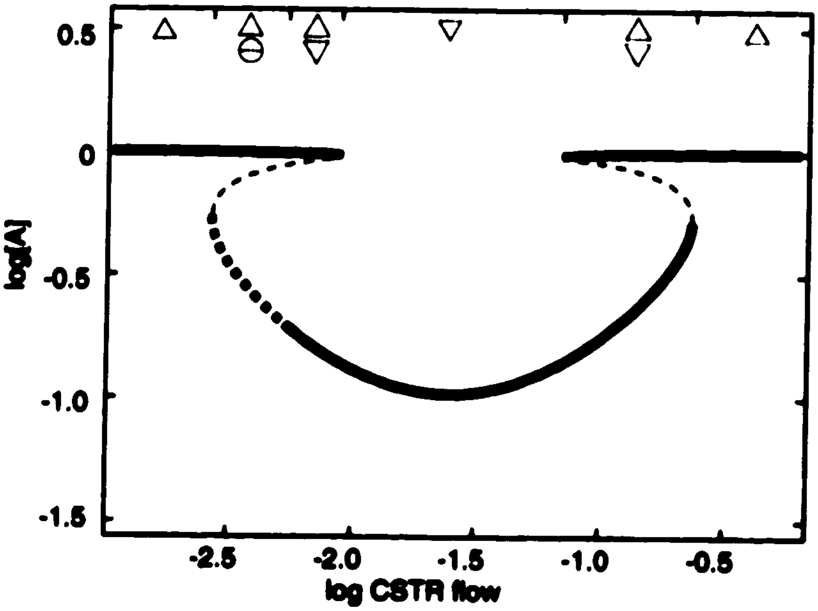

Fig. 25 Stabilities of steady states for the Gray-Scott network. All steady states on the dashed lines are unstable. All steady states on the solid lines are stable.

The curve in Fig. 25 looks like an inverted mushroom. Therefore it is sometimes called a *mushroom curve*. The mushroom curve can be divided into six regions according to the ordering of extreme current dominance. Fig. 26 shows graphical representations of the dominant currents in the six regions. It shows the underlying reasons for the curve shape and the stability of the different steady states.

In region 1, the high concentration of intermediate A makes the CSTR flow-through current of A (current $\mathbf{E}_3$) very important. The steady state concentration of A is totally determined by this current. The steady state concentration of B is determined by current $\mathbf{E}_2$ independently. Since currents $\mathbf{E}_3$ and $\mathbf{E}_2$ are both stable, the steady states in region 1 are stable.

In region 2, the lower steady state concentration [A] makes the CSTR flow through current $\mathbf{E}_3$ less important. It boosts up the relative importance of another current $\mathbf{E}_1$. The introduction of unstable current $\mathbf{E}_1$ causes the instability. The coexistence of current $\mathbf{E}_3$ and current $\mathbf{E}_1$ produces a fold and a bistability region in the parameter space. As a result, region 2 emerges as the middle branch of the fold and the region is unstable.

In region 3, the even lower concentration of A eliminates the importance of current $\mathbf{E}_3$. The most important current now is current $\mathbf{E}_1$ involving both the auto-catalytic reaction 1 and the B decomposition reaction 2. The steady states in this region are totally chemistry-controlled. Although the concentration [A] is low in this region, from Fig. 27 we can see that it is still higher than the concentration of species B. According to table 3, steady states in the region must be unstable and oscillatory dynamics exists in the region.

Region 4 appears symmetrical to region 3 on the log A *vs.* log k_0 mushroom-shaped curve. But they are apparently different on the log [B] *vs.* log k_0 curve shown in Fig. 27(b). The difference is caused by the fact that the higher flow rate in region

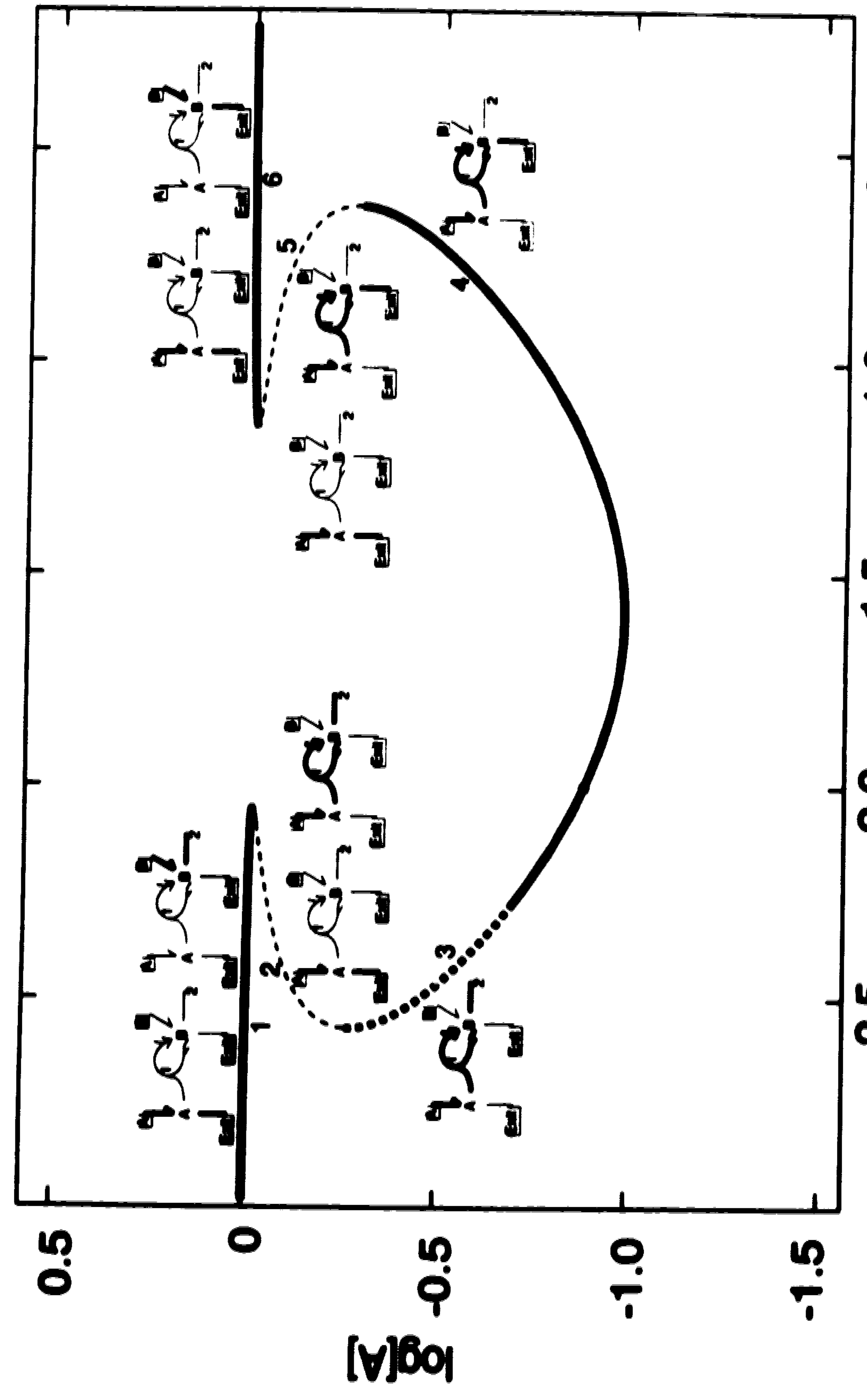

Fig. 26 Important extreme currents in various regions of the Gray-Scott network.

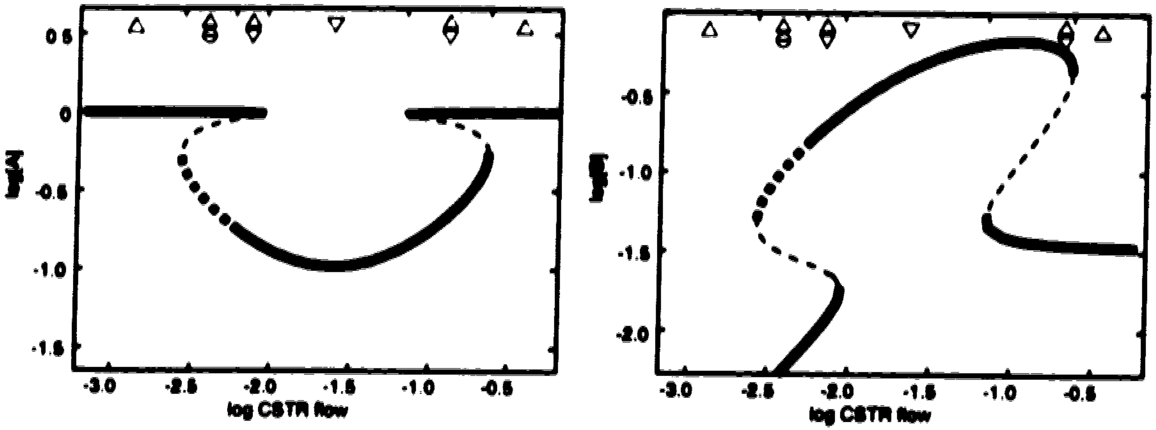

(a) (b)

Fig. 27 Comparison of two mushroom-shaped curves of the Gray-Scott network. (a) log A vs. log k_0; (b) log B vs. log k_0.

4 makes the CSTR outflow reaction of B more important than the B decomposition reaction in consuming B. Therefore, the most important current in region 4 is current $\mathbf{E}_4$ instead of current $\mathbf{E}_1$. Current $\mathbf{E}_4$ is also an unstable current and the region where current $\mathbf{E}_4$ dominates could be unstable. But since the concentration [B] is higher than [A] ($h_2 < h_1$), no system of inequalities for instability listed in table 3 is satisfied. So region 4 is a stable region.

Moving into region 5 from region 4, concentration [A] increases while concentration [B] decreases. Higher [A] raises the importance of the CSTR flow-through current of A again. Now the important currents are currents $\mathbf{E}_3$ and current $\mathbf{E}_4$. The combination of these two currents and the fact that they satisfy systems of inequalities for $\alpha_2 < 0$ cause region 5 to be the middle branch of the fold. Region 5 is unstable.

The even higher concentration of A in region 6 puts current $\mathbf{E}_3$ to an even more dominant position. In the region, concentration [A] is totally determined by the CSTR flow-through current of A. Concentration of B has to rely on another current $\mathbf{E}_5$. Comparing with region 1, the other important current is the CSTR flow-through current of B in region 6 while it is current $\mathbf{E}_2$ in region 1. The contributing factor to this difference is the flow rate value, which is higher in region 6 and is lower in region 1. Since steady state concentrations [A] and [B] are determined by the two CSTR flow-through currents respectively, they are all constant in region 6 and their values are determined by their concentrations in the CSTR reservoir. The steady states in region 6 are all stable.

I have explained the relationships among the important extreme currents, the steady state manifold, and the stability properties of the steady states for the Gray-Scott network. Understanding steady state manifolds and stability properties in terms of the controlling chemical processes or pathways can help explain experimental observations and help model real-world chemical processes.

5.4 *Structural elements and bifurcation structures of stability boundaries*

Even through the Gray-Scott network is a simple model network, it has all the six types of structural elements and bifurcation structures discussed in chapter III. The network possesses rich nonlinear dynamics.

Fig. 28 shows three two-dimensional phase diagrams of the Gray-Scott network, which are plotted in the two-dimensional ($\log [\mathrm{A}]_0, \log k_0$), ($\log [\mathrm{B}]_0, \log k_0$), ($\log k_1, \log k_0$) subspaces respectively. Unless otherwise specified, the parameters used for the calculations are

	k_0	A_0	B_0	k_1	k_2
	--	--	--	--	--
k :	0.01	1	0.03333	1	0.025
log **k** :	−2	0	−1.477	0	−1.60206

Except for parameters explicitly shown on the diagram, all other parameters are constant during the numerical continuation calculations.

Each phase diagram in Fig. 28 contains at least five different structural elements. They include the stability boundary pieces composed of the thin dashed SN curves, the thick dashed SN$^+$ curves, the thick solid Hopf curves, and the thin solid SE curves. They also contain DZ points. Fig. 28(b) has two cusp points.

There is one DZ point in Fig. 28(a), which is the centre of the general structure discussed in section 3.3. We can quickly identify a Y-shaped structure formed by a Hopf, a SN$^+$ and a SN curve. On the left half of the diagram, when the log [A]$_0$ value is decreased, the Hopf curve and the SN$^+$ curve get closer and closer to each other. They eventually join at the DZ point, and merge to produce a new SN curve. This is a type I Y-structure. When the SE curve is also considered in the DZ-centred structure, a more general structure where the DZ is the crossing point of the (SN,SN$^+$) and the (Hopf,SE) curves is recognized. After passing through the DZ point, the SE curve quickly turns back to the higher [A]$_0$ but lower k_0 region and appears to merge with another SN curve. A careful examination shows the SE and the SN curves never touch each other in the parameter range investigated. The SE curve stays on the left side of the SN curve as far as numerical integrations were carried out (SE points are always located on the middle branch of a fold on a steady state manifold). If the SE could touch the SN curve, it would cause a new DZ point and a new Hopf curve. It would guide us into a new possible oscillation region. Such is not the case.

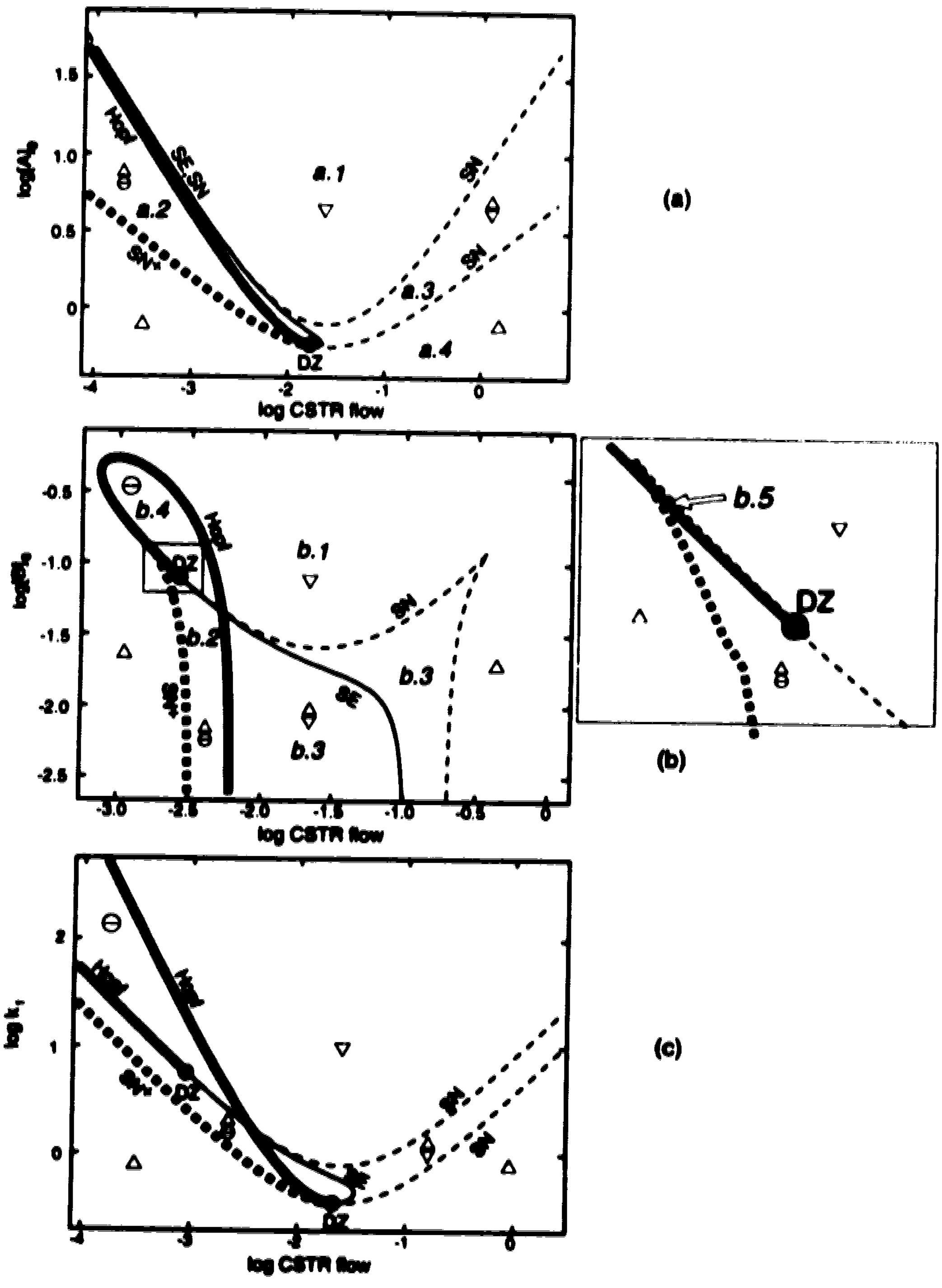

Fig. 28 Three two-dimensional phase diagrams of the Gray-Scott reaction network. (a)log $[A]_0$ *vs.* log k_0; (b)log $[B]_0$ *vs.* log k_0; (c)log k_1 *vs.* log k_0.

The stability boundaries shown in Fig. 28(b) are dynamically rich in the sense that they contain two cusp points and a crossing of a Hopf curve and a SN curve. The net effects of these structures are three different oscillation regions as well as the collapsing of bistable regions. I leave these interesting dynamic features to the next section and focus here on the bifurcation structure.

As for Fig. 28(a), we can quickly locate a Y-shaped structure and a crossing structure centred at the DZ point in Fig. 28(b). Note that the DZ point here does not belong to the same DZ hyperplane as the DZ point in Fig. 28(a). This DZ point is located on the upper branch of the fold on the steady state manifold while the DZ point in Fig. 28(a) is on the lower branch. Later we will see that the two DZ hyperplanes are connected by the SE curve in Fig. 28(c).

There are two cusp points in Fig. 28(b). Two folds on the mushroom-shaped steady state manifold disappear at the two cusp points respectively, and two SN (SN^+) hyperplanes join at the cusp points. So, we have two separate SN (SN^+) curves in Fig. 28(a), but we have only one unique SN (SN^+) curve in Fig. 28(b).

In Fig. 28(b), there is a crossing of the lower branch Hopf and the upper branch SN curves in the parameter space. This crossing is similar to the crossing discussed by Ringland[27] because both crossings are the crossing of a Hopf curve over a SN curve. But in Ringland's paper, the unstable region that started at the Hopf ends at another Hopf, while here the unstable region that started at the Hopf ends at a SN^+. This structural difference causes different stability regions in the parameter space. Therefore, the crossing appeared in the Gray-Scott network is a different type of crossing from that discovered by Ringland in the SNB network.

Fig. 28(c) reveals more aspects of the stability boundary structures of the

Gray-Scott network. It contains two DZ points and two Hopf bifurcation curves. They are located respectively on the upper branch and the lower branch of a fold on the steady state manifold. For the upper branch DZ point, it is hard to see the separated Hopf and SN$^+$ curves and the separated SE and SN curves because they are so close to each other. But our understanding of the bifurcation structure tells us the Hopf and the SE curves are on the left side of the SN$^+$ and the SN curves. The structures surrounded the two DZ points are identical. Both of them are the type I Y-shaped structures, the same as in Fig. 28(a) and Fig. 28(b).

The SE curve in Fig. 28(c) connects the two DZ points and the two Hopf curves into an integrated structure. It serves as a bridge between the upper branch and the lower branch of the steady state manifold. Without the SE curve, we would not be able to obtain the upper Hopf curve when we do the numerical continuation starting from a Hopf bifurcation point on the lower branch . This demonstrates one important application of the SE curves in finding new bifurcation hypersurfaces.

There is also a crossing of a Hopf curve and a SN curve in Fig. 28(c). It is structurally the same as in Fig. 28(b).

5.5 Stability regions

5.5.1 Stability regions and steady state manifold

Because of the complicated stability boundary structures discussed in the last section, the Gray-Scott network exhibits a wide variety of dynamics and stability regions. In the parameter space, there exist the following types of regions based on the steady state bifurcations. Even more complicated global dynamics is possible but will not be considered here.

1. Single stable region: There is only one stable steady state at every point in the region;
2. Single oscillation region: There is only one limit cycle oscillation at every point in the region;
3. Bistable region with two stable steady states: Two stable steady states coexist at every point in the region;
4. Region with one stable steady state and one oscillatory state: One stable steady state coexists with one limit cycle oscillation state at every point in the region;
5. Region with two oscillation states: Two oscillation states coexist at every point in the region.

In cases 1 and 2, the global dynamics has one attractor. In cases 3, 4 and 5, the global dynamics has two attractors. Every attractor has a region where trajectories go to the attractor. The region of the initial state determines which attractor will be reached. In other words, the two final states have their own *basins of attractions*. If the initial system state is within the basin of attraction of a particular final state (attractor), then the system dynamics will eventually bring the system onto that attractor.

There are three different types of steady state manifolds associated with each of the phase diagrams shown in Fig. 28. The first type is the typical mushroom-shaped steady state manifold. It contains two joined folds. There are three steady states in the folded regions and there is only one steady state in other regions. The second type is a combination of a single steady state manifold and a separated isola (a circle). This situation is the result of steady state manifold evolution started from a mushroom-shaped curve. When a second parameter such as the $\log[A]_0$ in Fig. 28(a) is adjusted, two nearby SN (or SN^+) points on the two folds of a mushroom-shaped curve can get closer and closer. After they meet at a certain point, a single steady state manifold and an isola emerge. The last type of steady state manifold contains a single steady state manifold only. It is the decaying product of either the first or the second type steady state manifold. The first decaying process starts from shrinking of the two folds on a mushroom-shaped steady state manifold. After passing through the cusp points, a mushroom-shaped steady state manifold becomes a single steady state manifold. The second decaying process goes through the shrinking of the isola in the second type of steady state manifold mentioned above. After the isola becomes a single point and then the point disappears, only a single steady state manifold is left.

5.5.2 Stability regions on the phase diagrams

The $(\log A_0, \log k_0)$ phase diagram in Fig. 28(a) can be divided into four regions:

a.1 a stable region containing lower stable steady states;

a.2 a region containing upper stable steady states and possible lower oscillation states;

a.3 a bistable region containing both upper and lower stable steady states;

a.4 a stable region containing upper stable steady states.

Similar analysis can be applied to the $(\log B_0, \log k_0)$ phase diagram in Fig. 28(b). The phase diagram consists of five stability regions

b.1 a stable region similar to a.1;

b.2 a region similar to **a.2**;

b.3 a bistable region similar to **a.3**;

b.4 a single oscillation region;

b.5 the tiny region in the neighbourhood of the left cusp point and the DZ point. Because a piece of the Hopf and a piece of the SN$^+$ curves are so close to each other in the neighbourhood, the existence of the region may not be noticed. A magnified picture of the region is shown on the right side to the Fig. 28(b). This region is very small, but dynamically it is very significant. In the region, steady states are on a fold. There are three unstable steady states at each point in the region. This is a region where two oscillation states could be found.

Stability regions on the $(\log k_1, \log k_0)$ phase diagram in Fig. 28(c) are qualitatively similar to those in Fig. 28(a) and Fig. 28(b). Refer to the symbols in the figure for stability properties of the regions.

VI. Stability boundaries of the bromate-sulfite-ferrocyanide network

The mechanism for the bromate-sulfite-ferrocyanide (BSF) reaction was proposed by Edblom, Luo, Orbán, Kustin and Epstein[25] (ELOKE) to account for experimentally observed oscillations and bistability of the reaction. The reaction is a counterpart of the iodate-sulfite-ferrocyanide oscillator discovered by Edblom, Orbán and Epstein (EOE)[58] but the mechanism is substantially different from that of the iodate oscillator[59,60].

I chose the BSF network for studies of stability boundaries because of the importance of bromate oscillators[61], and the extensive published experimental results. My initial intention was to enhance our understanding of this network, and explore the effects of various experimental parameters on its stability boundaries.

Surprisingly, my first calculation of unstable regions on steady state manifold showed quite different results than expected. A wide Hopf region of oscillation on the steady state manifold was missing. There was a fold in the experimental parameter region which suggested the existence of bistability at $[SO_3^{2-}]_0$ values where only oscillations were reported.

More investigation revealed that experimental results do not conflict with my calculation but must be given a new interpretation, as will be explained.

6.1 *The bromate-sulfite-ferrocyanide network*

The bromate-sulfite-ferrocyanide (BSF) network is composed of twenty-three reactions and twelve chemical species. Among the twenty-three reactions, nine of them are true chemical reactions, five are CSTR inflow reactions, and nine are CSTR outflow reactions. Among the twelve species, nine are dynamic intermediates, and three are major species or *down-stream species* whose concentrations do not affect chemical dynamics. The down-stream species are products that do not take part in other real reactions and are washed out of the system by the CSTR flow. Fig. 29 is a complete network diagram of the BSF network. All the twenty-three reactions are listed in Scheme IV.

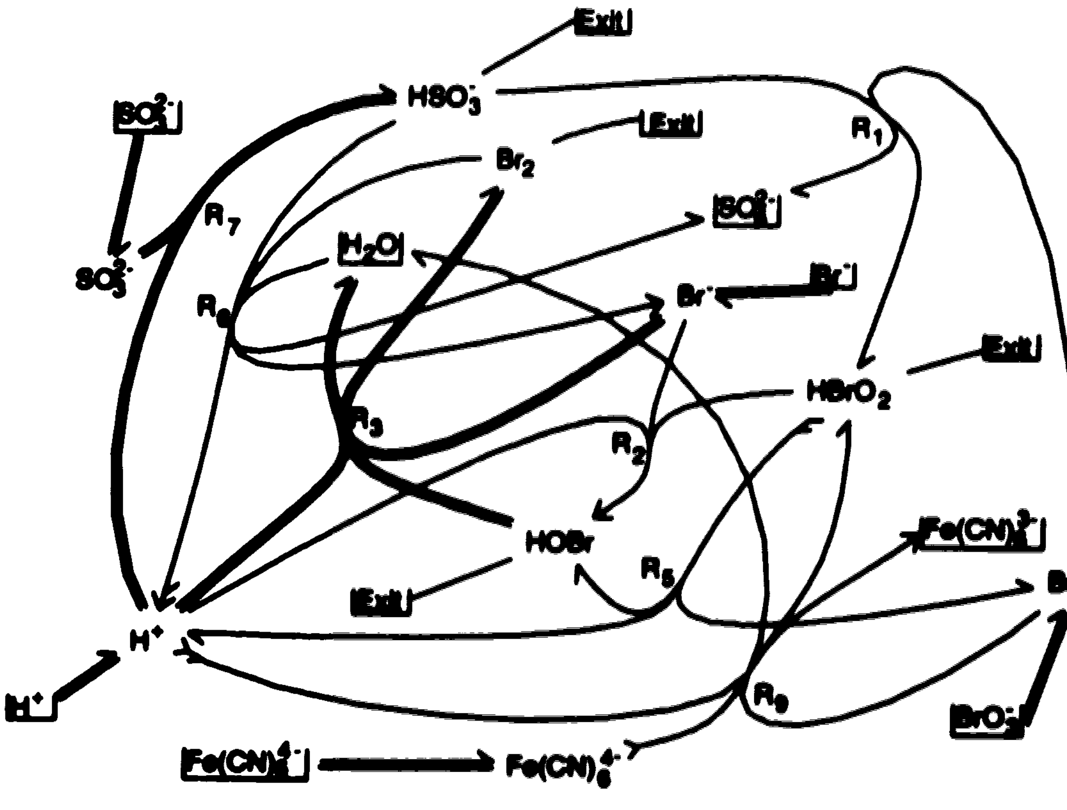

Fig. 29 Network diagram of the bromate-sulfite-ferrocyanide reaction network.

The symbols on the left column of Scheme IV are reaction numbers. True reaction numbers start with R, CSTR inflow reaction numbers start with I, and CSTR outflows start with O. The inflow reactions supply the reagents

Scheme IV:

R_1 $\mathrm{BrO_3^- + HSO_3^- \xrightarrow{k_1} HBrO_2 + SO_4^{2-}}$

R_2 $\mathrm{HBrO_2 + Br^- + H^+ \xrightarrow{k_2} 2HOBr}$

R_3 $\mathrm{HOBr + Br^- + H^+ \xrightarrow{k_3} Br_2 + H_2O}$

R_{-3} $\mathrm{Br_2 + H_2O \xrightarrow{k_4} HOBr + Br^- + H^+}$

R_5 $\mathrm{2HBrO_2 \xrightarrow{k_5} BrO_3^- + HOBr + H^+}$

R_6 $\mathrm{Br_2 + HSO_3^- + H_2O \xrightarrow{k_6} 2Br^- + SO_4^{2-} + 3H^+}$

R_7 $\mathrm{H^+ + SO_3^{2-} \xrightarrow{k_7} HSO_3^-}$

R_{-7} $\mathrm{HSO_3^- \xrightarrow{k_8} H^+ + SO_3^{2-}}$

R_9 $\mathrm{BrO_3^- + 2Fe(CN)_6^{4-} + 3H^+ \xrightarrow{k_9} HBrO_2 + 2Fe(CN)_6^{3-} + H_2O}$

I_1 $\mathrm{\{Br^-\} \xrightarrow{k_0} Br^-}$

I_2 $\mathrm{\{SO_3^{2-}\} \xrightarrow{k_0} SO_3^{2-}}$

I_3 $\mathrm{\{H^+\} \xrightarrow{k_0} H^+}$

I_4 $\mathrm{\{Fe(CN)_6^{4-}\} \xrightarrow{k_0} Fe(CN)_6^{4-}}$

I_5 $\mathrm{\{BrO_3^-\} \xrightarrow{k_0} BrO_3^-}$

O_1 $\mathrm{Br^- \xrightarrow{k_0}}$

O_2 $\mathrm{SO_3^{2-} \xrightarrow{k_0}}$

O_3 $\mathrm{H^+ \xrightarrow{k_0}}$

O_4 $\mathrm{Fe(CN)_6^{4-} \xrightarrow{k_0}}$

O_5 $\mathrm{BrO_3^- \xrightarrow{k_0}}$

O_6 $\mathrm{HSO_3^- \xrightarrow{k_0}}$

O_7 $\mathrm{HBrO_2 \xrightarrow{k_0}}$

O_8 $\mathrm{Br_2 \xrightarrow{k_0}}$

O_9 $\mathrm{HOBr \xrightarrow{k_0}}$

$Br^-, SO_3^{2-}, H^+, Fe(CN)_6^{4-}$, and BrO_3^-. On the diagram, these reactions are labelled with the species and cup-shaped symbols are drawn around the species. In the scheme, a pair of curly brackets instead of the cup-shaped symbol is used. The outflow reactions flush out the nine dynamical intermediates, which are $Br^-, SO_3^{2-}, H^+, Fe(CN)_6^{4-}, BrO_3^-, HSO_3^-, HBrO_2, Br_2$, and HOBr. The nine true chemical reactions affect chemical dynamics in different ways. The reactions R_1, R_2, R_3, R_{-3} and R_6 provide the auto-catalytic generation of H^+ and Br^- with the overall stoichiometry

$$BrO_3^- + 3HSO_3^- \longrightarrow Br^- + 3H^+ + 3SO_4^{2-}.$$

The disproportion of $HBrO_2$ (reaction R_5) is included to maintain $[HBrO_2]$ at a reasonable level. Reactions R_7, R_{-7} provide an equilibrium between sulfite and bisulfite. Reaction R_9 provides a negative feedback because of its high H^+ consumption.

Calculation shows that the BSF network contains twenty-eight extreme currents. The transpose of the complete extreme current matrix is shown on the next page. Among the twenty-eight currents, there are five CSTR flow-through currents. These are currents $\mathbf{E}_1$, $\mathbf{E}_4$, $\mathbf{E}_5$, $\mathbf{E}_6$, $\mathbf{E}_7$, which are the flows of Br^-, SO_3^{2-}, H^+, $Fe(CN)_6^{4-}$, BrO_3^- through the CSTR, respectively. Two other currents $\mathbf{E}_2$, $\mathbf{E}_3$ are detail-balanced currents. They provide the equilibria through the reactions (R_3, R_{-3}) and the reactions (R_7, R_{-7}) respectively. The remaining twenty-two extreme currents are chemical pathways that produce net chemical transformations.

Since there are twenty-three reactions ($r = 23$) and nine independent intermediates ($n = d = 9$), dimension of the current cone is $r - d = 14$. Any steady state can be expressed as a linear combination of fourteen extreme currents. In other words, there are fourteen non-zero j_i values for steady states where all reactions are

	R_1	R_2	R_3	R_{-3}	R_5	R_6	R_7	R_{-7}	R_9	I_1	I_2	I_3	I_4	I_5	O_1	O_2	O_3	O_4	O_5	O_6	O_7	O_8	O_9
$\mathbf{E}_{1}$	0	0	0	0	0	0	0	0	0	1	0	0	0	0	1	0	0	0	0	0	0	0	0
$\mathbf{E}_{2}$	0	0	1	1	0	0	0	0	0	0	0	0	0	0	0	0	0	0	0	0	0	0	0
$\mathbf{E}_{3}$	0	0	0	0	0	0	1	1	0	0	0	0	0	0	0	0	0	0	0	0	0	0	0
$\mathbf{E}_{4}$	0	0	0	0	0	0	0	0	0	0	1	0	0	0	0	1	0	0	0	0	0	0	0
$\mathbf{E}_{5}$	0	0	0	0	0	0	0	0	0	0	0	1	0	0	0	0	1	0	0	0	0	0	0
$\mathbf{E}_{6}$	0	0	0	0	0	0	0	0	0	0	0	0	1	0	0	0	0	1	0	0	0	0	0
$\mathbf{E}_{7}$	0	0	0	0	0	0	0	0	0	0	0	0	0	1	0	0	0	0	1	0	0	0	0
$\mathbf{E}_{8}$	0	0	0	0	0	0	1	0	0	0	1	1	0	0	0	0	0	0	0	1	0	0	0
$\mathbf{E}_{9}$	0	0	0	0	0	0	0	0	1	0	0	3	2	1	0	0	0	0	0	0	1	0	0
$\mathbf{E}_{10}$	1	1	2	0	0	2	3	0	0	0	3	0	0	1	1	0	0	0	0	0	0	0	0
$\mathbf{E}_{11}$	2	0	1	0	1	1	3	0	0	0	3	0	0	1	1	0	0	0	0	0	0	0	0
$\mathbf{E}_{12}$	0	1	2	0	0	0	0	0	1	3	0	6	2	1	0	0	0	0	0	0	0	2	0
$\mathbf{E}_{13}$	0	1	0	0	0	0	0	0	1	1	0	4	2	1	0	0	0	0	0	0	0	0	2
$\mathbf{E}_{14}$	0	0	1	0	1	0	0	0	2	1	0	6	4	1	0	0	0	0	0	0	0	1	0
$\mathbf{E}_{15}$	0	0	0	0	1	0	0	0	2	0	0	5	4	1	0	0	0	0	0	0	0	0	1
$\mathbf{E}_{16}$	1	0	0	0	0	0	1	0	0	0	1	1	0	1	0	0	0	0	0	0	1	0	0
$\mathbf{E}_{17}$	1	1	2	0	0	0	1	0	0	3	1	4	0	1	0	0	0	0	0	0	0	2	0
$\mathbf{E}_{18}$	1	1	0	0	0	0	1	0	0	1	1	2	0	1	0	0	0	0	0	0	0	0	2
$\mathbf{E}_{19}$	2	0	1	0	1	0	2	0	0	1	2	2	0	1	0	0	0	0	0	0	0	1	0
$\mathbf{E}_{20}$	2	0	0	0	1	0	2	0	0	0	2	1	0	1	0	0	0	0	0	0	0	0	1
$\mathbf{E}_{21}$	0	1	2	0	0	2	2	0	1	0	2	2	2	1	1	0	0	0	0	0	0	0	0
$\mathbf{E}_{22}$	0	0	1	0	1	1	1	0	2	0	1	4	4	1	1	0	0	0	0	0	0	0	0
$\mathbf{E}_{23}$	2	2	4	0	0	3	5	0	0	0	5	2	0	2	0	0	0	0	0	0	0	1	0
$\mathbf{E}_{24}$	1	1	1	0	0	1	2	0	0	0	2	1	0	1	0	0	0	0	0	0	0	0	1
$\mathbf{E}_{25}$	4	0	2	0	2	1	5	0	0	0	5	2	0	2	0	0	0	0	0	0	0	1	0
$\mathbf{E}_{26}$	0	2	4	0	0	3	3	0	2	0	3	6	4	2	0	0	0	0	0	0	0	1	0
$\mathbf{E}_{27}$	0	1	1	0	0	1	1	0	1	0	1	3	2	1	0	0	0	0	0	0	0	0	1
$\mathbf{E}_{28}$	0	0	2	0	2	1	1	0	4	0	1	10	8	2	0	0	0	0	0	0	0	1	0

occurring.

Using a thermally regulated CSTR[62], ELOKE found both sustained oscillations and hysteresis (bistability) in the BSF reactions[25]. They collected experimental points using parameters ($[SO_3^{2-}]_0, k_0$). Figure 30 is a replotted experimental phase diagram from reference (25) (experiments at 20°C).

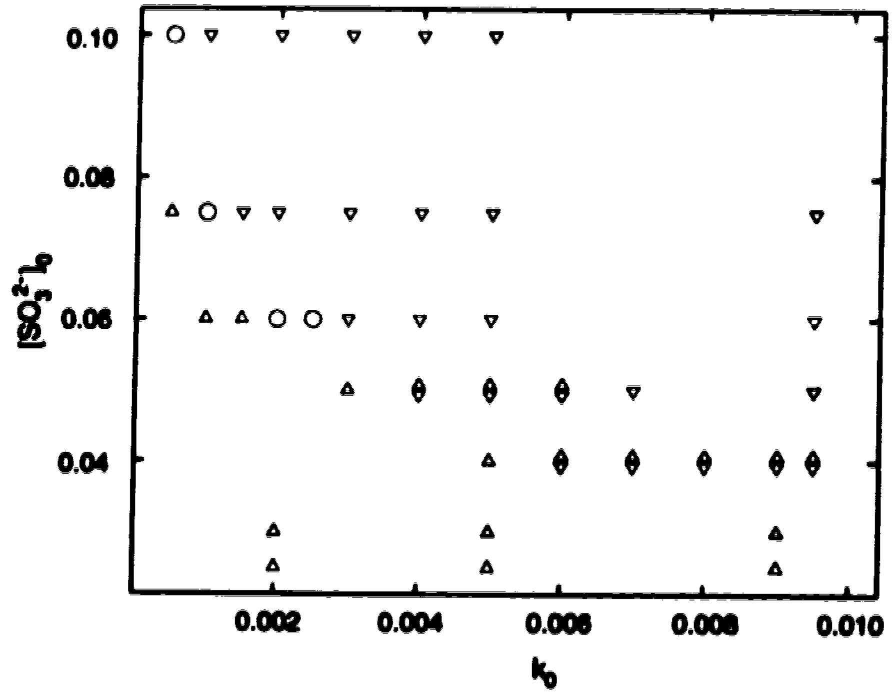

Fig. 30 Experimental points on a phase diagram in reference (25) (experiments at 20°C). This phase diagram and other similar phase diagrams were interpreted as cross-shaped. See Fig. 6 for the meaning of the symbols.

Their data appear to match cross-shaped phase diagrams, which have been observed in many reaction systems[24,59,64,65,66]. Their numerical integrations at selected parameter points using ROW4S[63] also agreed with a cross-shaped interpretation.

6.2 Searching for the oscillation region

To begin the detailed study of the BSF network, I first calculated a steady state manifold using parameter values given by reference (25). The results were unexpected.

Fig. 31 is a steady state manifold calculated at a cross section where $[SO_3^{2-}]_0 = 0.08M$. The graph seems to have nothing to do with the BSF system even though it is exactly produced from the BSF network.

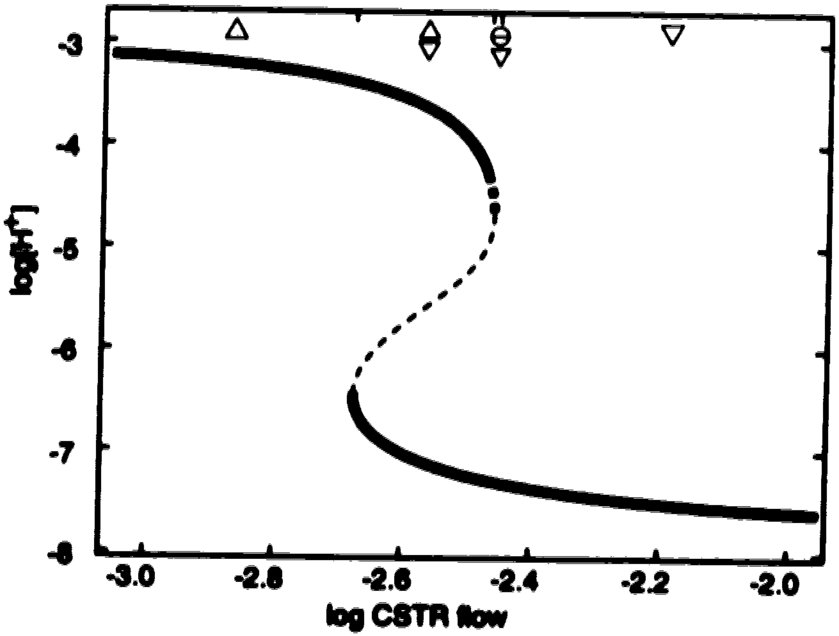

Fig. 31 A steady state manifold of the BSF network, calculated at $[SO_3^{2-}]_0 = 0.08M$. Other fixed parameters are $[BrO_3^-]_0 = 6.5 \times 10^{-2}M$, $[Br^-]_0 = 5.27 \times 10^{-7}M$, $[H^+]_0 = 2.0 \times 10^{-2}M$, $[SO_3^{2-}]_0 = 5.0 \times 10^{-2}M$, $[Fe(CN)_6^{4-}]_0 = 2.0 \times 10^{-2}M$, $k_1 = 8.0 \times 10^{-2}M^{-1}s^{-1}$, $k_2 = 9.5 \times 10^6 M^{-2}s^{-1}$, $k_3 = 1.6 \times 10^{10} M^{-2}s^{-1}$, $k_4 = 1.1 \times 10^1 s^{-1}$, $k_5 = 3.0 \times 10^3 M^{-1}s^{-1}$, $k_6 = 1.0 \times 10^6 M^{-1}s^{-1}$, $k_7 = 5.0 \times 10^{10} M^{-1}s^{-1}$, $k_8 = 3.0 \times 10^3 s^{-1}$, $k_9 = 3.2 \times 10^1 M^{-2}s^{-1}$.

First, all experiments and numerical integrations in reference (25) pointed out that at $[SO_3^{2-}] = 0.08M$ most steady states are stable, except for some oscillation states in a low flow rate region. This can be seen from Figure 30. This suggests that the steady state manifold does not have a fold and it only has an unstable region bounded by Hopf bifurcations. In contrast, Fig. 31 has a fold that indicates the existence of a bistability region. Although it has a region between the Hopf and the SN^+ points on the upper branch, as shown by a short piece of thick-dashed curve, the region is very small compared to the wide experimental oscillation region. A careful examination of dynamic trajectories in this small region showed that no oscillations exist. Trajectories always end at the points on the lower branch of the fold.

There are two questions to be answered here. Where are the oscillations found by ELOKE? What is the origin of the fold and the bistability that I found?

I first thought that I could have set the parameters different from ELOKE. The only ambiguity is the CSTR input concentration $[H^+]_0$ from the CSTR reservoir. Reference (25) mentioned that $[H_2SO_4]_0 = 1.0 \times 10^{-2}M$. If the starting solution is quite basic as pointed out by the reference, then both H^+'s should dissociate from the H_2SO_4 and we should use $[H^+]_0 = 0.02M$, which is what I actually used. If we take the partial dissociation of the second H^+ into consideration, then a lower $[H^+]_0 = 0.0145M$ should be used. So, I decided to try this new $[H^+]_0$ to see if it made a difference.

I did see a difference in the steady state manifold and stability regions. But the difference appeared only at much lower CSTR flow rates than the experimental parameter range. Fig. 32 shows a steady state manifold (a) and an oscillation (b) that occurred at $\log k_0 = -9.7376$. It is obvious that the oscillation is not the one that I was looking for. On the steady state manifold, there is a barely noticeable Hopf point on the upper branch very close to the most upper-right folding (SN^+) point. This small region cannot provide us with the desired oscillations either.

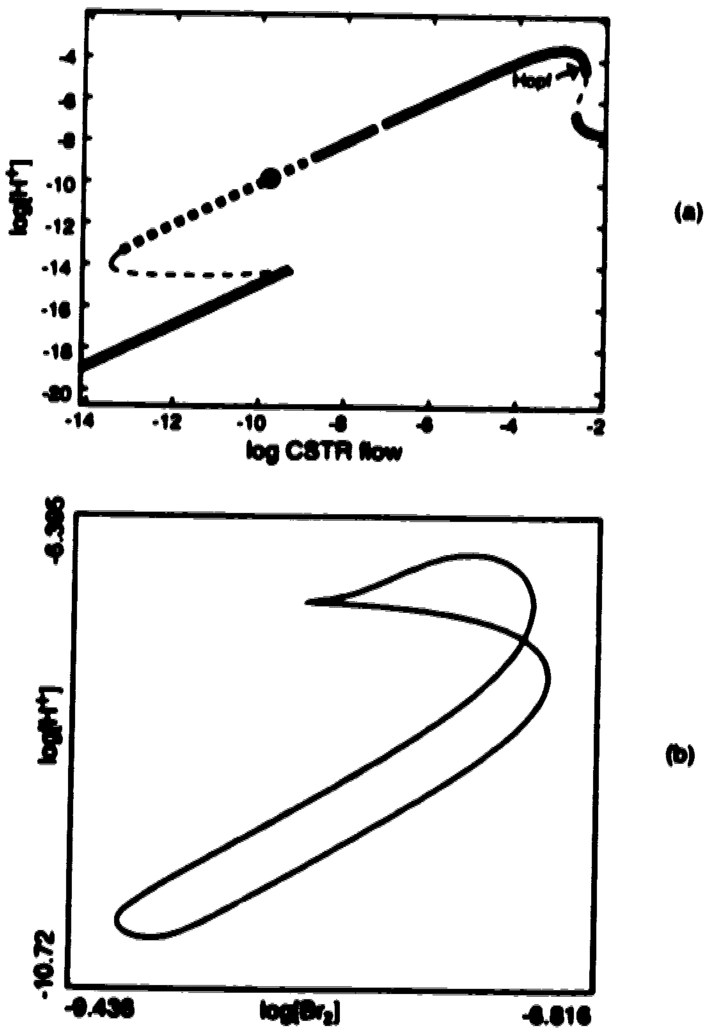

Fig. 32 (a) A steady state manifold and (b) an oscillatory trajectory of the BSF network. CSTR input concentration $[H^+]_0 = 0.0145M$ is used for the calculation. The oscillatory trajectory is calculated at $\log k_0 = -9.7376$. This is much lower than the real experimental parameter range. All other parameters are the same as in Fig. 31

Another possible way to get a large region of oscillations is to widen the small region between the Hopf and the SN$^+$ points on the upper-right corner of Fig. 32(a) by adjusting some of the other experimental parameters. Since the steady states in this region are within the basin of attraction of the lower stable branch, an oscillation region would be produced only if we could extend the unstable region far enough to the left so that the Hopf point could go across the lower SN point in the parameter space. To achieve this goal, I needed to adjust some rate constants.

Analysis of important currents at the Hopf bifurcation point shows the rate constant k_9 must be changed. This matches the experimental observation that oscillations appeared only after $Fe(CN)_6^{4-}$ was added and reaction R_9 occurred. Calculations show that when the rate constant k_9 is increased, the Hopf bifurcation point moves toward the left. This makes the region between the Hopf point and the upper SN$^+$ point become larger. It is found that $k_9 \approx 200.59 M^{-2}s^{-1}$ is the minimum k_9 value to cause a crossing of the Hopf and the lower SN points in the experimental parameter range. Fig. 33 is the steady state manifold calculated at $[SO_3^{2-}]_0 = 0.10018M$ and $k_9 = 200.59 M^{-2}s^{-1}$. Notice that the upper branch Hopf point and the lower SN point occur at approximately the same CSTR flow rate. The k_9 value that causes crossing at the experimentally observed position is near $k_9 = 250 M^{-2}s^{-1}$.

The results are still not convincing for two reasons. One is that the k_9 values are too big compared to the optimized value $32.5 M^{-2}s^{-1}$ in reference (25) and Birk and Kozub's value[67] $39.5 M^{-2}s^{-1}$ ($[H^+] = 10^{-4.5}, \frac{1.25 \times 10^{-3}}{10^{-4.5}} = 39.5$). Another more important reason is that when k_9 is made as large as in Fig. 33, the region of bistability extends to infinitely high flow rate at low $\log [SO_3^{2-}]_0$. Experimentally the bistable region falls within a closed curve at $30°C$ and $40°C$.

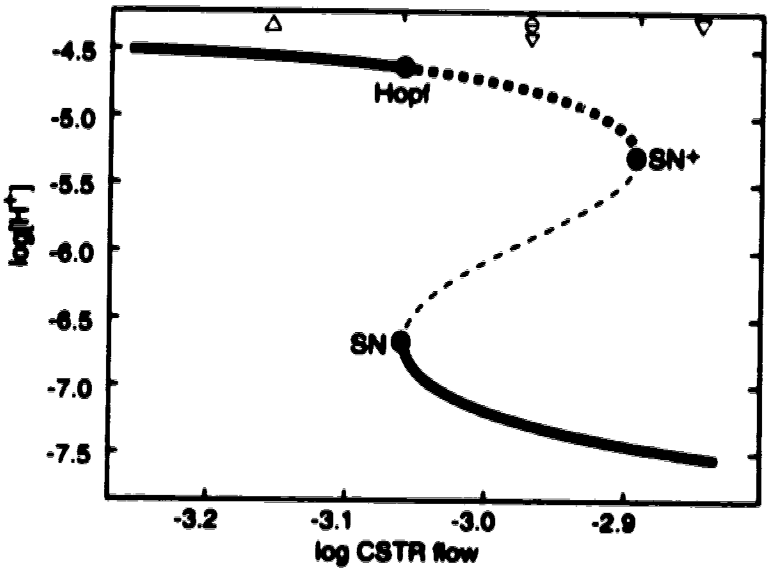

Fig. 33 Steady state manifold of the BSF network at $[SO_3^{2-}]_0 = 0.10018M$, $k_9 = 200.59M^{-2}s^{-1}$ and $[H^+]_0 = 0.145M$. The k_9 value is the minimum to cause a crossing of the Hopf and the lower branch SN points within the experimental parameter range. All other parameters are the same as in Fig. 31.

It is now clear that the difference between my results and ELOKE's results is not caused by using $[H^+]_0 = 0.02M$. There was one other possible way an oscillatory region might occur. This would involve a limit cycle which coexists with the upper stable steady state. Such limit cycles sometimes occur when the Hopf bifurcation is subcritical. The oscillatory region typically ends at a *saddle-node of periodic solution(SNP)*[68]. The details will be explained later.

To test this idea, I dragged the cursor on the upper branch of Fig. 31 to a little lower k_0 value than that of the lower SN point. Then I dragged the system state point **X** a little off the steady state on the dynamics screen of the SNA package. The new system state **X** was used as the starting point of a numerical integration. The dynamic trajectory soon approached a limit cycle and started a sustained oscillation. A careful examination proved this is the oscillation that I was looking for.

To make sure this understanding of the oscillation is correct, I tried to find trajectories that ended at a stable steady state at the same parameter point. I quickly found trajectory 1 shown in Fig. 34 . The trajectory coexists with other trajectories such as trajectories 2 and 3 on the graph, which eventually become limit cycles. Fig. 34 demonstrates the coexistence of a limit cycle oscillation and a stable steady state. The trajectory approaching the stable steady state is inside the limit cycle. All the trajectories were calculated using the same system of differential equations and the same parameter settings. The only difference between the trajectories is the initial point. The approach of the trajectories to two different attractors confirmed the reason for the oscillations discussed above.

6.3 Stability boundaries of the BSF network

6.3.1 Cross-shaped phase diagrams

In experimental studies of nonlinear chemical systems, the phase diagrams often appear cross-shaped as shown in Fig. 35. Detailed calculations show that complicated dynamics usually occur near the crossing point. Epstein and Luo showed that strictly cross-shaped phase diagrams occur for differential delay equations when two of the parameters are restricted[69]. This is a special case where there must be a relationship between the parameters to obtain the cross-shaped phase diagram. (In their studies, $\tau = \frac{1}{\mu}$). The crossing is often a very simplified picture of what actually happens.

The important issue here is the distinction between typical phase diagrams which can be considered cross-shaped if the fine detail is neglected, and the situation

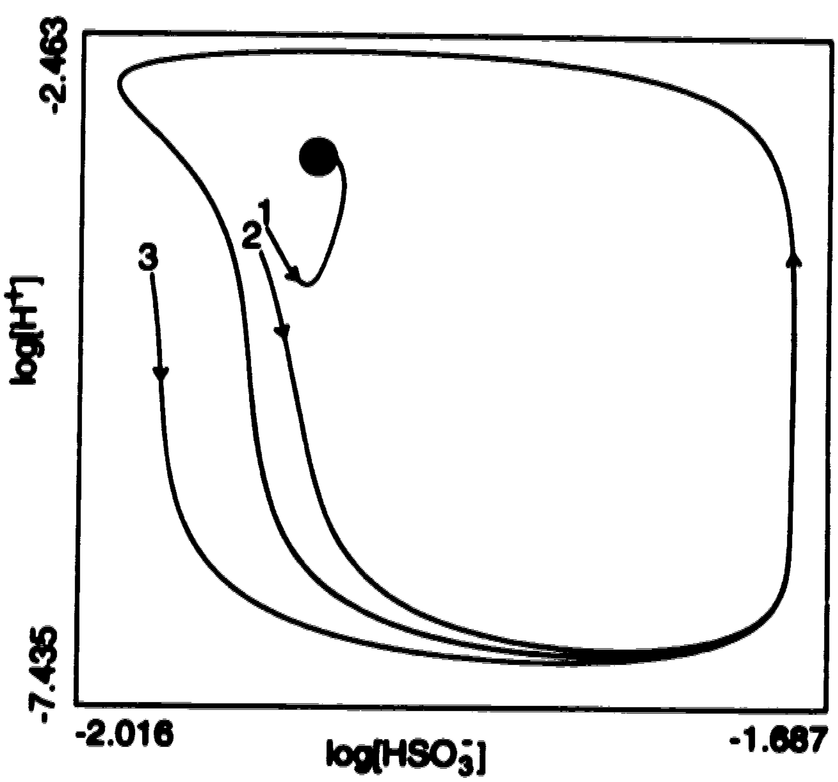

Fig. 34 Two different types of dynamic trajectories calculated from the same set of parameter values. The difference is caused by different initial conditions. The trajectories indicate the coexistence of a stable steady state (trajectory 1) and a sustained oscillation (trajectories 2 and 3). The dark dot stands for the stable steady state. Parameters: $[SO_3^{2-}]_0 = 0.08M; k_0 = 0.0020s^{-1}$; all other parameter values are the same as in Fig. 31. The starting points are obtained by dragging the cursor on the screen from the stable steady state to the desired starting points of the individual trajectories.

in the BSF network which is very different. Since I found oscillations at parameter values which correspond to stable steady states, I questioned the validity of the cross-shaped diagram interpretation of the BSF network data. As I will discuss later, the phase diagrams of the BSF network cannot be made into cross-shaped phase diagrams no matter what changes in the network are used. While many published

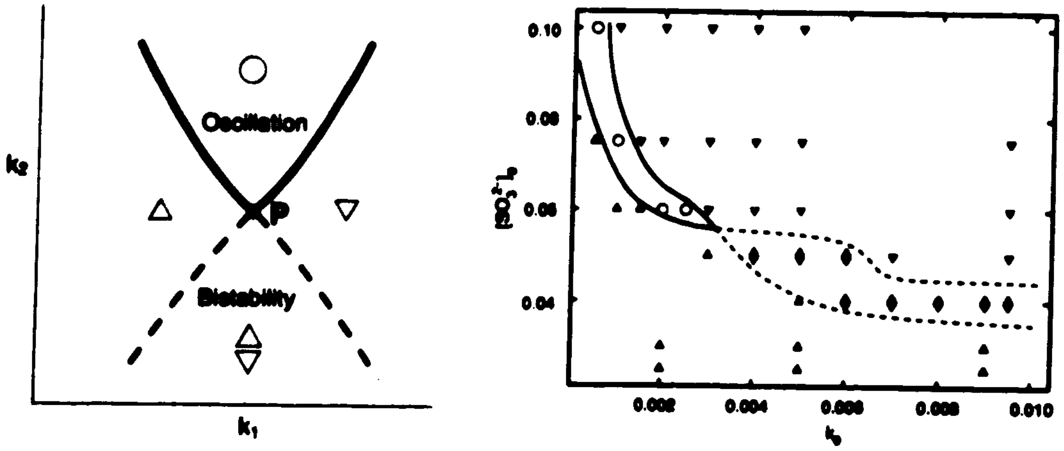

Fig. 35 Cross-shaped phase diagrams. Left: general shape. Right: the BSF data appears consistent with a cross-shaped phase diagram using estimated stability boundaries of ELOKE (replotted). The solid curves represent boundaries for the oscillation region, and the dashed curves represent boundaries for the bistable region. The point P is the crossing point.

cross-shaped phase diagrams are truly close to being cross-shaped, I believe at least some of them are not intrinsically cross-shaped at all. The BSF network is a representative of the later type.

6.3.2 Unexpected stability boundaries of the BSF network

The oscillations in the BSF network are associated with a subcritical Hopf bifurcation, which extends the region of oscillation an unusually large distance beyond the Hopf bifurcation point. This wide region is called a ***subcritical Hopf overlap***. The oscillations occur at the parameter points where corresponding steady states are stable. Fig. 36 is a qualitative bifurcation diagram to illustrate the idea. On the diagram, the upper branch can be divided into four segments.

The segment farther to its right is a tiny region bounded by the Hopf and the SN^+ bifurcation points. Steady states in the segment are unstable. There are

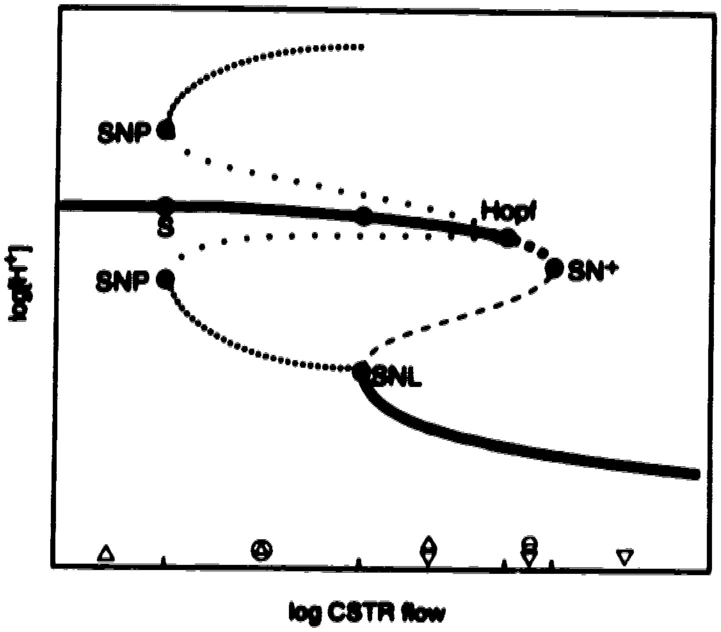

Fig. 36 A qualitative bifurcation diagram of the BSF network. $[SO_3^{2-}]_0 > 0.068M$. The curve is reshaped in order to illustrate the ideas more clearly. In addition to the steady state manifold, branches of oscillatory trajectories are also plotted. The sparse-dotted branch is a branch of unstable limiting cycles. The dense-dotted branch is a branch of stable limit cycles. SNP is a saddle-node of periodic solution. SNL is a saddle-node on a loop. All other parameters are the same as those in Fig. 31.

two conceivable attractors to trajectories in this parameter range. One is a limit cycle surrounding the unstable steady state. The other is the stable steady state on the lower branch at the same parameter point. In the case of the BSF network, the trajectories started near the upper branch unstable steady states always approach the lower branch steady states. Limit cycles do not exist in this region. Experimentally we only observe one stable steady state for each k_0 value in this region.

In the second segment, k_0 starts from the Hopf bifurcation point and ends at the lower SNL point (SNL means *saddle-node on a loop*[68]). Steady states in the segment are stable. They are surrounded by an unstable periodic solution. The unstable periodic solution is a repeller that pushes dynamic trajectories away from it. When a trajectory starts between the upper stable steady state and the unstable periodic solution, the trajectory will be attracted to the upper stable steady state. When a trajectory starts outside the unstable periodic solution, it is attracted to the stable steady state on the lower branch. Experimentally we cannot observe oscillations in the region. We should be able to observe two stable steady states for each k_0 value. The two stable steady states are located on the upper branch and the lower branch respectively.

The third segment is from the point where the second segment ends to the point S where the limit cycles end. In this range, there are a stable steady state, an unstable limit cycle and a stable limit cycle for each k_0 value. The difference between this segment and the second segment is that this segment is outside the folding region of the steady state manifold so that there is only one steady state for each k_0 value. The lack of the lower branch means that the dynamic trajectories started between the unstable limit cycle and the possible stable limit cycle can only be attracted to the limit cycle. Trajectories started between the unstable limit cycle and the stable steady states are still attracted to the steady states on the upper branch. Therefore, at every experimental CSTR flow rate in this region, we should be able to observe the coexistence of a sustained oscillation and a stable steady state.

The segment to the left of the point S is the fourth segment. In this segment, there is a unique stable steady state for each CSTR flow rate.

The steady states on the lower branch of the fold are all stable. The region for k_0 greater than the k_0 at the SN^+ point is a region with a unique stable steady state.

Based on the bifurcation structure discussed above, the stability regions as k_0 is increased from lower flow rates to higher flow rates should be in the order of:

- upper stable steady state only;
- coexistence of the upper stable steady state and oscillation;
- bistability between the upper and lower stable steady state;
- lower steady state only.

Fig. 37(a) shows calculated stability boundaries on the (k_0, $[SO_3^{-2}]_0$) parameter plane. The thick-long-dashed line is the SN^+ bifurcation curve, which is the right boundary of the upper steady states. It is difficult to see the SN^+ curve because it almost coincides with the thick-solid Hopf bifurcation curve. The thin-dashed line is the SN curve, which is the left boundary of the lower steady states. The upper part of the SN curve coincides with the right half boundary of the oscillation region when $[SO_3^{2-}]_0 > 0.068M$. The thick-dotted lines are boundaries of the oscillation region. The two large regions at the upper-right and the lower-left corners of Fig. 37 (a) are stable with a single lower and upper stable steady state respectively. The region between the Hopf and SN curves is the bistable region containing two stable steady states. The region between the thick-dotted lines on the upper-left of the plot is the region where the oscillations exist. The upper branch stable steady states also exist in this region. So the region is actually a region of coexistence of oscillations and upper stable steady states. Fig. 37(b) is a counterpart of Fig. 37(a) in the log space.

At each cross section of Fig. 37 above the DSN point (*Double Saddle Node point*), there is a bifurcation diagram similar to Fig. 36. From Fig. 37, we can see

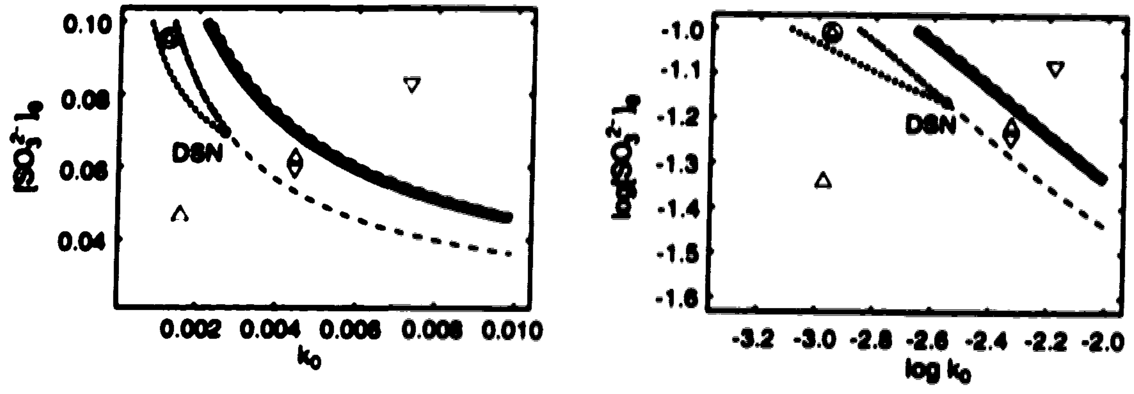

(a) (b)

Fig. 37 Stability boundaries of the BSF network. (a) on the (k_0, $[SO_3^{-2}]_0$) parameter plane; (b) on the ($\log k_0, \log [SO_3^{-2}]_0$) parameter plane. All parameters are the same as those in Fig. 31 except k_0 and $[SO_3^{-2}]_0$. Hopf: thick-solid curves; SN: thin-dashed curves; SN$^+$: thick-long-dashed curves; Oscillation boundary: thick-dotted curves.

that throughout most of the range covered by the $[SO_3^{2-}]_0$, the fold and bistability exist. The oscillations only occur in the high $[SO_3^{2-}]_0$ range above the DSN point. When we scan the whole $[SO_3^{2-}]_0$ range from the top, we first see a bifurcation structure represented by Fig. 36. The four stability regions listed above all exist at the higher $[SO_3^{2-}]_0$ values. Lowering the $[SO_3^{2-}]_0$ moves all stability boundaries to the higher CSTR flow rate region. At the same time, the oscillation-containing region becomes narrower. At $[SO_3^{2-}]_0 \approx 0.068M$, the oscillations disappear because left boundary of the oscillation region (the SNP point) meets the boundary of the SN (SNL) curve at the DSN point. All dynamic trajectories that were originally attracted to the limit cycle will be attracted to the lower stable states after we pass this point. As a result, only bistable regions for two stable steady states and single stable regions occur when $[SO_3^{2-}]_0 < 0.068M$. No oscillations occur below the DSN point.

It is obvious that the stability boundaries in Fig. 37 are not cross-shaped.

In next section, I will show how to interpret the cross-shaped phase diagrams obtained from the experiments and numerical integrations using our non-cross-shaped stability boundaries.

6.4 Why were experimental phase diagrams previously considered to be cross-shaped?

6.4.1 Comparison of my stability boundaries with previous numerical simulations

Let's compare my stability boundaries with the calculated phase diagrams published in reference (25).

The stability boundaries in the published phase diagrams were drawn on the basis of numerical integrations at some selected points on the parameter plane. To avoid human prejudice in interpreting computer-generated data, the correct comparison would be to use only calculated data points (not the original phase diagram) from the publication and my calculated stability boundaries. Since there were no numerical data published, I measured the locations of all published data points in Fig. 6 (a) of the reference and replotted all the points on my own phase diagrams. The results are shown in Fig. 38 in both non-log and log spaces. The numerical data corresponding to the points are listed in Appendix 3.

My stability boundaries are consistent with most of the published data points. All published bistable points fit into my region of bistability between two stable steady states. All published points with oscillations fit into my region of bistability between a stable steady state and an oscillation with one exception. The exception is the circle on the most upper-left corner. It was published as an oscilla-

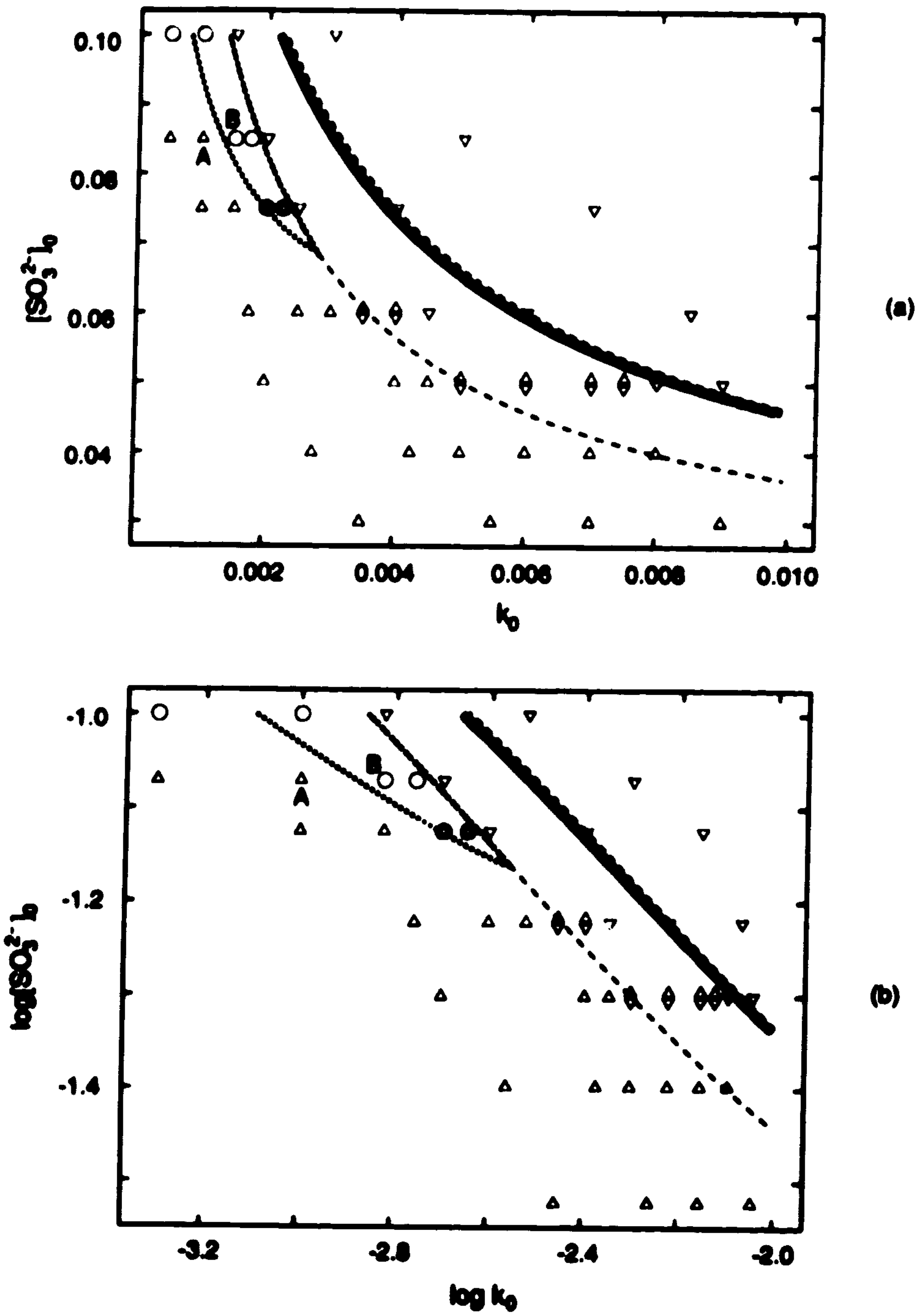

Fig. 38 Comparison of the published data points based on numerical integrations with my calculated stability boundaries of the BSF network. All parameters and line patterns are the same as those in Fig. 37.See Fig. 6 for the meaning of the symbols.

tion point. But both my stability boundaries and my numerical integrations showed that it should be a point where only an upper steady state exists. All published stable steady state points fit into the correct regions of my diagram. Indeed, my region of bistability between two stable steady states includes the published points of lower steady states. Therefore, there are no fundamental differences as far as the computer calculations are concerned. However, the published results are only a partial reflection of all dynamic features. A phase diagram that gives a complete picture is needed.

It is not strange to see that only partial results were obtained by the numerical integration method. Results of numerical integrations depend on the initial points chosen. When there is more than one attractor and one of the attractors has a much larger basin of attraction than the other attractors, the chances of choosing an initial point in the smaller attracting basin are small.

This is one reason that the published BSF data are incomplete. On the upper branch of Fig. 36, the region between the stable steady states and the unstable limit cycles is very narrow. Among many points picked up for calculations in reference (25), only two of them were started in that narrow region. The results of the two calculations were shown by ELOKE on the graph with the circled triangles. If the two points were investigated further and a clear understanding of stability boundaries were obtained, more information would have been collected.

What phase diagrams would have emerged if we had failed to start our numerical integrations in the narrow range between the stable steady states and the unstable limit cycle? I will start our analysis from the SN^+ point in Figure 36 and use the same segment division designated in the last section. The farthest right segment is obviously not affected. The upper stable steady states in the second segment would escape detection. We would conclude there are only lower steady states in the k_0 range corresponding to the second segment. Then the distinction between the first and the second segment would not exist. We would get a single large region having only lower steady states. Further to the left, the upper steady states would escape detection again and we would conclude the third segment is a region with only one attractor, a limit cycle oscillation.

What would happen to the situations where $[SO_3^{2-}]_0 < 0.068M$? In these situations, the segment 3 (oscillation region) has disappeared. Fig. 39 shows how Figure 36 must be modified for this situation. A lower $[SO_3^{2-}]_0$ has pushed the point where limit cycles ends (the SNP point) inward into the folding region. The original SNP point becomes a *homoclinic loop bifurcation point* (HL)[68]. The point divides the k_0 range corresponding to the fold into two parts. On the left part, the steady states on the upper and the lower branches attract their neighbouring dynamical trajectories without being influenced by any other attractors or repellers. Both steady states would be easily detected by numerical integrations. On the right, there still exists a narrow region between the upper stable steady states and the unstable limit cycles. Failing to start numerical integrations within the narrow region would still cause all trajectories be attracted to the lower steady states. The corresponding k_0 range would appear to be a single steady state region and it would be combined into the region on its right to form a large single steady state region.

These scenarios explain how ELOKE missed some of the dynamical possibilities of the BSF system and obtained data that was consistent with a cross-shaped phase diagram. When $[SO_3^{2-}]_0 > 0.068M$, one would find only a single oscillation region on the left part of the graph. When $[SO_3^{2-}]_0 < 0.068M$, one would find only a bistability region on the right part of the graph. The two regions join at a point where $[SO_3^{2-}]_0 \approx 0.068M$. This is the point where the k_0 on the left boundary

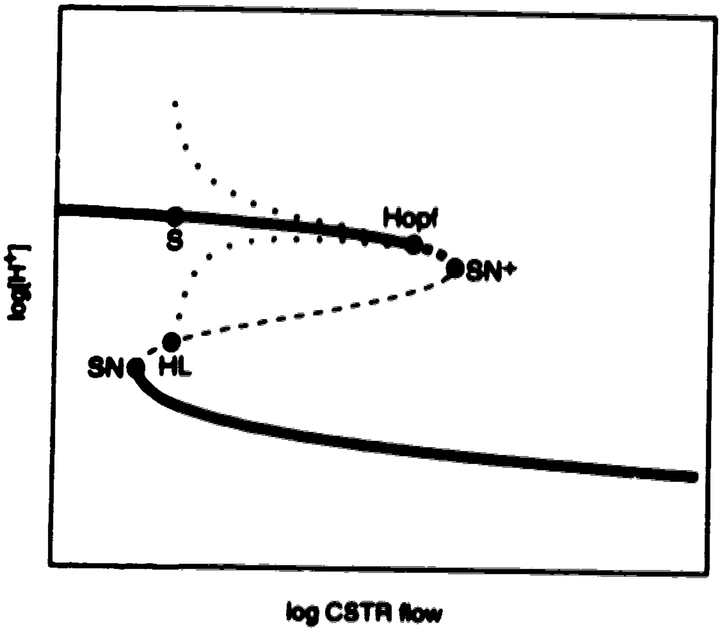

Fig. 39 A qualitative bifurcation diagram of the BSF network when $[SO_3^{2-}]_0 < 0.068M$. All symbols, patterns and other parameters are the same as those in Fig. 36. HL is a homoclinic loop bifurcation point.

of the oscillation region coincides with the k_0 at the lower SNL point. It makes a perfect cross-shaped phase diagram.

Fig. 40 gives six dynamic trajectories calculated at three points on the $(k_0, [SO_3^{2-}]_0)$ parameter plane. Fig. 40(a) shows my calculated stability boundaries, the selected points for calculating dynamic trajectories, and the correct stability features of the selected points. The letters beside the selected points indicate the figure number for the corresponding trajectories.

Trajectories calculated at the selected point b are shown on the following plots (b.1) and (b.2). Point b is at $k_0 = 1 \times 10^{-3}s^{-1}, [SO_3^{2-}]_0 = 0.10M$. It is located in the oscillation region on the cross-shaped phase diagram and in the region of bistability between the upper steady states and the oscillations on my

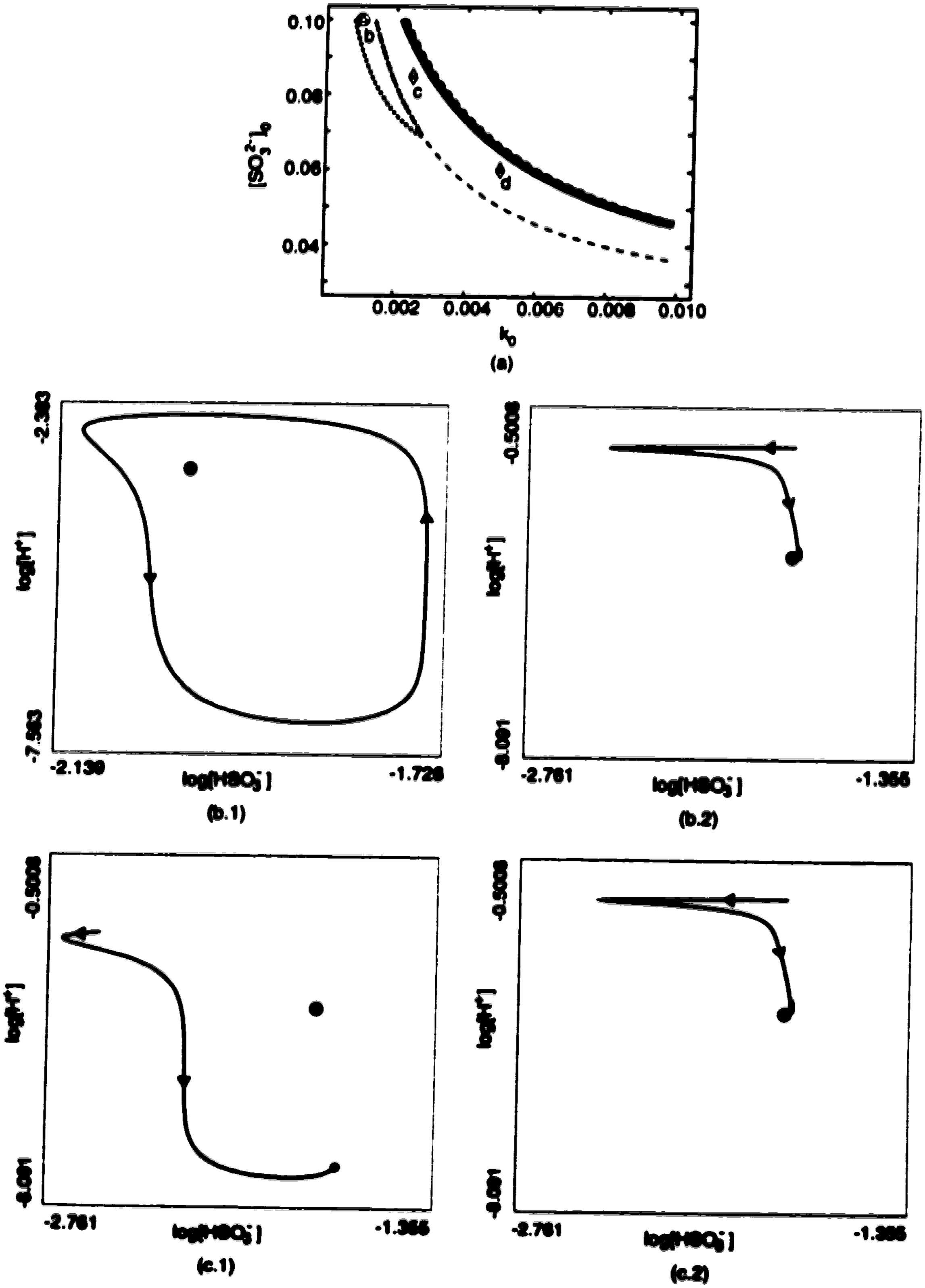

(a)

(b.1)

(b.2)

(c.1)

(c.2)

Fig. 40 (to be continued on next page)

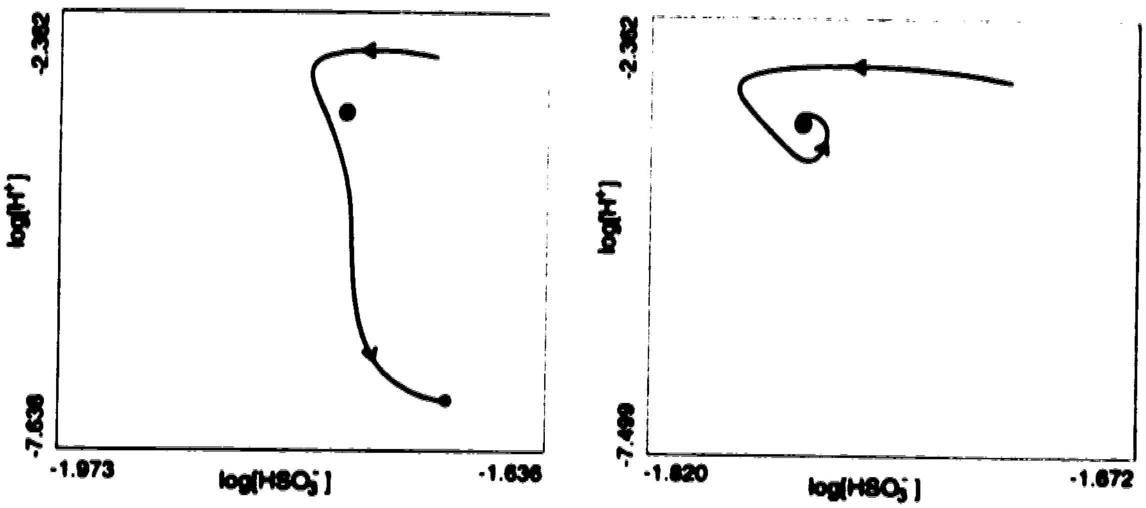

(d.1) (d.2)

Fig. 40 Trajectories at three selected points on the $(k_0, [SO_3^{2-}]_0)$ parameter plane. They match with non-cross-shaped stability boundaries. But they do not fit into the cross-shaped phase diagrams. (a) locations and stability properties of the three selected points on my calculated phase diagram; (b.1)(b.2) trajectories at the point b, $k_0 = 1 \times 10^{-3} s^{-1}, [SO_3^{2-}]_0 = 0.10M$; (c.1)(c.2) trajectories at the point c, $k_0 = 2.5 \times 10^{-3} s^{-1}, [SO_3^{2-}]_0 = 0.085M$; (d.1)(d.2) trajectories at the point d, $k_0 = 5 \times 10^{-3} s^{-1}, [SO_3^{2-}]_0 = 0.06M$. Big dots are the upper steady states that we start with. All starting points of integrations are obtained by moving a steady state point to a neighbouring point as shown on the graphs. Small dots are steady states on the lower branch of the fold. Some trajectories end at these points. All other parameters are the same as those in Fig. 31.

phase diagram. Two different types of trajectories presented in Fig. (b.1) and Fig. (b.2) support my conclusions. Fig. (b.1) shows a stable limit cycle. Fig. (b.2) gives a trajectory ending at an upper steady state.

Fig. (c.1) and Fig. (c.2) are two trajectories ended at two different steady states. They demonstrate the coexistence of two steady states in the region represented by the selected point c. They match with my calculated phase diagram. They contradict the conclusion that the point c is located in the region of single lower steady states based on the cross-shaped phase diagram.

Trajectories at point d are shown in Fig. (d.1) and Fig. (d.2). My calculated phase diagram agrees with the cross-shaped phase diagram. Both phase diagrams predict the coexistence of two steady states at the point although the justifications for the stability classification are different. My prediction is based on the fact that the points c and d are both located in the same large region of bistability. The cross-shaped phase diagrams were prepared assuming that the points c and d belong to two different regions. From Fig. (d.2), we can also clearly see that the upper steady state at the point d is a stable focus. It supports the explanations presented in Fig. 39, i.e., there is an unstable periodic solution surrounding each stable steady state. The unstable periodic solution acts as a repeller while the steady state is an attractor to the nearby dynamic trajectories.

6.4.2 Comparison of my stability boundaries with the experimental data

It is more complicated to compare my stability boundaries with the published experimental data. There are two reasons for this. First, the BSF network matches experiments only qualitatively when the proposed rate constants are used. Second, the experiments are subject to the same interpretation problems as the numerical integrations. Setting starting points for the experiments is similar to choosing initial conditions for numerical integrations. They could lead to only a partial discovery of the system features. Explaining the experimental results is a challenge.

I have treated the published experimental points in the same way as I have done on the data points produced by the numerical integrations. Careful measurements of points on the published experimental phase diagrams produced the data sets listed in Appendix 3. Then I replotted the points on my phase diagrams. The results are shown in Fig. 41.

There are three sets of data for experiments at $20^oC, 30^oC$ and 40^oC. Fig. 41(a), (b) and (c) compare my calculated stability boundaries with the three experimental data sets. None of the data sets fit the calculated stability boundaries very well. Actually, the same differences also exist between the results of numerical integrations and the experiments in the original publication[25].

By careful examination of Fig. 41, we found that the basic shapes of our stability boundaries match with the experimental results. For Fig. 41(a) and (b), if we could move our stability boundaries toward the lower-left corner of the graphs without incurring a change in the shapes of the stability boundaries, we would be able to catch most experimental bistability points in our correct region of bistability, and to catch experimental oscillatory points in our region where oscillations exist. I will discuss this topic in more detail in Section 6.6.

6.5 A procedure for locating all attractors at a phase diagram point

The most important mandate for theoretical investigations is to explain the experimental results and develop experimental procedures. My research results have clearly shown the correct stability boundaries. We have also understood the reason why cross-shaped phase diagrams are inappropriate. Therefore, we are in a position to develop a procedure for experiments and numerical integrations which yields correct phase diagrams.

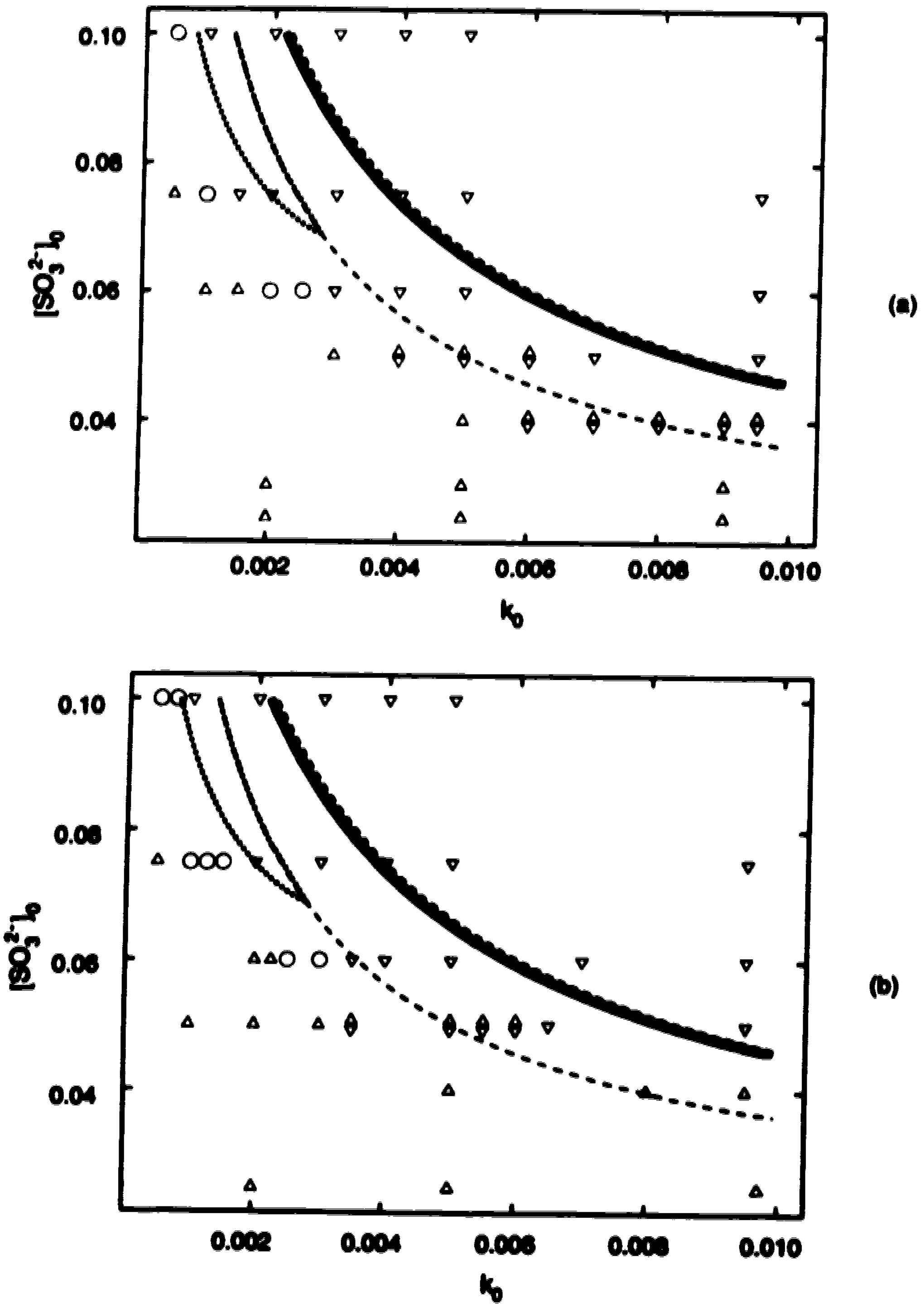

Fig. 41 (to be continued on next page)

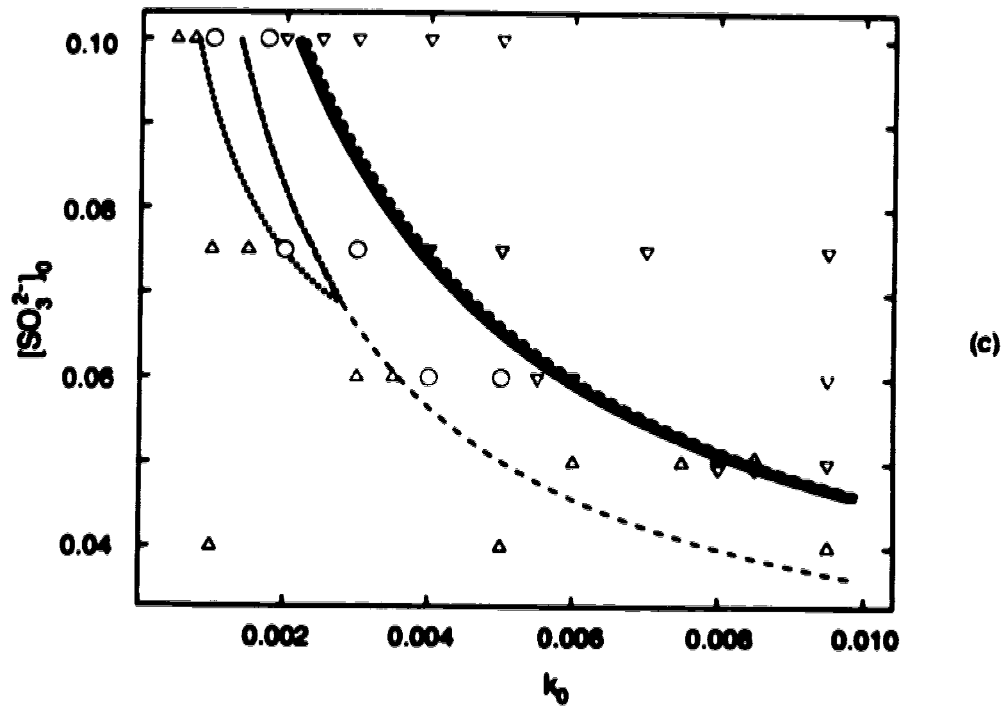

Fig. 41 Comparison between the calculated stability boundaries and the experimental results. (a) comparing with the experiments at 20^oC; (b) comparing with the experiments at 30^oC; (c) comparing with the experiments at 40^oC.

I have pointed out that numerical integration at the selected points could give us only a partial picture of all dynamic features. But the numerical integration method still has a special feature of which we could take advantage. It is a very close simulation of real chemical processes in the laboratory. In the laboratory, we set up certain experimental conditions and then start up an experiment at a certain initial system state. In theoretical investigations using the numerical integration method, we specify a set of parameters, which are the counterparts of the experimental conditions. We also select a starting point, which is similar to an initial experimental system state, to do the numerical integration. This is parallel to running an experiment on a computer instead of running it in a chemistry laboratory. This close similarity could produce problems like the one that we discussed for the BSF network. But it can also be used to simulate real experiments very closely with a good model like the BSF network. Using our understanding of stability boundaries of the network, we will develop an investigation strategy using computer simulations. If the numerical simulation can get correct results, we should be able to apply it to the real chemical experiments and to confirm all system features. Since experiments are not part of this thesis, I will focus on exploring the missed features using numerical integration.

Look at Fig. 38 again and imagine how we could use numerical integration to simulate experiments. In an experiment, we set up a set of experimental conditions. In our case, we set up a CSTR reservoir concentration $[SO_3^{2-}]_0$ and a flow rate k_0 along with some other fixed parameters. We run the experiment from a certain initial state. After some time, the system will reach either a stable steady state or a sustained oscillatory state. Then we change one of our parameters to a new value. In most cases, we adjust our flow rate. Then the system will evolve from the state we just achieved to a new stable or oscillatory state. In a numerical simulation, we do exactly the same thing as we did in the real experiment in the hope of duplicating the experimental results. In Fig. 38, let's assume our first point is the point A. Numerical integration leads the system to a stable upper steady state. Then we change the flow rate to the point B. More numerical integration will bring us to an oscillatory state. This way, we get the same conclusion on the stability as the experiment did. However, we actually missed a stable steady state that coexists with the oscillatory state.

The reason for failing to detect the coexisting stable steady state can be seen from Fig. 42. The figure is somewhat exaggerated to show the idea clearly. After the system settles at the stable steady state S_0, at the flow rate A discussed above, an adjustment of the flow rate to the point B in Fig. 38 brings the system state to the point P in Fig. 42. Point P is within the basin of attraction of the stable limit cycle, so, we get a sustained oscillation.

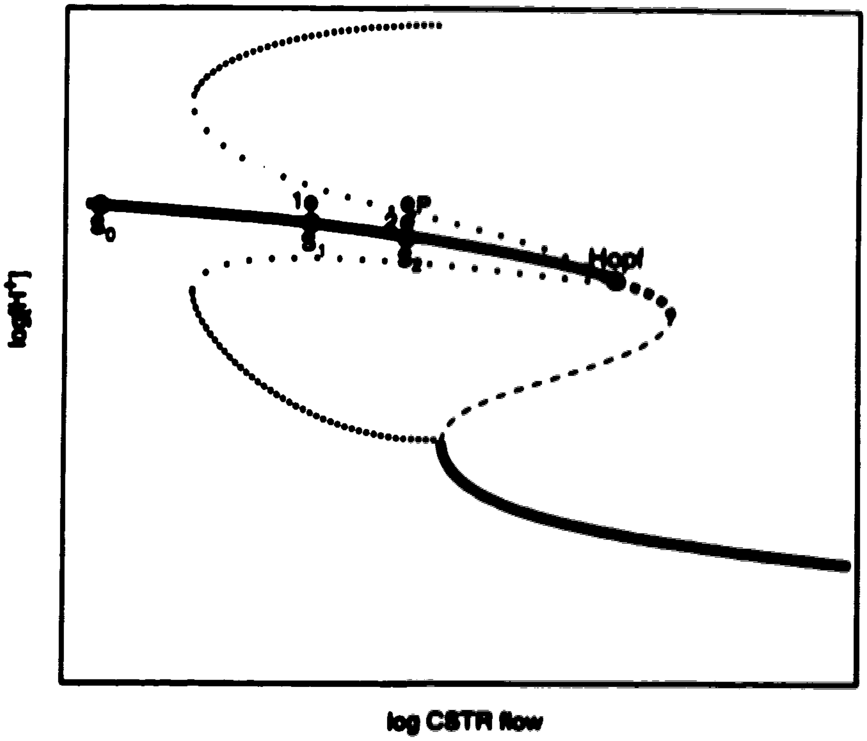

Fig. 42 Why the upper stable steady states were not detected and how to detect them. A big adjustment of flow rate k_0 moves the system from the steady state S_0 to the point P. The system will be attracted to the stable limit cycle when P is used as a new starting point. Using smaller adjustment of k_0 can avoid the problem. The system states will be changed in the sequence of $S_0 \rightarrow 1 \rightarrow S_1 \rightarrow 2 \rightarrow S_2$.

It is not difficult to find the oscillation when we scan the k_0 range back from the high CSTR flow rate. It is difficult to find the coexisting steady state. From Fig. 42, we see that the answer is to adjust the CSTR flow rate slowly near the stability boundaries. The pattern of adjustment shown on the figure carries the system from the state S_0 to state 1 by adjusting the flow rate, then to S_1 by integration, then to 2 by the flow rate adjustment again, and so on. This way, we can always detect the upper stable steady state with desired accuracy.

Dynamic trajectories in Fig. 43 show the differences in final states when we adjust the flow rate at different step sizes for the BSF network. Fig. 43(a) is a trajectory at the point A in Fig. 38, where k_0 is $1 \times 10^{-3}s^{-1}$. The trajectory ends at a stable upper steady state. Then we change k_0 so that we get to the point B in Fig. 38, where k_0 is $1.5 \times 10^{-3}s^{-1}$. The numerical integration at the point B gives the trajectory in Fig. 43(b). The resulting state is an oscillatory state. Fig. 43(c) is what happens when we adjust k_0 from $1 \times 10^{-3}s^{-1}$ to $1.5 \times 10^{-3}s^{-1}$ using three smaller step sizes. The adjustment is in the sequence of $1 \times 10^{-3}s^{-1} \rightarrow 1.25 \times 10^{-3}s^{-1} \rightarrow 1.40 \times 10^{-3}s^{-1} \rightarrow 1.50 \times 10^{-3}s^{-1}$. For $k_0 = 1.25 \times 10^{-3}s^{-1}$, the trajectory ends at a stable steady state S_1. Then k_0 is changed to $1.40 \times 10^{-3}s^{-1}$ while keeping all other parameters and concentrations fixed. A new round of numerical integration carries the trajectory to a new stable steady state S_2. Changing k_0 again to $1.50 \times 10^{-3}s^{-1}$, we conduct one more step of numerical integration. The trajectory finally lands on a stable steady state S_3 instead of the oscillatory state shown in Fig. 43(b). Hence, we find the upper stable steady state that was missed before.

In a real experiment, it might take a lot of time to adjust the flow rate slowly. If this is a real concern, a strategy such as a bisection method should be applied when we see a sudden change of dynamic features. If a well-established model is available, it is strongly suggested to calculate stability boundaries first. Then use a combination of the stability boundaries and the numerical integration method to explore the possibility of the existence of other dynamic features. This procedure should bring us to the interesting parameter region quickly. Then a thorough experimental investigation should be conducted in the specific region.

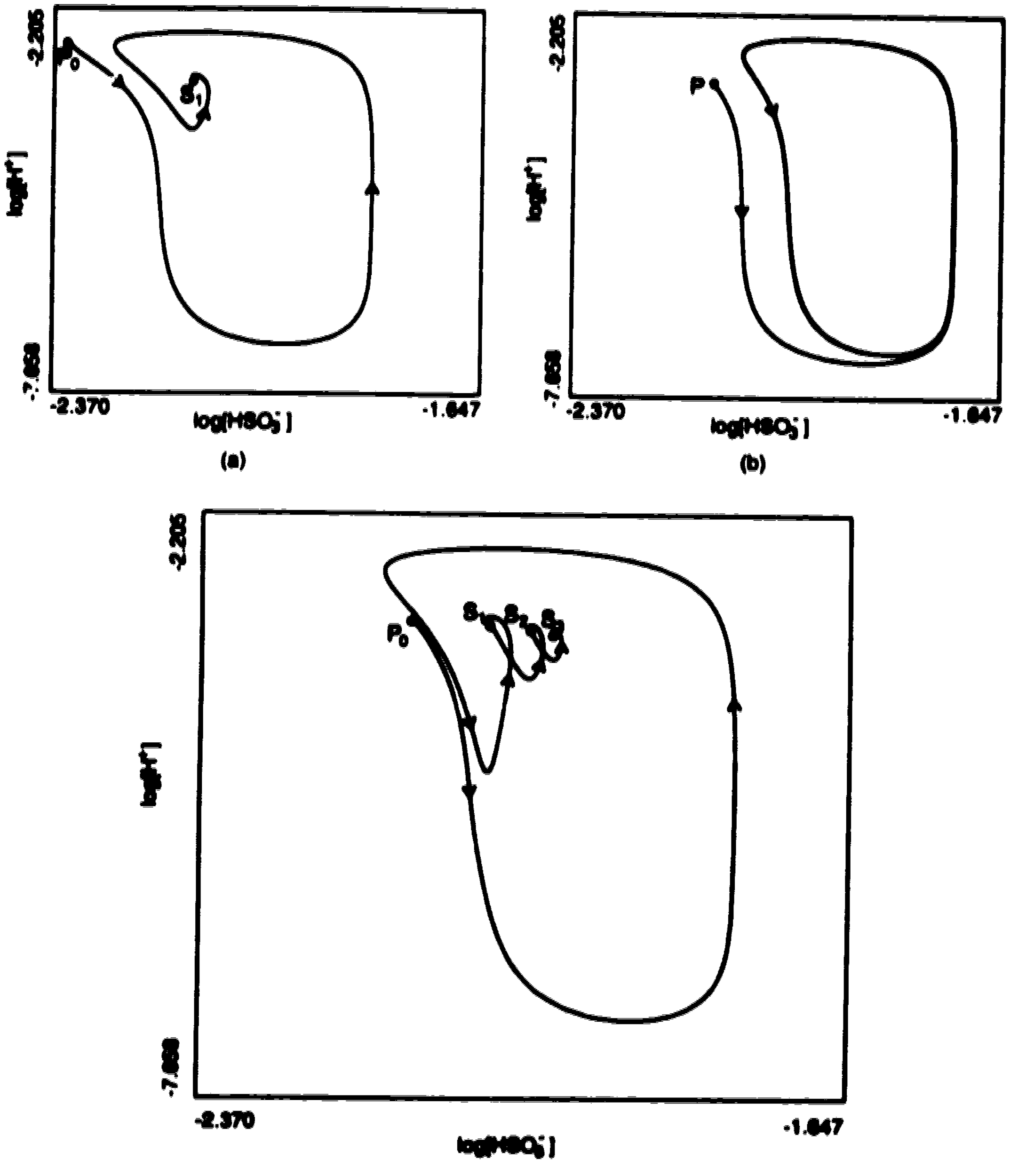

Fig. 43 Trajectories of the BSF network when $[SO_3^{2-}]_0 = 0.085M$. (a) A trajectory ends at an upper steady state; (b) A trajectory ends on an oscillatory state. The starting point of the trajectory in (b) is the same as the final stable steady state of the trajectory in (a) except that k_0 has been adjusted from $1 \times 10^{-3}s^{-1}$ to $1.5 \times 10^{-3}s^{-1}$; (c) A trajectory still ends at the upper steady state. The final k_0 for the trajectory in (c) is the same as that for the trajectory (b). But the change of k_0 has been taken in three smaller step sizes.

6.6 Adjusting rate constants to fit experimental results

From Fig. 41, we have seen that the BSF network does not quantitatively match any set of the experiments conducted at $20^oC, 30^oC$ and 40^oC. The problem is not caused by the reaction mechanism. My studies show that the rate constants can be adjusted to fit experimental results. I will use the 20^oC experiments as an example to show how to modify the rate constants.

Fig. 44 is a plot in log space that compares my calculated stability boundaries with the experimental points at 20^oC. As discussed in section 6.4.2, we want to move our stability boundaries SN and SN^+ to the left to include all experimentally observed bistable points between the SN and the SN^+ boundaries. We also need to move the oscillation region boundary to the lower left to catch all experimental oscillation points in our calculated region of oscillation.

According to the slope pattern discussed in section 4.4, parameters $[BrO_3^-]_0, k_1, k_2, k_5, k_6, k_7$ affect the positions of the bistable boundaries. Numerical calculation shows that the stability boundaries are especially sensitive to a small adjustment in k_1. Changing k_1 causes the SN and the SN^+ boundaries to move in the same direction without noticeably changing the width of the bistable region between them. The effect of changing k_1 on the boundary of the oscillation region is also desirable. It does not change the slopes of the oscillatory boundary so that treatment of the oscillatory boundary can be conducted separately. All these facts related to k_1 suggest that k_1 is an ideal candidate which should be adjusted first. The slope pattern derived in section 4.4 indicates that k_1 should be lowered to move the boundaries of the bistable region to the left of the phase diagram on the $(\log [SO_3^{2-}]_0, \log k_0)$ plane.

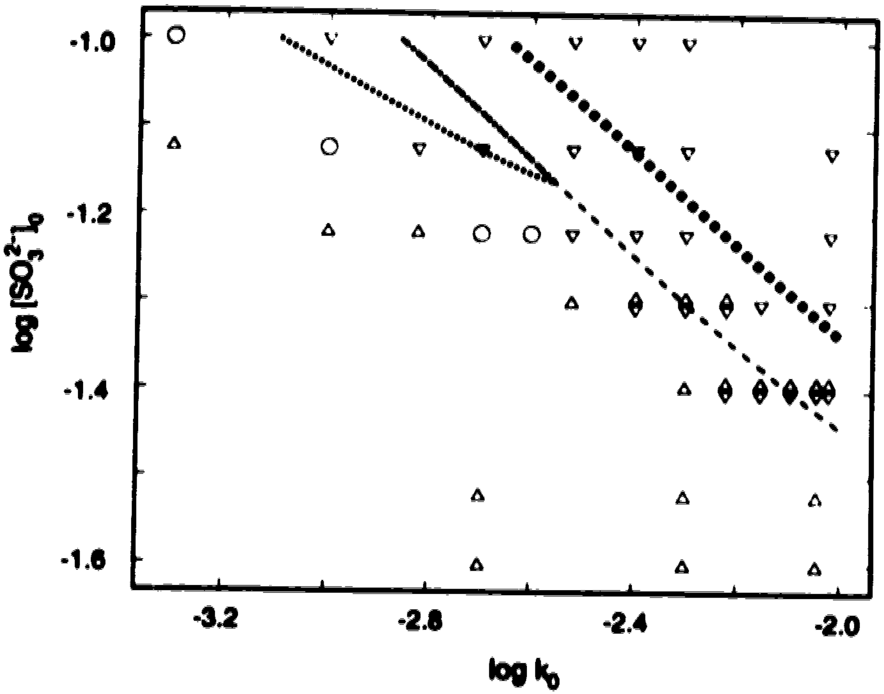

Fig. 44 Comparison between the calculated stability boundaries and the experimental results at 20^oC. Original rate constants in reference (25) are used. The rate constants need to be modified in order to match the calculated stability boundaries with the experimental results.

Fig. 45 shows the calculated stability boundaries for the 20^oC experiments after k_1 has been changed from $8.000 \times 10^{-2} M^{-1}s^{-1}$ to $5.765 \times 10^{-2} M^{-1}s^{-1}$. We see that all experimentally observed bistable points are in the region between the SN and the SN$^+$ boundaries. Other experimental points in the region were reported to have only a single lower steady state. It disagrees with the prediction based on the stability boundary calculations. However, this disagreement is understandable because of the narrow basin of attraction caused by the subcritical Hopf bifurcation for the upper steady states. Using the strategy discussed in Section 6.5, a second stable steady state should be detected for all the experimental points in the region.

The next step is to fix the problem associated with the boundaries of the

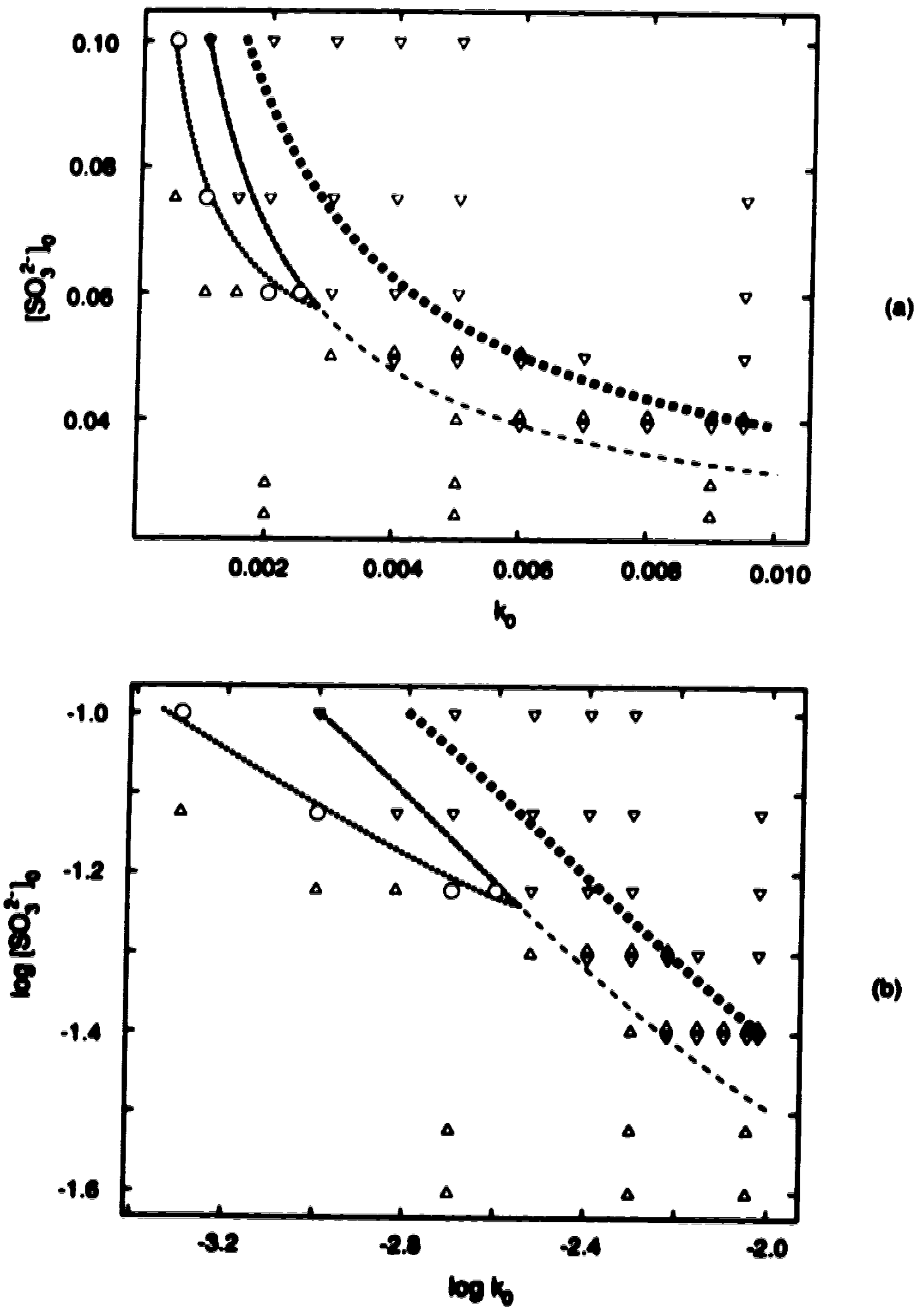

Fig. 45 Comparison of the calculated stability boundaries with the experimental results at $20°C$ after k_1 is adjusted from $8.000 \times 10^{-2} M^{-1}s^{-1}$ to $5.765 \times 10^{-2} M^{-1}s^{-1}$. All experimentally observed bistable points are in the calculated bistable region. (a) in the conventional parameter space; (b) in the log space. All other parameters are the same as those in Fig. 31.

oscillation region. The right boundary of the region always coincides with the SN boundary because of the existence of the saddle-node on a loop(SNL) bifurcation structure illustrated by Fig. 36. As long as the SN boundary is moved to the desirable position as we already did, the right boundary of the oscillation region is determined.

According to Fig. 45, left boundary of the oscillation region needs to be moved downward so that we can get a wider oscillation region to accommodate all experimentally observed oscillatory points. Since this boundary consists of saddle-nodes of periodic solutions (SNP), it is related to global system dynamics. It cannot be determined from the local steady state features only.

There exists some information that can help us to find the right parameter for the adjustment. As I mentioned in section 6.2, key extreme currents associated with the Hopf bifurcation all contain reaction R_9. Experiments also demonstrated that the oscillations appeared only after ferrocyanide was added to the bromate-sulfite system so that reaction R_9 occurs in the system. Since the oscillations here are directly related to the subcritical Hopf bifurcation, its boundary must be related to reaction R_9. Hence, adjustment of k_9 should change position of the boundary for the oscillation region.

Fig. 46 and Fig. 47 show two comparisons of calculated stability boundaries with experiments at 20^oC after k_9 is adjusted. In Fig. 46, k_9 is changed from $32.5M^{-2}s^{-1}$ to $49.5M^{-2}s^{-1}$ while all other parameters are kept constant. All experimental oscillation points are now located in the newly calculated oscillation region. Although we call the region an oscillation region, real dynamics in the region is actually the coexistence of oscillations and the upper stable steady states as discussed previously. One suspicious experimental point that I cannot explain using the calculated stability boundaries is the point P in Fig. 46. The original experiment should have produced either a single upper steady state, an oscillatory state or a combination of an upper steady state and an oscillation. From the figure, we can conclude that $49.5M^{-2}s^{-1}$ is approximately the upper limit for the k_9 value we can use. A bigger k_9 value will move the boundary of oscillation region too much to the left and cause discrepancies between the experimental and the calculated results.

A better choice of k_9 value is $k_9 = 39.5M^{-2}s^{-1}$. Fig. 47 is calculated using this k_9 value. The experimental and calculated results also match very well on the figure except the suspicious point P. The main difference between Fig. 46 and Fig. 47 is the location of the curve where the oscillation region ends.

As mentioned earlier, the left boundary of the oscillation region is a SNP (saddle-node of periodic solutions) curve while right boundary of the region is a SNL (saddle-node on a loop) curve. The ending point of the region is a point where the SNP and the SNL curves join. A normal SN curve also joins the SNP and the SNL curves at the point. This is a codimension 2 bifurcation point. In Fig. 47, the point is located at $[\mathrm{SO}_3^{2-}]_0 \approx 5.22 \times 10^{-2}M$. All experimental bistable points were found at lower $[\mathrm{SO}_3^{2-}]_0$ values than this theoretical value at the ending point of the oscillation region. This is understandable because at lower $[\mathrm{SO}_3^{2-}]_0$ values, bifurcation diagrams have the qualitative shape shown on Fig. 39. It is much easier to detect two stable steady states in a range between the SN and the HL (homoclinic loop) as I explained before. So, Fig. 47 not only shows the match between experimental and calculated results, it also accounts for the fact that some bistable points were observed experimentally but some were missed in experiments. In Fig. 46, the ending point of the oscillation region is located at $[\mathrm{SO}_3^{2-}]_0 \approx 4.71 \times 10^{-2}M$. Even though the calculated stability boundaries can

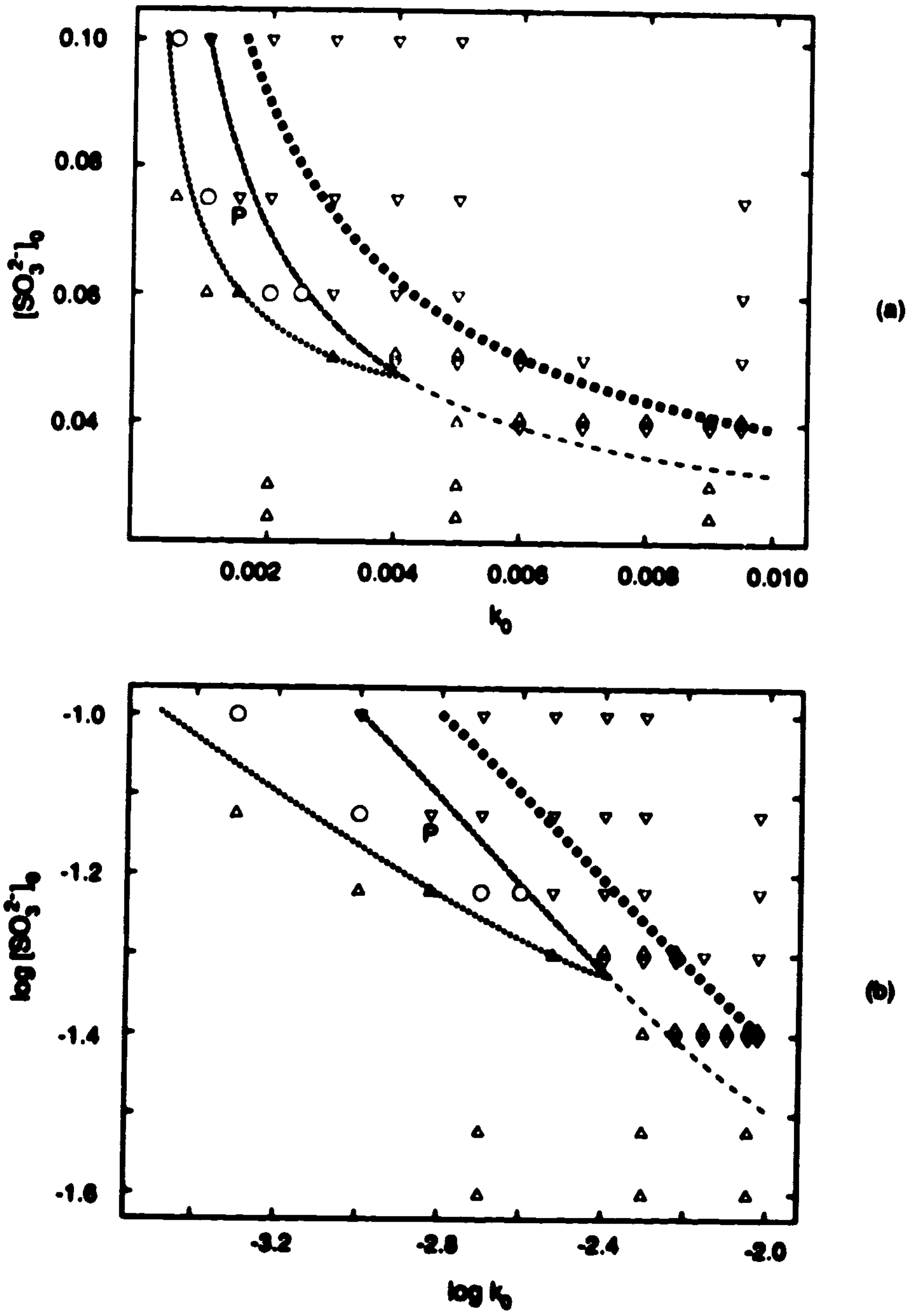

Fig. 46 Comparison of the calculated stability boundaries with the experimental results at 20^oC after k_1 is adjusted from $8.000\times10^{-2}M^{-1}s^{-1}$ to $5.765\times10^{-2}M^{-1}s^{-1}$ and k_9 is adjusted from $32.5M^{-2}s^{-1}$ to $49.5M^{-2}s^{-1}$. All experimentally observed dynamic features are contained in the corresponding calculated regions except the point P. (a) in the conventional parameter space; (b) in the log space. All other parameters are the same as those in Fig. 31.

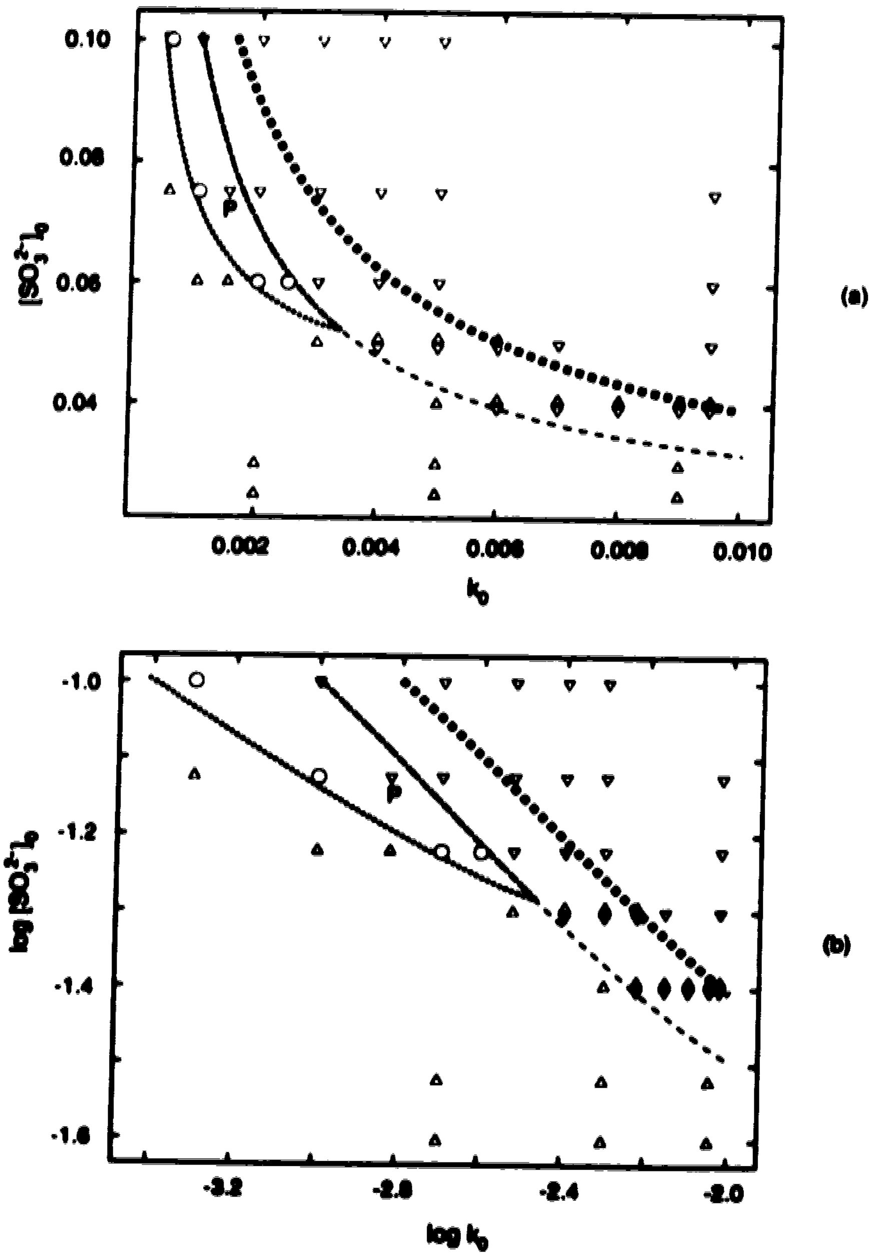

Fig. 47 Comparison of the calculated stability boundaries with the experimental results at $20°C$ after k_1 is adjusted from $8.000 \times 10^{-2} M^{-1} s^{-1}$ to $5.765 \times 10^{-2} M^{-1} s^{-1}$ and k_9 is adjusted from $32.5 M^{-2} s^{-1}$ to $39.5 M^{-2} s^{-1}$. All experimentally observed dynamic features are contained in the corresponding calculated regions except the point P. The figure also explains why some bistable points were detected in experiments but some bistable points were not detected. (a) in the conventional parameter space; (b) in the log space. All other parameters are the same as those in Fig. 31.

accommodate all experimental points except point P in the figure, it cannot explain why some bistable points were detected experimentally, but some points were not detected. Therefore, $k_9 = 39.5M^{-2}s^{-1}$ should be our chosen k_9 value.

The complete phase diagram at 20^oC for the experimental points is shown in Fig. 48. All experimentally observed dynamic features (except one point discussed above) match the calculated stability boundaries very well. The phase diagram also shows the features which were missed at the various experimental points.

6.7 Important chemical pathways for the steady state bifurcations of the BSF reaction network

In this section, I will examine the chemical pathways responsible for the Hopf and the SN bifurcations.

6.7.1 The minimum set of unstable combinations of extreme currents

There are twenty-eight extreme currents in the BSF network. They correspond to twenty-eight chemical pathways for the network to achieve steady state. The transpose of the complete extreme current matrix was given in Section 6.1. To find sources of instability in the network, I have conducted a computational search for the minimum set of unstable combinations of currents. The calculation shows that there are ten unstable extreme currents. There are also twenty-seven combinations of two stable currents are unstable. That is to say, the two stable currents in each combination combine to produce instability. No combinations of three stable currents can produce instability. Therefore, we can conclude that the instabilities in the BSF network are caused by at least one of following thirty-seven unstable combinations.

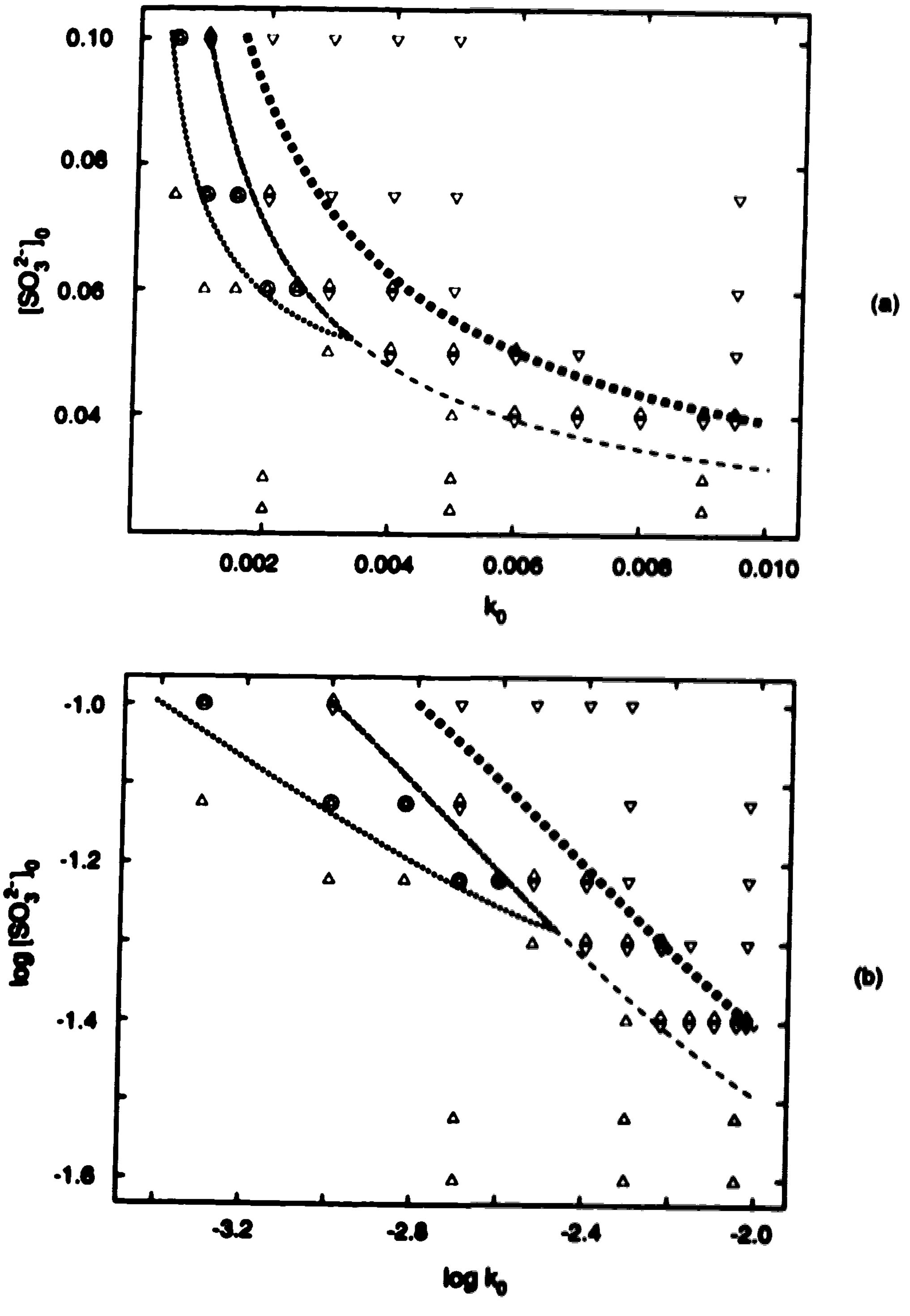

Fig. 48 The correct phase diagram for the BSF network at 20°C. (a) in the conventional parameter space; (b) in the log space. All parameters are the same as those in Fig. 46.

1 - current: 10 11 21 22 23 24 25 26
27 28

2 -currents: (9,16) (9,17) (9,18) (9,19) (9,20) (10,16) (12,17) (12,18)
(12,19) (12,20) (13,14) (13,15) (13,16) (13,17) (13,18) (13,19)
(13,20) (14,16) (14,17) (14,18) (14,19) (14,20) (15,16) (15,17)
(15,18) (15,19) (15,20)

6.7.2 The minimum set of necessary extreme currents for bifurcations

In the search of important chemical pathways responsible for the steady state bifurcations, we need to know the relative rates of the extreme currents near the bifurcation point. Usually at a bifurcation, the rate of one current increases above the rate of another current.

To find the minimum set of necessary extreme currents for a bifurcation, we calculate the j values at the bifurcation point only and put the j values in a descending order. Using the SNA package, we delete the currents one by one starting from the lower end of the j-ordering. After deleting a current, we flip over to the screen where unstable regions on steady state manifold are calculated. If the bifurcation feature is still unchanged, we go back and delete one more current. The procedure is repeated until we discover a current that cannot be deleted without destroying the bifurcation feature. We then carry out the same procedure starting from the top of the j-ordering until we meet another undeletable current. Sometimes, certain very strong currents are detail-balanced currents or CSTR flow-through currents. They maintain some concentration levels without influencing the stability. In a qualitative identification of necessary currents for a bifurcation, these currents can often be deleted. If a quantitative match is necessary, then we have to keep these currents. They will make our minimum set bigger. After finding the two ends of the necessary currents in the j-ordering, we then try to delete the remaining currents one by one to make sure all the remaining currents are necessary. We only keep the minimum number of necessary currents.

Using this procedure, we can also investigate more then one bifurcation point at a time. For example, when we are working on one SN (or SN$^+$) point of a fold, we can keep an eye on the other SN (or SN$^+$). If we want to find the minimum set for keeping both SN (or SN$^+$) bifurcation points, we should delete only those currents whose elimination does not eliminate either one of the two SN (SN$^+$) points. The minimum set of extreme currents found this way will be the minimum set responsible for the whole fold.

I applied the procedure to the fold of the BSF network. I started with the lower-left SN point. There are fourteen nonzero **j** values because the current cone is fourteen dimensional. The nonzero j values at the point are

$j_3 = 59.63$

$j_7 = 1.8684 \times 10^{-4}$

$j_6 = 7.1365 \times 10^{-5}$

$j_8 = 7.0960 \times 10^{-5}$

$j_{11} = 3.8032 \times 10^{-5}$

$j_4 = 8.4378 \times 10^{-6}$

$j_{10} = 6.7723 \times 10^{-6}$

$j_{16} = 3.8664 \times 10^{-7}$

$j_2 = 2.8544 \times 10^{-8}$

$j_9 = 1.5321 \times 10^{-8}$

$j_1 = 1.8742 \times 10^{-9}$

$j_{27} = 1.8182 \times 10^{-9}$

$j_5 = 1.8014 \times 10^{-9}$

$j_{26} = 9.2623 \times 10^{-12}$

Starting from the smallest j_{26}, I deleted all the right column currents and three of the left column currents in the order of $j_{26}, j_5, j_{27}, j_1, j_9, j_2, j_{16}, j_3, j_8, j_6$. The remaining four currents, j_7, j_{11}, j_4, j_{10}, preserved both saddle-node bifurcation points and the whole fold. Fig. 49 is a calculated steady state manifold after ten of the fourteen extreme currents have been deleted. Comparing with the minimum set of unstable combinations of extreme currents, we know the sources of instability are the unstable extreme currents $\mathbf{E}_{10}$ and $\mathbf{E}_{11}$. They have rates j_{10} and j_{11} respectively.

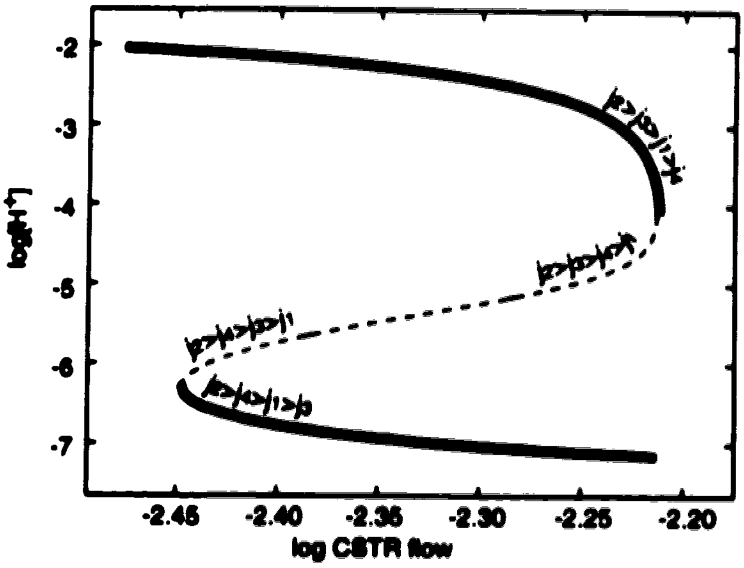

Fig. 49 A steady state manifold after ten of the fourteen extreme currents have been deleted for the BSF network. The remaining four extreme currents still preserve the whole fold. The relative rates of the four extreme currents in different regions are given by the j-orderings on the graph. Correspondence between the numbering of the j_i for the simplified network and that for the original network will be given in next section.

6.8 Stability boundaries of the BSFSN network

6.8.1 SN bifurcations in the simplified BSFSN network

The minimum set of necessary extreme currents $(\mathbf{E}_4, \mathbf{E}_7, \mathbf{E}_{10}, \mathbf{E}_{11})$ constitutes a simplified reaction network. I call it the BSFSN network, which means the network simplified from the BSF network with saddle-node features preserved.

Fig. 50 is the network diagram of the BSFSN network.

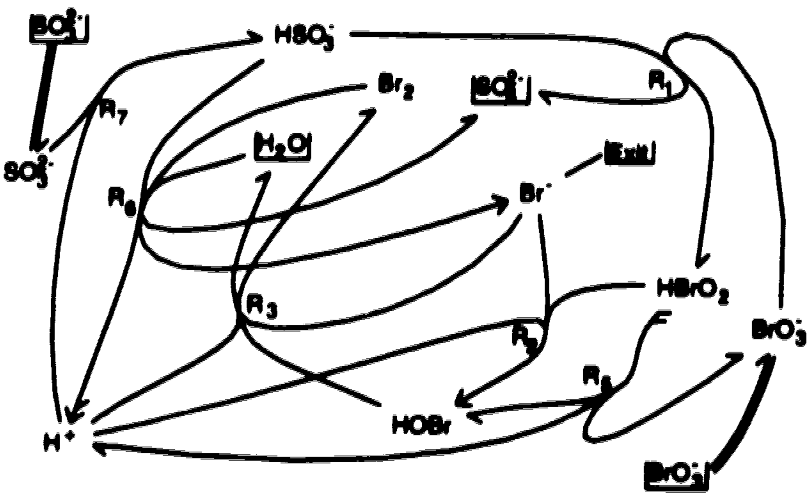

Fig. 50 Network diagram of the BSFSN network. It contains only four extreme currents that are necessary to maintain the fold and the SN bifurcations.

There are eleven reactions and eight intermediates in the BSFSN network as compared with twenty-three reactions and nine intermediates in the original BSF network. There are four extreme currents in the BSFSN network. They correspond to the original extreme currents of the BSF network in the following way:

BSFSN:	j_1	j_2	j_3	j_4
BSF:	j_4	j_7	j_{10}	j_{11}

Fig. 51 gives graphical representation of the four extreme currents of the BSFSN network. Reactions belonging to a specific extreme current are marked by thick lines on each of the four diagrams. SN bifurcations in the BSFSN network are the results of changing the relative rates of the four extreme currents on different branches of the fold. j-orderings shown in Fig. 49 are the relative rates of the extreme currents near the two bifurcation points. The upper-right SN bifurcation is caused by the changing relative rates of stable current 1 and unstable current

4. As we can imagine intuitively, the stable current 1 is faster on the stable upper branch while the unstable current 4 is faster on the middle branch. The lower-left SN bifurcation is the result of the changing relative rates of stable current 1 and unstable current 3. The stable current 1 is faster on the lower stable branch and the unstable current 3 is faster on the middle unstable branch.

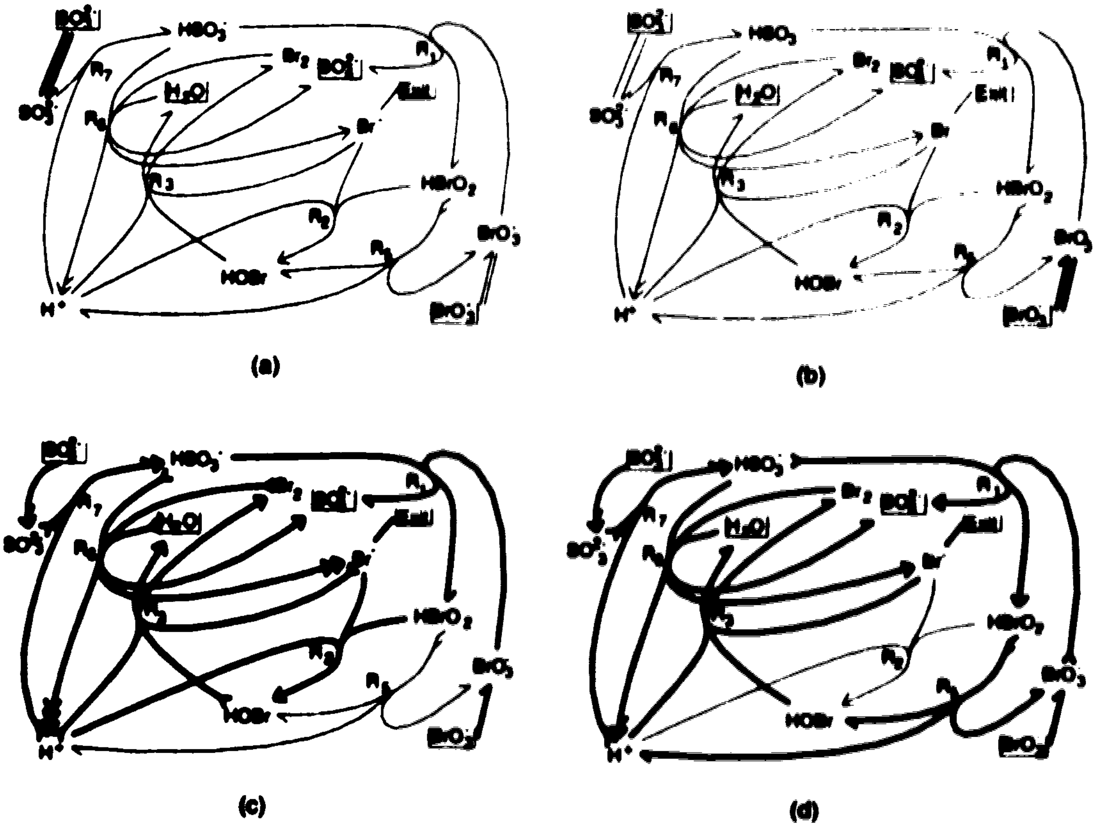

(a) (b)

(c) (d)

Fig. 51 Four extreme currents of the BSFSN network. (a) current $\mathbf{E}_1$ (current $\mathbf{E}_4$ in the BSF network); (b) current $\mathbf{E}_2$ (current $\mathbf{E}_7$ in the BSF network); (c) current $\mathbf{E}_3$ (current $\mathbf{E}_{10}$ in the BSF network); (d) current $\mathbf{E}_4$ (current $\mathbf{E}_{11}$ in the BSF network).

Another difference between the two SN bifurcations is that current 3 is the second fastest current at the upper-right SN point while current 4 is the second fastest current at the lower-left SN point. The two currents represent two different chemical pathways for the same total reaction:

$$3SO_3^{2-} + BrO_3^- \longrightarrow 3SO_4^{2-} + Br^-.$$

At high CSTR flow rates, a large portion of Br^- is washed out of the system. This effect benefits its competing species H^+ . From Fig. 51(c), we can see that H^+ competes with Br^- via both reactions R_2 and R_3. So, the upper-right SN bifurcation occurs at a higher flow rate and a higher $[H^+]$ concentration. When the flow rate is low, its effect on concentrations is opposite to the above. According to Fig. 51(d), a lower flow rate washes less Br^- out of the system. This causes the concentration of its competing species H^+ be suppressed via reaction R_3. Hence, both the flow rate and the $[H^+]$ are lower at the lower-left SN bifurcation point.

6.8.2 Linear segments of SN boundaries of the BSFSN network

Fig. 52 is a calculated phase diagram of the BSFSN network on the two-dimensional $(\log [SO_3^{2-}]_0, \log k_0)$ plane. The experimentally interesting region is shown in the small rectangle. It includes part of the stability boundaries that are close to straight lines with slopes of -1. It is complicated to derive explicit equations for these stability boundaries. I will discuss the process in the next section. Now, I focus on deriving implicit equations for the stability boundary segments marked as SN_1 and SN_2 on the graph to prove its linearity.

The BSFSN network contains eleven reactions shown in Scheme V.

Scheme V:

R_1 $\quad BrO_3^- + HSO_3^- \xrightarrow{k_1} HBrO_2 + SO_4^{2-}$

R_2 $\quad HBrO_2 + Br^- + H^+ \xrightarrow{k_2} 2HOBr$

R_3 $\quad HOBr + Br^- + H^+ \xrightarrow{k_3} Br_2 + H_2O$

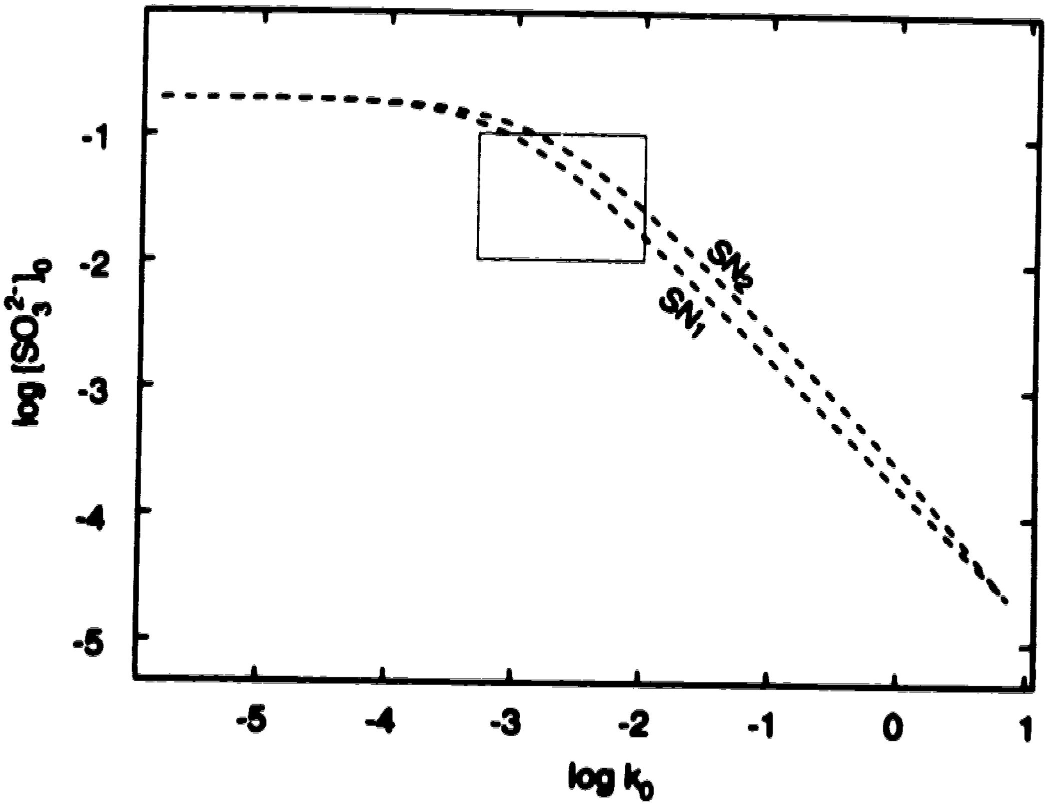

Fig. 52 Stability Boundaries of the BSFSN network. The region covered by the small rectangle is the experimentally interesting region.

R_5 $\quad 2HBrO_2 \xrightarrow{k_5} BrO_3^- + HOBr + H^+$

R_6 $\quad Br_2 + HSO_3^- + H_2O \xrightarrow{k_6} 2Br^- + SO_4^{2-} + 3H^+$

R_7 $\quad H^+ + SO_3^{2-} \xrightarrow{k_7} HSO_3^-$

I_2 $\quad \{SO_3^{2-}\} \xrightarrow{k_0} SO_3^{2-}$

I_5 $\quad \{BrO_3^-\} \xrightarrow{k_0} BrO_3^-$

O_1 $\quad Br^- \xrightarrow{k_0}$

O_2 $\quad SO_3^{2-} \xrightarrow{k_0}$

O_5 $\quad BrO_3^- \xrightarrow{k_0}$

The reaction numbers in Scheme V are the same as those in Scheme IV so that a direct comparison between the two networks can be made.

The extreme current matrix of the BSFSN network is

$$\mathbf{E} = \begin{array}{c} \\ R_1 \\ R_2 \\ R_3 \\ R_5 \\ R_6 \\ R_7 \\ I_2 \\ I_5 \\ O_1 \\ O_2 \\ O_5 \end{array} \begin{array}{c} \begin{array}{cccc} \mathbf{E}_1 & \mathbf{E}_2 & \mathbf{E}_3 & \mathbf{E}_4 \end{array} \\ \begin{pmatrix} 0 & 0 & 1 & 2 \\ 0 & 0 & 1 & 0 \\ 0 & 0 & 2 & 1 \\ 0 & 0 & 0 & 1 \\ 0 & 0 & 2 & 1 \\ 0 & 0 & 3 & 3 \\ 1 & 0 & 3 & 3 \\ 0 & 1 & 1 & 1 \\ 0 & 0 & 1 & 1 \\ 1 & 0 & 0 & 0 \\ 0 & 1 & 0 & 0 \end{pmatrix} \end{array}.$$

For this network, equation (8) can be written as

$$k_1[\mathrm{HSO_3^-}][\mathrm{BrO_3^-}] = j_3 + 2j_4 \tag{41.1}$$

$$k_2[\mathrm{H^+}][\mathrm{HBrO_2}][\mathrm{Br^-}] = j_3 \tag{41.2}$$

$$k_3[\mathrm{H^+}][\mathrm{HOBr}][\mathrm{Br^-}] = 2j_3 + j_4 \tag{41.3}$$

$$k_5[\mathrm{HBrO_2}]^2 = j_4 \tag{41.4}$$

$$k_6[\mathrm{HSO_3^-}][\mathrm{Br_2}] = 2j_3 + j_4 \tag{41.5}$$

$$k_7[\mathrm{H^+}][\mathrm{SO_3^{2-}}] = 3j_3 + 3j_4 \tag{41.6}$$

$$k_0[\mathrm{SO_3^{2-}}]_0 = j_1 + 3j_3 + 3j_4 \tag{41.7}$$

$$k_0[\mathrm{BrO_3^-}]_0 = j_2 + j_3 + j_4 \tag{41.8}$$

$$k_0[\mathrm{Br^-}] = j_3 + j_4 \tag{41.9}$$

$$k_0[\mathrm{SO_3^{2-}}] = j_1 \tag{41.10}$$

$$k_0[\mathrm{BrO_3^-}] = j_2. \tag{41.11}$$

According to Fig. 49, the linear segment of the lower stability boundary SN_1 shown in Fig. 52 also satisfies the equation:

$$j_1 = j_3. \tag{41.12}$$

On the linear segment of SN_1, concentrations of five chemicals are constant. Fig. 53 shows all eight concentrations on the stability boundaries. We can see that HSO_3^-, HOBr, $HBrO_2$, Br_2 and BrO_3^- have constant concentrations on the linear segment of the SN_1 boundary.

To prove the linearity for the linear segment of the SN_1 boundary, we need to derive an equation that contains only experimental parameters and the five constant chemical concentrations mentioned above.

From equations (41.6) and (41.9), we have

$$3k_0[Br^-] = k_7[H^+][SO_3^{2-}]. \tag{42}$$

Similarly, we have

$$k_2[H^+][HBrO_2][Br^-] = k_0[SO_3^{2-}] \tag{43}$$

according to equations (41.2), (41.10) and (41.12). We also have

$$k_3[H^+][HOBr][Br^-] = k_6[HSO_3^-][Br_2] \tag{44}$$

according to equations (41.3) and (41.5). Dividing (43) by (44) and rearranging the resulting equation gives

$$[SO_3^{2-}] = \frac{k_2k_6[HSO_3^-][Br_2][HBrO_2]}{k_0k_3[HOBr]}. \tag{45}$$

Dividing (42) by (43) and rearranging produce

$$[H^+] = \frac{\sqrt{3}k_0}{k_2^{\frac{1}{2}}k_7^{\frac{1}{2}}[HBrO_2]^{\frac{1}{2}}}. \tag{46}$$

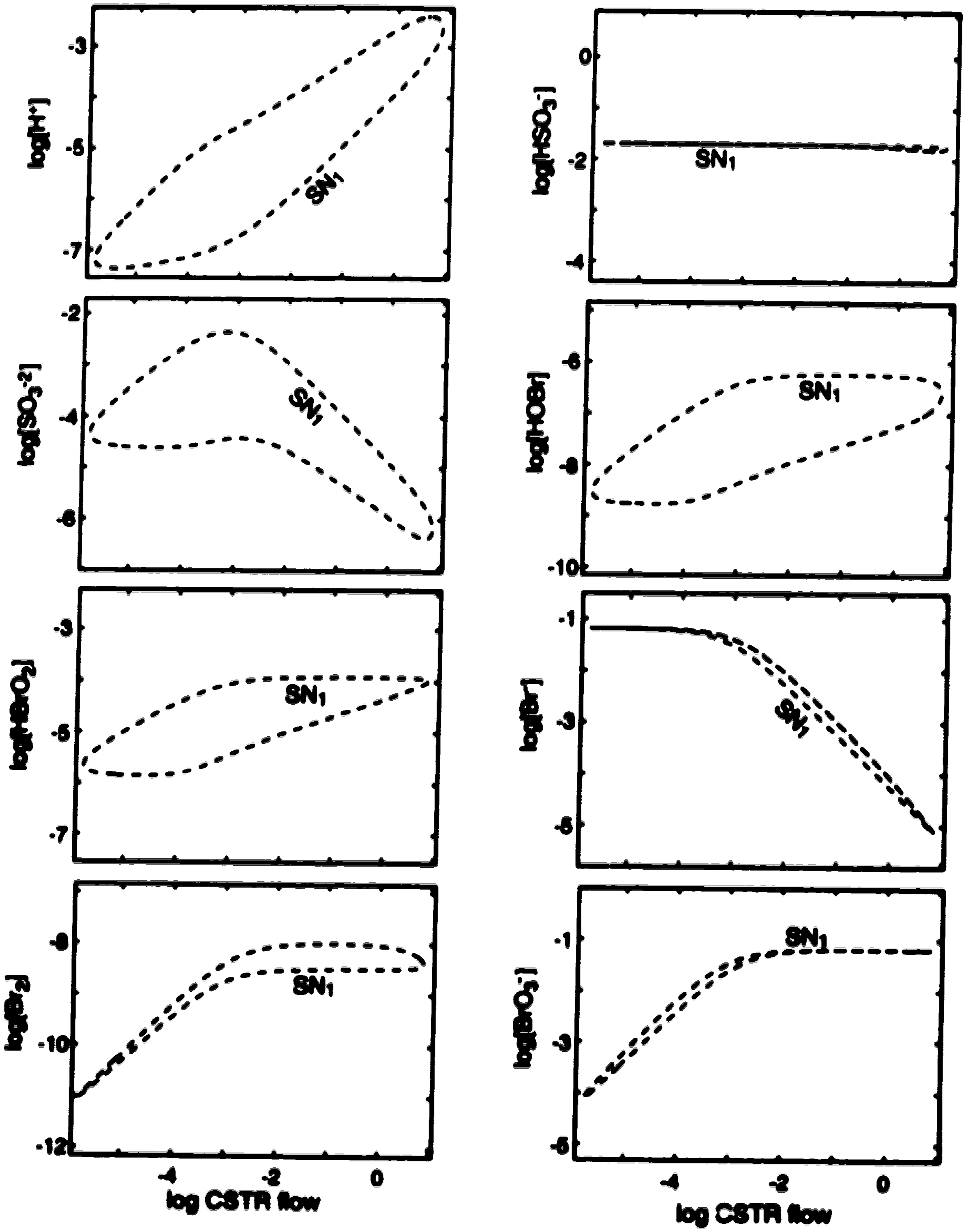

Fig. 53 Concentrations of dynamical intermediates on the stability boundaries of the BS-FSN network. Note that the linear segments marked by SN_1 on the plots $[HSO_3^-]$, $[HOBr]$, $[HBrO_2]$, $[Br_2]$, $[BrO_3^-]$ are constant on the linear segments.

Substituting equations (45), (46) into (42) gives an expression for $[Br^-]$

$$[Br^-] = \frac{k_2^{\frac{1}{2}} k_6 k_7^{\frac{1}{2}}}{\sqrt{3} k_0 k_3} \frac{[HSO_3^-][Br_2][HBrO_2]^{\frac{1}{2}}}{[HOBr]}. \tag{47}$$

Substituting equations (41.9), (41.10), (45) and (47) into (41.7) gives the stability boundary equation

$$k_0[SO_3^{2-}]_0 = \frac{k_2 k_6}{k_3} \frac{[HSO_3^-][Br_2][HBrO_2]}{[HOBr]} \{1 + \frac{\sqrt{3} k_7^{\frac{1}{2}}}{k_2^{\frac{1}{2}} [HBrO_2]^{\frac{1}{2}}}\}. \tag{48}$$

On the linear segment, all variables and parameters included on the right side of equation (48) are constant. Hence, the equation can be written as

$$k_0[SO_3^{2-}] = c,$$

where c is a constant whose value equals to the right-hand side of equation (48). In log space, the equation is

$$\log [SO_3^{2-}]_0 = -\log k_0 + C,$$

where $C = \log c$. This is a straight line with a slope of -1.

Using the similar treatment, we can derive an equation for the upper-right saddle-node bifurcation surface SN_2:

$$k_0[SO_3^{2-}]_0 = k_5[HBrO_2]^2 + (\frac{3k_5 k_6 k_7}{k_3})^{\frac{1}{2}} \frac{[HBrO_2][HSO_3^-]^{\frac{1}{2}}[Br_2]^{\frac{1}{2}}}{[HOBr]^{\frac{1}{2}}}. \tag{49}$$

In log space, this is also a straight line with a slope of -1.

6.8.3 Explicit stability boundary equations of the BSFSN network

It is difficult to derive analytical stability boundary equations of the BSFSN network because of two reasons. First, the steady state manifold of the BSFSN network is highly nonlinear. The hyperplane approximation cannot be used to derive either the steady state manifold equations or the stability boundary equations. The nonlinearity can be seen from Fig. 49. The second difficulty in deriving the stability boundary equations is that the rates of the important currents are comparable. The rates of the currents at a typical point on a stability boundary of the BSFSN network are

$$j_1 = 1.2992 \times 10^{-5}; \qquad j_2 = 3.5413 \times 10^{-3};$$

$$j_3 = 7.1249 \times 10^{-6}; \qquad j_4 = 4.6970 \times 10^{-5}.$$

Here, current 2 is the fastest current. The other three currents have comparable rates and cannot be ignored. Therefore, the dominant extreme current approximation cannot be used to derive explicit equations for the stability boundaries. The only method that we can use is to do a stability analysis in $(\mathbf{h},\mathbf{j})$ parameters and find the important stability boundary conditions in $(\mathbf{h},\mathbf{j})$ parameters. The boundary conditions will greatly simplify the system of equations and the equations will become directly solvable.

A stability analysis using $(\mathbf{h},\mathbf{j})$ parameters produced 186 systems of inequalities representing unstable regions for the BSFSN network. Two of them are related to the SN boundaries in which we are interested. One system contains the following inequalities.

$$\begin{aligned}
-\log j_1 + \log j_2 + \log j_3 - \log j_4 &> \log \frac{2}{3} \\
\log j_3 - \log j_4 - \log[\mathrm{HSO}_3^-] + \log[\mathrm{HOBr}] &> \log 2 \\
\log j_3 - \log j_4 - \log[\mathrm{HSO}_3^-] + \log[\mathrm{H}^+] &> \log 2 \\
-\log j_1 + \log j_3 &> \log \frac{2}{3} \\
-\log[\mathrm{HSO}_3^-] + \log[\mathrm{Br}_2] &> \log 6 \\
-\log[\mathrm{HSO}_3^-] + \log[\mathrm{HBrO}_2] &> \log 1 \\
\log j_3 + \log j_4 &> \log 6.
\end{aligned}$$

The unstable steady states in the SN region must satisfy all of the 7 inequalities.

Non-log form of the system of inequalities is

$$\begin{aligned}
j_2 j_3 &> \frac{2}{3} j_1 j_4 \\
j_3[\mathrm{HOBr}] &> 2 j_4[\mathrm{HSO}_3^-] \\
j_3[\mathrm{H}^+] &> 2 j_4[\mathrm{HSO}_3^-] \\
j_3 &> \frac{2}{3} j_1 \\
[\mathrm{Br}_2] &> 6[\mathrm{HSO}_3^-] \\
[\mathrm{HBrO}_2] &> [\mathrm{HSO}_3^-] \\
j_4 &> 6 j_3.
\end{aligned}$$

The system of inequalities for the unstable region contains the inequality

$$j_3 > \frac{2}{3} j_1.$$

This inequality is violated when $j_3 = \frac{2}{3} j_1$, which is one of the boundaries of the unstable region. Previously, the method of examining essential currents found the equation $j_3 = j_1$ for the boundary. Thus, the analytical treatment using SNA agrees with the numerical observation that essential currents $\mathbf{E}_1$ and $\mathbf{E}_3$ have roughly equal rates at the bifurcation. The factor of $\frac{2}{3}$ in the SNA result is not significant because the method omits terms from polynomials. Such an approximation can produce coefficients which are inaccurate by a factor close to 1.

The unstable region in the $\log \mathbf{h}$–$\log \mathbf{j}$ parameters is a convex polyhedral cone. The boundary of each inequality above is one face of the cone. Two boundaries meet at a codimension 2 face of the cone. We now consider the special case of the codimension 2 face where the condition

$$j_4 = 6j_3$$

is satisfied in addition to the condition $j_3 = \frac{2}{3}j_1$, which holds along the SN$_1$ curve. This extra condition makes it possible to solve the equations explicitly.

Substituting the two boundary equations into equations (41.1) through (41.11) gives

$$k_1[HSO_3^-][BrO_3^-] = \frac{16}{3}j_1 \tag{50.1}$$

$$k_2[H^+][HBrO_2][Br^-] = \frac{2}{3}j_1 \tag{50.2}$$

$$k_3[H^+][HOBr][Br^-] = \frac{16}{3}j_1 \tag{50.3}$$

$$k_5[HBrO_2]^2 = 4j_1 \tag{50.4}$$

$$k_6[HSO_3^-][Br_2] = \frac{16}{3}j_1 \tag{50.5}$$

$$k_7[H^+][SO_3^{2-}] = 14j_1 \tag{50.6}$$

$$k_0[SO_3^{2-}]_0 = 15j_1 \tag{50.7}$$

$$k_0[BrO_3^-]_0 = j_2 + \frac{14}{3}j_1 \tag{50.8}$$

$$k_0[Br^-] = \frac{14}{3}j_1 \tag{50.9}$$

$$k_0[SO_3^{2-}] = j_1 \tag{50.10}$$

$$k_0[\mathrm{BrO_3^-}] = j_2. \tag{50.11}$$

Equations (50.1) through (50.11) can be solved to give concentrations of eight species and the stability boundary equation. Procedures for solving the equations mainly include substitutions of one equation into another and rearranging the resulting equations.

Substituting (50.10) into (50.7) gives

$$[\mathrm{SO_3^{2-}}] = \frac{1}{15}[\mathrm{SO_3^{2-}}]_0; \tag{51.1}$$

Substituting (50.9) into (50.7) gives

$$[\mathrm{Br^-}] = \frac{14}{45}[\mathrm{SO_3^{2-}}]_0; \tag{51.2}$$

Substituting (50.11), (50.7) into (50.8) gives

$$[\mathrm{BrO_3^-}] = [\mathrm{BrO_3^-}]_0 - \frac{14}{45}[\mathrm{SO_3^{2-}}]_0; \tag{51.3}$$

Substituting (50.4) into (50.7) gives

$$[\mathrm{HBrO_2}] = \{\frac{4k_0}{15k_5}[\mathrm{SO_3^{2-}}]_0\}^{\frac{1}{2}}; \tag{51.4}$$

Substituting (50.6), (51.1) into (50.7) gives

$$[\mathrm{H^+}] = \frac{14k_0}{k_7}; \tag{51.5}$$

Substituting (50.3), (51.2) and (51.5) into (50.7) gives

$$[\mathrm{HOBr}] = \frac{8k_7}{98k_3}; \tag{51.6}$$

Substituting (50.1), (51.3) into (50.7) gives

$$[\mathrm{HSO_3^-}] = \frac{14k_0[\mathrm{SO_3^{2-}}]_0}{k_1\{45[\mathrm{BrO_3^-}]_0 - 14[\mathrm{SO_3^{2-}}]_0\}}; \tag{51.7}$$

Substituting (50.5), (51.7) into (50.7) gives

$$[\mathrm{Br_2}] = \frac{8k_1}{585k_6}\{45[\mathrm{BrO_3^-}]_0 - 14[\mathrm{SO_3^{2-}}]_0\}. \tag{51.8}$$

The stability boundary equation is obtained by substituting (50.7), (51.2), (51.4) and (51.5) into (50.2) and rearranging the equation. The result is

$$k_0[\mathrm{SO_3^{2-}}]_0 = \frac{15k_5k_7^2}{38416k_2^2}. \tag{52}$$

Note that the equation does not necessarily hold at the SN_1 curve. It holds only if the parameters satisfy the extra condition $j_4 = 6j_3$, which means the steady state is on a codimension 2 face of the cone of instability.

On the $(\log[\mathrm{SO_3^{2-}}]_0, \log k_0)$ plane, the right-hand side of equation (52) is constant, so the equation can be written as

$$k_0[\mathrm{SO_3^{2-}}]_0 = c.$$

In log form, the equation is

$$\log[\mathrm{SO_3^{2-}}]_0 = -\log k_0 + C.$$

This is a straight line with a slope of -1, which matches Fig. 52. Substituting this equation into equations (51.1) to (51.8) and converting the resulting equations into the log version gives a set of equations which matches the eight plots in Fig. 53. The derivation is very straight forward and is omitted here. (For the concentrations $[\mathrm{BrO_3^-}]$, $[\mathrm{HSO_3^-}]$ and $[\mathrm{Br_2}]$, approximate straight line equations can be obtained by considering that current 2 is the fastest current in the parameter range.)

Using the same procedures as above, we can derive an explicit equation for the SN_2 boundary (upper-right SN bifurcation surface). To get the equation, we need to combine boundary equations

$$j_3 = 3j_4$$

$$j_1 = 6j_4.$$

with equations (41.1) through (41.11). All other steps are the same as those used for deriving SN_1 boundary equation. The result is

$$k_0[SO_3^{2-}]_0 = \frac{117k_5k_7^2}{64k_2^2}.$$

Like Equation 52, this equation holds when the SN_2 bifurcation is on a codimension 2 face of the cone of instability.

6.9 Destabilizing feedback cycles of the BSFSN network

The feedback cycles which produce the instability can be determined easily using the SNA software. Eiswirth, Freund and Ross[30-31] have summarized some prototype unstable cycles for chemical oscillators using SNA. For the BSFSN network, there are no Hopf bifurcations and oscillations. We will only identify the destabilizing cycles responsible for the saddle-node instability.

Fig. 54 shows the five destabilizing cycles of the BSFSN network. To show the location of the cycles in the whole network, I have also included the network diagram in the figure.

The four destabilizing feedback cycles in figures 54(b), 54(c), 54(e) and 54(f) have similar network features. They all contain a critical current cycle and a destabilizing positive feedback 2-cycle. In Fig. 54(b), the critical current cycle contains H^+ and Br_2 via reactions R_3 and R_6. H^+ also lies on a positive feedback cycle

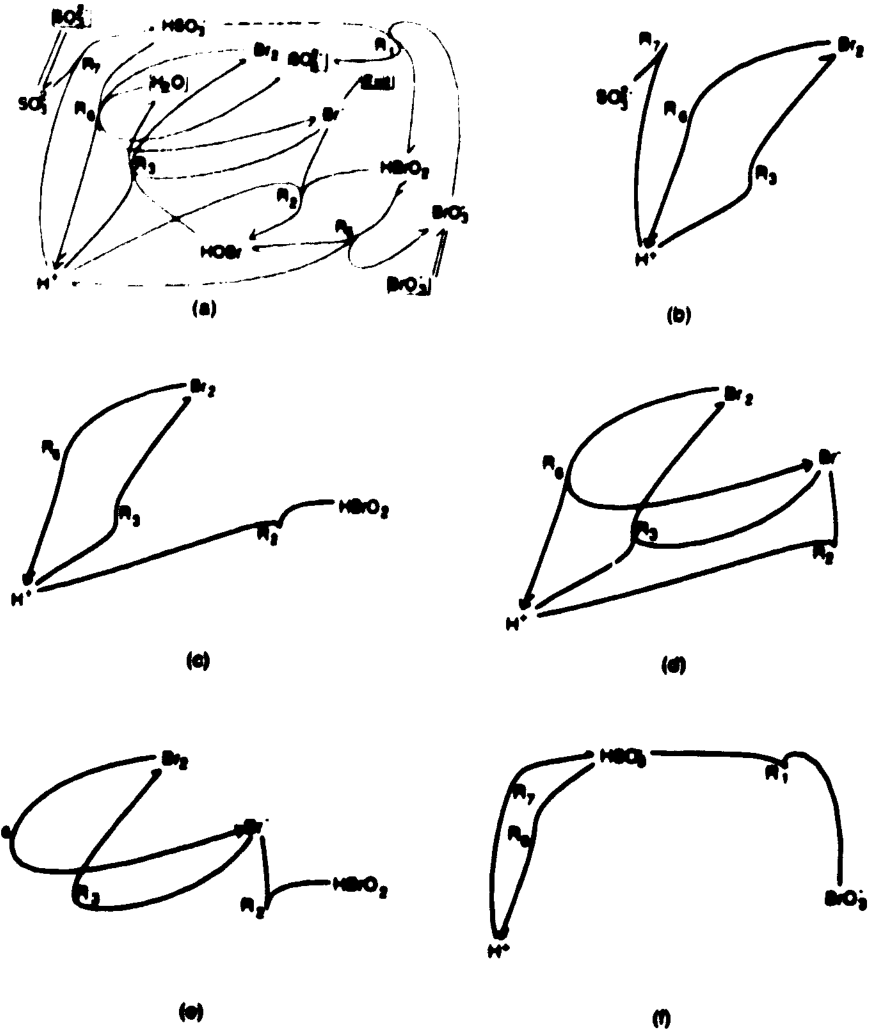

Fig. 54 Destabilizing feedback cycles of the BSFSN network, shown along with the original network diagram. Positions of species and reactions in the current cycles were not changed so their relationships with the original network diagram can be seen directly.

involving SO_3^{2-} via reaction R_7, which destabilizes. That such an arrangement of feedback cycles destabilizes was proven by Clarke in theorem V.10 in Ref. 28. Fig. 54(c) contains the same critical current cycle as Fig. 54(b), but the destabilizing positive cycle involves $HBrO_2$ via R_2. A similar analysis can be applied to critical current cycles and positive feedback cycles in Fig. 54(e) and Fig 54(f), where different species and reactions are involved.

Fig. 54(d) contains a short-circuited cycle which involves reactions R_3, R_6 and species Br_2, H^+, Br^-. A positive feedback 2-cycle between H^+ and Br^- via R_2 still destabilizing here. This is also a source of instability.

VII. Summary and conclusion

In this thesis, I have systematically presented my research on computer investigation of stability boundaries. It includes theoretical investigation, method development and real chemical reaction network analysis.

Following the introductory chapter, I discussed topics related to steady state manifolds of chemical reaction networks in chapter II. I first summarized terminology, ideas and parameters used by the SNA. Then, the problem of calculating steady state manifolds was tackled using numerical and analytical approaches. My numerical algorithm calculates reaction network steady state manifold. accurately and efficiently. Two analytical methods provide approximate analytical formulas for steady state manifolds in a multidimensional parameter space. They tell how experimental parameters affect the steady state manifolds. They also help identify important chemical pathways at the steady states.

The investigation of stability boundaries begins in chapter III. First, I discussed steady state stability problems and explained the mathematical methods used for determining stability. Then, I discussed the general equations for the stability boundary and a numerical method for calculating them. The general stability boundary equations cause the stability boundary to have an interesting structure. The structure is useful for exploring unstable regions.

In chapter IV, I turned my attention to another important problem associated with stability boundaries. How do the experimental parameters affect stability boundaries? Multidimensional analytical equations for stability boundaries were derived using three approaches. Since all experimental parameters are presented as variables in the equations, their implications on stability boundaries can be seen explicitly. For some networks, analytical equations may not always be available. In these situations, an operational method based on slope sign patterns can be used to determine how experimental parameters affect stability boundaries. The methods presented in chapter IV can be used as a guidance for adjusting experimental parameters or predict experimental results.

In chapter V, I discussed stability boundaries of the Gray-Scott network. A complete stability analysis was conducted in the (**h**, **j**) parameter space. It identified all sources of instabilities. A mushroom-shaped steady state manifold was obtained. The important chemical pathways were found for various regions of the steady state manifold. Stability boundaries on three different two-dimensional parameter planes were calculated numerically. The various stability boundary structures explains why this prototype reaction network has such rich chemical dynamics

In chapter VI, I analyzed stability boundaries of the bromate-sulfite-ferrocyanide (BSF) reaction network. The focus here is the stability boundary structure and its relationship to the experimentally observed nonlinear dynamics. I explained the process in searching for the observed oscillations. The fact that the expected cross-shaped phase diagrams were not found prompted in-depth investigation on reasons for this. My results require a reinterpretation of the experimental results. I also developed an approach to avoid misinterpreting the experimental stability boundaries and dynamical features in the various stability regions. I devised a method which uses the sign patterns of the slopes to improve the rate constants and make them match the experimental results.

After solving the stability boundary structure problem, I analyzed the BSF network to find sources of instability that are responsible for the stability boundaries. I simplified the network and discussed how the key chemical pathways affect stability properties of the steady states. This picture helps on understanding the whole reaction network.

The research conducted in this thesis uses the approach known as SNA. This work has greatly enhanced SNA's ability to deal with real chemical reaction networks using both the conventional $(\mathbf{k}, \mathbf{C})$ parameters and the $(\mathbf{h}, \mathbf{j})$ parameters. It has also enriched our understanding of stability boundary structures. The numerical and analytical methods for calculating steady state manifold as well as stability boundaries provide us with an effective means for investigating chemical reaction networks. The SE curves discovered in this thesis are important. They connect DZ-centered structures so that new unstable regions in parameter spaces can be explored. The discovery that non-cross-shaped stability boundaries occur may help explain other experimental results. The strategy proposed in the thesis can be applied to many mechanisms.

The SNA program package makes it possible to treat other mechanisms easily. A particular interesting research project is to reexamine reaction networks which have been claimed to have cross-shaped phase diagrams. I have shown that what appears to be cross-shaped is not always truly cross-shaped. Olsen and Epstein have recently emphasized the importance of investigating stability boundaries using bifurcation analysis methods[26,70]. Their approach is based on the universal unfolding and the singularity theory. Using the stability boundary structures, SE curves and other methods presented in this thesis, we can extend our understanding to even wider scope, such as the relationships between Hopf bifurcations on two different branches of a fold. Using the algorithms developed for this thesis, we can also trace stability boundaries efficiently. The unique feature of SNA in identifying important chemical pathways improves our understanding of real chemical systems.

Bibliography

1. J. J. Tyson, *"Some Further Studies of Nonlinear Oscillations in Chemical Systems"*, J. Chem. Phys. **58**, 3919 (1973).
2. U. F. Franck, *"Feedback Kinetics in Physicochemical Oscillators"*, Ber. Bunsenges. Phys. Chem. **84**, 334 (1980).
3. E. D. Cera, P. E. Phillipson and J. Wyman, *"Limit-cycle Oscillations and Chaos in Reaction Networks Subject to Conservation of Mass"*, Proc. Natl. Acad. Sci. USA **86**, 142 (1989).
4. B. Hess and A. Boiteux, *"Oscillatory Phenomena in Biochemistry"*, Annu. Rev. Biochem. **40**, 237 (1971).
5. H. Degn, *"Oscillating Chemical Reactions in Homogeneous Phase"*, J. Chem. Educ. **49**, 302 (1972).
6. Faraday Symp. Chem. Soc., *"Physical Chemistry of Oscillatory Phenomena"*, (University Press, Aberdeen, 1974).
7. O. Decroly and A. Goldbeter, *"Birhythmicity, Chaos, and Other Patterns of Temporal Self-Organization in a Multiply Regulated Biochemical System"*, Proc. Natl. Acad. Sci. USA **79**, 6917 (1982).
8. O. Decroly and A. Goldbeter, *"Coexistence Between Three Stable Periodic Regimes in a Multiply Regulated Biochemical System"*, C. R. Acad. Sci. Paris SER II **298**, 779 (1984).
9. A. J. Lotka, *"Contribution to the Theory of Periodic Reactions"*, J. Phys. Chem. **14**, 271 (1910).
10. A. J. Lotka, *"Undamped Oscillations Derived from the Law of Mass Action"*, J. Am. Chem. Soc. **42**, 1595 (1920).
11. W. C. Bray, *"A Periodic Reaction in Homogeneous Solution and Its Reaction to Catalysis"*, J. Am. Chem. Soc. **43**, 1262 (1921).

12. B. P. Belousov, Ref. Radiats. Med., 1958, Medgiz, Moscow , 145 (1959).

13. A. M. Zhabotinskii, Dokl. Akad. Nauk SSSR **157**, 392 (1964).

14. R. J. Field, E. Körös and R . M. Noyes, *"Oscillations in Chemical Systems. II. Thorough Analysis of Temporal Oscillation in the Bromate-Cerium-Malonic Acid System"*, J. Am. Chem. Soc. **94**, 8649 (1972).

15. P. Gray and S. K. Scott, *"Autocatalytic Reactions in the Isothermal, Continuous Stirred Tank Reactor"*. Chem. Eng. Sci. **38**, 29 (1983).

16. P. Gray and S. K. Scott, *"Autocatalytic Reactions in the Isothermal, Continuous Stirred Tank Reactor"*, Chem. Eng. Sci. **39**, 1087 (1984).

17. S. R. Kay, S. K. Scott and P. -G. Lignola, *"The Application of Singularity Theory to Isothermal Autocatalytic Reactions: the Influence of Uncatalyzed Reactions"*, Proc. Roy. Soc. London A **409**, 433 (1987).

18. P. Gray and S. K. Scott, *"Archetypal Response Patterns for Open Chemical Systems with Two Components"*, Phil. Trans. Roy. Soc. London A **332**, 69 (1990).

19. P. Gray and S. K. Scott, *"Isothermal Oscillations and Exotic Bifurcation Behaviour from Second-Order Schemes Involving Only Three Components"*, React. Kinet. Catal. Lett. **42**, 227 (1990).

20. P. Gray and S. R. Kay, *"Modelling Complex Oscillatory Behavior by Simple Chemical Schemes"*, J. Phys. Chem. **94**, 3304 (1990).

21. J. E. Pearson, *"Complex Patterns in a Simple System"*, Science **261**, 189 (1993).

22. J. Boissonade and P. De Kepper, *"Transition from Bistability to Limit Cycle Oscillations. Theoretical Analysis and Experimental Evidence in An Open Chemical System"*, J. Phys. Chem. **84**, 501 (1980).

23. J. Guckenheimer, *"Multiple Bifurcation Problems for Chemical Reactors"*, Physica **20D**, 1 (1986).

24. I. R. Epstein and K. Kustin, "*A Mechanism for Dynamical Behavior in the Oscillatory Chlorite-Iodide Reaction*", J. Phys. Chem. **89**, 2275 (1985).

25. E. C. Edblom, Y. Luo, M. Orban, K. Kustin, and I. R. Epstein, "*Kinetics and Mechanism of the Oscillatory Bromate-Sulfite-Ferrocyanide Reaction*", J. Phys. Chem. **93**, 2722 (1989).

26. R. J. Olson and I. R. Epstein, "*Bifurcation Analysis of Chemical Reaction Mechanisms. I. Steady State Bifurcation Structure*", J. Chem. Phys. **94**, 3083 (1991).

27. J. Ringland, "*Rapid Reconnaissance of a Model of a Chemical Oscillator by Numerical Continuation of a Bifurcation Feature of Codimension 2*", J. Chem. Phys. **95**, 555 (1991).

28. B. L. Clarke, "*Stability of Complex Reaction Networks*", Adv. Chem. Phys. **43**, 1 (1980).

29. B. L. Clarke, "*Stoichiometric Network Analysis*", Cell Biophysics **12**, 237 (1988).

30. M. Eiswirth, A. Freund and J. Ross, "*Operational Procedure toward the Classification of Chemical Oscillators*", J. Phys. Chem. **95**, 1294 (1991).

31. M. Eiswirth, A. Freund and J. Ross, "*Mechanistic Classification of Chemical Oscillators and the Role of Species*", Adv. Chem. Phys. **80**, 127 (1991).

32. F. Hynne, P. G. Sørensen and T. Møller, "*Current and Eigenvector Analysis of Chemical Reaction Networks at Hopf Bifurcations*", J. Chem. Phys. **98**, 211 (1993).

33. F. Hynne, P. G. Sørensen and T. Møller, "*Complete Optimization of Models of the Belousov-Zhabotinsky Reaction at a Hopf Point*", J. Chem. Phys. **98**, 219 (1993).

34. B. D. Aguda and R. Larter, "*Dynamic Elements of Mixed-mode Oscillations and Chaos in Peroxidase-oxidase Model Network*", J. Chem. Phys. **90**, 4168 (1989).

35. B. D. Aguda and B. L. Clarke, "*Bistability in Chemical Reaction Networks: Theory and Application to the Peroxidase-oxidase Reaction*", J. Chem. Phys. **87**, 3461 (1987).

36. E. J. Doedel and J. P. Kernevez, "*AUTO: Software for Continuation and Bifurcation Problems in Ordinary Differential Equations; AUTO 86 User Manual, Technical Report*", (Applied Mathematics, California Institute of Technology, 1980).

37. B. L. Clarke, "*Stoichiometric Network Analysis of the Oxalate-Persulfate-Silver Oscillator*", J. Chem. Phys. **97**, 2459 (1992).

38. K. Showalter, R. M. Noyes and K. Bar-Eli, "*A Modified Oregonator Model Exhibiting Complicated Limit Cycle Behavior in a Flow System*", J. Phys. Chem. **69**, 2514 (1978).

39. B. L. Clarke, "*Stability of the Bromate-Cerium-Malonic Acid Network. I. Theoretical Formulation*", J. Chem. Phys. **64**, 4165 (1976).

40. G. Hadley, "*Linear Programming*", (Addison-Wesley Pub. Co., Inc., Reading, Mass., U.S.A., 1962).

41. B. L. Clarke, "*Qualitative Dynamics and Stability of Chemical Reaction Networks*", Studies in Physical and Theoretical Chemistry **28**, 322 (1983).

42. B. L. Clarke, "*Complete Set of Steady States for the General Stoichiometric Dynamical System*", J. Chem. Phys. **75**, 4970 (1981).

43. B. L. Clarke and W. Jiang, "*Method for Deriving Hopf and Saddle-node Bifurcation Hypersurfaces and Application to a Model of the Belousov-Zhabitinskii System*", J. Chem. Phys. **99**, 4464 (1993).

44. M. Kubiček, *"Dependence of Solution of Nonlinear Systems on a Parameter"*, ACM Trans. Math. Software **2**, 98 (1976).

45. W. H. Press, B. P. Flannery, S. A. Teukolsky, W. T. Veyyerling, *"Numerical Recipes"*, (Cambridge Univ. Press, Cambridge, 1986).

46. B. von Hohenbalken, B. L. Clarke and J. E. Lewis, *"Least Distance Methods for the Frame of Homogeneous Equation Systems"*, J. Comp. Appl. Math **19**, 231 (1976).

47. B. Porter, *"Stability Criteria for Linear Dynamical Systems"*, (Academic Press, New York, 1968).

48. F. R. Gantmacher, *"Applications of the Theory of Matrices"*, (Interscience Publishers, New York, 1959).

49. B. L. Clarke, *"Stability of the Bromate-Cerium-Malonic Acid Network. I. Steady State Formic Acid Case"*, J. Chem. Phys. **64**, 4179 (1976).

50. S. R. Rüdiger, *"From Equilibrium to Chaos: Practical Bifurcation and Stability Analysis"*, (Elsevier, New York, 1988).

51. B. J. Beltrami, *"Mathematics for Dynamic Modeling"*, (Academic Press, Boston, 1987).

52. J. Guckenheimer, *"Nonlinear Oscillations, Dynamical Systems, and Bifurcations of Vector Fields"*, (Springer-Verlag, New York, 1983).

53. L. Orlando, *"Sul problema di Hurwitz relativo alle parti reali delle radici di un' equazione algebrica"*, Math. Ann. **71**, 233 (1911).

54. H. W. Broer and F. Takens, *"Geometry and Analysis in Nonlinear Dynamics"*, (Longman Scientific&Technical, Essex, 1992).

55. F. Dumortier, R. Roussarie and J. Sotomayor, *"Generic 3-Parameter Families of Vector Fields on the Plane, Unfolding a Singularity with Nilpotent Linear Part. The Cusp Case of Codimension 3"*, Ergod. Th.&Dynam. Sys. **7**, 375 (1987).

56. K. D. Willamowski and O. E. Rössler, "*Irregular Oscillations in a Realistic Abstract Quadratic Mass Action System*", Z. Naturforsch **35A**, 317 (1980).

57. B. D. Aguda and B. L. Clarke, "*Dynamic Elements of Chaos in the Willamowski-Rössler Network*", J. Chem. Phys. **89**, 7428 (1988).

58. E. C. Edblom, M. Orbán and I. R. Epstein, "*A New Iodate Oscillator: The Landolt Reaction with Ferrocyanide in a CSTR*", J. Am. Chem. Soc. **108**, 2826 (1986).

59. E. C. Edblom, L. Györgyi, M. Orbán and I. R. Epstein, "*A Mechanism for Dynamical Behavior in the Landolt Reaction with Ferrocyanide*", J. Am. Chem. Soc. **109**, 4876 (1987).

60. V. Gáspár and K. Showalter, "*The Oscillatory Landolt Reaction. Empirical Rate Law Model and Detailed Mechanism*", J. Am. Chem. Soc. **109**, 4869 (1987).

61. R. M. Noyes, "*A Generalised Mechanism for Bromate-Driven Oscillators Controlled by Bromide*", J. Am. Chem. Soc. **102**, 4644 (1980).

62. P. De Kepper, I. R. Epstein and K. J. Kustin, "*Bistability in the Oxidation of Arsenite by Iodate in a Stirred Flow Reactor*", J. Am. Chem. Soc. **103**, 6121 (1981).

63. P. Valko, and S. Vajda, "*An Extensive ODE Solver for Sensitivity Calculations*", Computers&Chemistry **8**, 255 (1984).

64. M. Alamgir, M. Orbán, and I. R. Epstein, "*Inorganic Bromate Oscillators. Bromate-Manganous-Reductant*", J. Phys. Chem. **87**, 3725 (1983).

65. M. Orbán, C. Dateo, P. De Kepper, and I. R. Epstein, "*Chlorite Oscillators: New Experimental Examples, Tristability, and Preliminary Classification*", J. Am. Chem. Soc. **104**, 5911 (1982).

66. W. Gelseler, "*Multiplicity, Stability, and Oscillations in the Stirred Flow Oxidation of Manganese(II) by Acidic Bromate*", J. Phys. Chem. **86**, 4394 (1982).

67. J. P. Birk and S. G. Kozub, "*Mechanism of the Reaction of Bromate Ion Bromate Ion by Hexacyanoferrate(II) and by Bromide Ion in Acidic Aqueous Solution*", Inorg. Chem. **12**, 2460 (1973).

68. J. Hale and H. Kocak, "*Dynamics and Bifurcations*", (Springer-Verlag, New York, 1991).

69. I. R. Epstein and Y. Luo, "*Differential Delay Equations in Chemical Kinetics. Nonlinear Models: The Cross-Shaped Phase Diagram and the Oregonator*", J. Chem. Phys. **95**, 244 (1991).

70. R. J. Olson and I. R. Epstein, "*Bifurcation Analysis of Chemical Reaction Mechanisms. II. Hopf Bifurcation Analysis*", J. Chem. Phys. **98**, 2805 (1993).

71. Graphics Software Systems, Inc., "*GSS*CGI FORTRAN Reference Booklet*", (GSS,Inc., Oregon, 1988).

72. Microsoft Corp., "*Microsoft FORTRAN Compiler Language Reference*", (Microsoft Corp., Redmond, WA, 1986).

73. Lahey Computer Systems, Inc., "*Lahey FORTRAN Language Reference*", (Lahey Comp. Sys., Inc., Incline Village, NV, 1992).

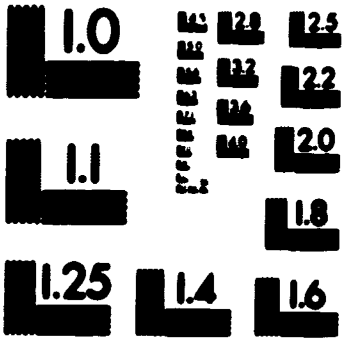
1.0
1.1
1.25
1.4
1.6
1.8
2.0
2.2
2.5
2.8
3.2
3.6
4.0

Appendix 1: Numerical continuation method for calculating steady state manifold

A1.1 The problem

The kinetic equations of a reaction network are

$$\frac{d\mathbf{X}}{dt} = \mathbf{f}(\mathbf{X}, a),$$

where $\mathbf{X}$ is the concentration vector of the intermediates, and a is a specific abscissa parameter. $\mathbf{X}$ is a steady state if

$$\frac{d\mathbf{X}}{dt} = \mathbf{f}(\mathbf{X}, a) = 0.$$

We need to calculate the steady state $\mathbf{X}$ in a given range of a. This is the mathematical problem of evaluating the dependence of the solution of a system of equations on a specific parameter. The result will be a function $\mathbf{X}(a)$.

A1.2 Dependence of the solution of a system of equations on a specific parameter

Consider a system of equations

$$\begin{aligned} f_1(X_1, X_2, \ldots, X_n, a) &= 0, \\ f_2(X_1, X_2, \ldots, X_n, a) &= 0, \\ &\vdots \\ f_n(X_1, X_2, \ldots, X_n, a) &= 0. \end{aligned} \tag{A.1}$$

We want to know $X_1, X_2, \ldots X_n$ at different a values. The procedure is as follows.

1. Rewrite equation (A.1) as

$$\begin{aligned} f_1(X_1, X_2, \ldots, X_n, X_{n+1}) &= 0, \\ f_2(X_1, X_2, \ldots, X_n, X_{n+1}) &= 0, \\ &\vdots \\ f_n(X_1, X_2, \ldots, X_n, X_{n+1}) &= 0, \end{aligned} \qquad (A.2)$$

   where $X_{n+1} = a$.

2. Differentiate each equation of (A.2) with respect to a variable we will call τ.

$$\frac{df_i}{d\tau} = \sum_{j=1}^{n+1} \frac{\partial f_i}{\partial X_j} \frac{dX_j}{d\tau} = 0 \qquad i = 1, 2, \ldots, n \qquad (A.3)$$

   We let τ be the arc length on the curve $\mathbf{X}(a)$.

3. Solve equation (A.3) for the unknowns $\frac{dX_1}{d\tau}, \frac{dX_2}{d\tau}, \ldots, \frac{dX_{k-1}}{d\tau}, \frac{dX_{k+1}}{d\tau}, \ldots, \frac{dX_n}{d\tau}, \frac{dX_{n+1}}{d\tau}$ assuming $\frac{dX_k}{d\tau}$ is a fixed independently adjustable variable. The unknowns are proportional to $\frac{dX_k}{d\tau}$ and the solution produces n numbers β_i such that

$$\frac{dX_i}{d\tau} = \beta_i \frac{dX_k}{d\tau} \qquad i = 1, 2, \ldots, k-1, k+1, \ldots, n+1. \qquad (A.4)$$

   An infinitesimal piece of the curve where $\mathbf{X}$ changes by $(dX_1, dX_2, \ldots, dX_n)$ has the infinitesimal length $d\tau$ where

$$d\tau^2 = \sum_{i=1}^{n+1} dX_i^2.$$

   Hence,

$$\sum_{i=1}^{n+1} (\frac{dX_i}{d\tau})^2 = 1.$$

Then $\frac{dX_k}{d\tau}$ is determined by the β_i coefficients as follows.

$$(\frac{dX_k}{d\tau})^2 = (1 + \sum_{i=1, i \neq k}^{n+1} \beta_i^2)^{-1}.$$

The subscript k is determined by the Gaussian elimination procedure when it chooses the best index for pivoting.

4. Predict the next point on the curve by integrating equation (A.4) using the Adams-Bashforth explicit multi-step method with an automatic adjustment in the order of approximation.

a). The first order approximation

$$\mathbf{X}_1 = \mathbf{X}_0 + h\frac{d\mathbf{X}_0}{d\tau} = \mathbf{X}_0 + h\mathbf{X}_0'$$

b). The second order approximation

$$\mathbf{X}_1 = \mathbf{X}_0 + 0.5h(3\mathbf{X}_0' - \mathbf{X}'_{-1})$$

c). The third order approximation

$$\mathbf{X}_1 = \mathbf{X}_0 + \frac{h}{12}(23\mathbf{X}_0' - 16\mathbf{X}'_{-1} + 5\mathbf{X}'_{-2})$$

d). The fourth-order approximation

$$\mathbf{X}_1 = \mathbf{X}_0 + \frac{h}{24}(55\mathbf{X}_0' - 59\mathbf{X}'_{-1} + 37\mathbf{X}'_{-2} - 9\mathbf{X}'_{-3})$$

where h is the step size; $\mathbf{X}_0, \mathbf{X}_{-1}, \mathbf{X}_{-2}, \mathbf{X}_{-3}$ are previous points; $\mathbf{X}_1$ is the new point that we want to calculate.

The order of approximation is chosen automatically by the program. It depends on the number of previous points available. It is set back to 1 whenever the step size is changed.

5. Correct the predicted point using Newton-Raphson (NR) iteration. The NR formula can be derived as follows.

Let $\Delta\mathbf{X}$ be the difference between the estimated point on the curve and the nearest true point on the curve, then

$$\begin{pmatrix} \frac{\partial f_1}{\partial x_1} & \frac{\partial f_1}{\partial x_2} & \cdots & \frac{\partial f_1}{\partial x_{k-1}} & \frac{\partial f_1}{\partial x_{k+1}} & \cdots & \frac{\partial f_1}{\partial x_{n+1}} \\ \frac{\partial f_2}{\partial x_1} & \frac{\partial f_2}{\partial x_2} & \cdots & \frac{\partial f_2}{\partial x_{k-1}} & \frac{\partial f_2}{\partial x_{k+1}} & \cdots & \frac{\partial f_2}{\partial x_{n+1}} \\ \vdots & \vdots & \ddots & \vdots & \vdots & \ddots & \vdots \\ \frac{\partial f_n}{\partial x_1} & \frac{\partial f_n}{\partial x_2} & \cdots & \frac{\partial f_n}{\partial x_{k-1}} & \frac{\partial f_n}{\partial x_{k+1}} & \cdots & \frac{\partial f_n}{\partial x_{n+1}} \end{pmatrix} \Delta\mathbf{X} = \mathbf{f}$$

or

$$\mathbf{\Gamma}_k \cdot \Delta\mathbf{X} = \mathbf{f},$$

where

$$\mathbf{\Gamma}_k = \begin{pmatrix} \frac{\partial f_1}{\partial x_1} & \frac{\partial f_1}{\partial x_2} & \cdots & \frac{\partial f_1}{\partial x_{k-1}} & \frac{\partial f_1}{\partial x_{k+1}} & \cdots & \frac{\partial f_1}{\partial x_{n+1}} \\ \frac{\partial f_2}{\partial x_1} & \frac{\partial f_2}{\partial x_2} & \cdots & \frac{\partial f_2}{\partial x_{k-1}} & \frac{\partial f_2}{\partial x_{k+1}} & \cdots & \frac{\partial f_2}{\partial x_{n+1}} \\ \vdots & \vdots & \ddots & \vdots & \vdots & \ddots & \vdots \\ \frac{\partial f_n}{\partial x_1} & \frac{\partial f_n}{\partial x_2} & \cdots & \frac{\partial f_n}{\partial x_{k-1}} & \frac{\partial f_n}{\partial x_{k+1}} & \cdots & \frac{\partial f_n}{\partial x_{n+1}} \end{pmatrix},$$

The correction to $\mathbf{X}$ that is required to get back to the curve is $-\Delta\mathbf{X}$, or

$$\mathbf{X}^*_{new} - \mathbf{X}^*_{old} = -\mathbf{\Gamma}_k^{-1}\mathbf{f}$$

where $\mathbf{X}^* = (X_1, X_2, \cdots, X_{k-1}, X_{k+1}, \cdots, X_{n+1})^T$.

Therefore,

$$\mathbf{X}^*_{new} = \mathbf{X}^*_{old} - \mathbf{\Gamma}_k^{-1}\mathbf{f}.$$

The convergence criteria should be set to reflect the required data accuracy. After the Newton iterations bring a data point onto the curve, another round of prediction using the predictor is carried out. It will produce another predicted point for the curve.

Appendix 2: Dominant extreme current approximation of the Gray-Scott network

When the dominant extreme current approximation method is applied to simplices in the current polytope of the Gray-Scott network, the simplices are divided into smaller simplicial regions, each with a given j ordering. The ordering gives the relative importance of the extreme currents in the region. In the following tables, the extreme currents are arranged in descending order of importance in the j orderings. The simplified steady state reaction rate vectors $\mathbf{v}_0$ are expressed in terms of the vector of the dominant currents.

For example, in case 1 the $\mathbf{v}_0$ column of the table gives $j_1 j_1 j_3 j_4 j_1 j_2$. This abbreviated notation means that $\mathbf{v}_0$ is approximated as

$$\mathbf{v}_0 = (j_1, j_1, j_3, j_4, j_1, j_2)$$

in the region. Under "j orderings with same $\mathbf{v}_0$", there are a number of cases, one of which is (1 2 3 4). This abbreviated notation means case 1 applies when $j_1 > j_2 > j_3 > j_4$.

The tables give $\mathbf{v}_0$ for all possible current polytope simplices of the Gray-Scott network. The current polytope can be decomposed into two simplices, such as $(1,2,3,4)$ and $(2,3,4,5)$ which are given in Tables A2.1 and A2.4. The alternative decomposition into simplices $(1,2,3,5)$ and $(1,3,4,5)$ uses the formulas in Tables A2.2 and A2.3. Refer to section 4.2 in the thesis for details.

A2.1 Simplex (E_1, E_2, E_3, E_4)

1. Reaction rates and j orderings

Case	$\mathbf{v}_0$	j orderings [illegible]
1	$j_1 j_1 j_3 j_4 j_1 j_2$	(1 2 3 4),(1 [illegible] 3 4 2),(1 4 2 3),(1 4 3 2)
2	$j_1 j_2 j_3 j_4 j_1 j_2$	(2 1 3 4),([illegible]
3	$j_1 j_2 j_3 j_4 j_3 j_2$	(2 3 1 4),([illegible]
4	$j_4 j_2 j_3 j_4 j_3 j_2$	(2 3 4 1),(3 [illegible] 2 1)
5	$j_4 j_2 j_3 j_4 j_4 j_2$	(2 4 1 3),(2 4 3 1),(4 1 2 3),(4 2 1 3),(4 2 3 1),(4 3 2 1)
6	$j_1 j_1 j_3 j_4 j_3 j_2$	(3 1 2 4),(3 1 4 2)
7	$j_4 j_1 j_3 j_4 j_3 j_2$	(3 4 1 2)
8	$j_4 j_1 j_3 j_4 j_4 j_2$	(4 1 3 2),(4 3 1 2)

2. (h, j) - (k, C) mapping

Case	$\mathbf{v}_0$	A	B	j_1	j_2	j_3	j_4
1	$j_1 j_1 j_3 j_4 j_1 j_2$	$\frac{k_2^2}{k_0 k_1 A_0}$	$\frac{k_0 A_0}{k_2}$	$k_0 A_0$	$k_0 B_0$	$\frac{k_2^2}{k_1 A_0}$	$\frac{k_0^2 A_0}{k_2}$
2	$j_1 j_2 j_3 j_4 j_1 j_2$	$\frac{k_2^2 A_0}{k_0 k_1 B_0^2}$	$\frac{k_0 B_0}{k_2}$	$k_0 A_0$	$k_0 B_0$	$\frac{k_2^2 A_0}{k_1 B_0^2}$	$\frac{k_0^2 B_0}{k_2}$
3	$j_1 j_2 j_3 j_4 j_3 j_2$	A_0	$\frac{k_0 B_0}{k_2}$	$\frac{k_0^2 k_1 A_0 B_0^2}{k_2^2}$	$k_0 B_0$	$k_0 A_0$	$\frac{k_0^2 B_0}{k_2}$
4	$j_4 j_2 j_3 j_4 j_3 j_2$	$\frac{k_2}{k_1 B_0}$	$\frac{k_0 B_0}{k_2}$	0	$B_0 k_0$	$k_0 A_0$	$\frac{k_0^2 B_0}{k_2}$
5	$j_4 j_2 j_3 j_4 j_4 j_2$	$\frac{k_2}{k_1 B_0}$	$\frac{k_0 B_0}{k_2}$	0	$k_0 B_0$	$\frac{k_0^2}{k_1 A_0}$	$k_0 A_0$
6	$j_1 j_1 j_3 j_4 j_3 j_2$	A_0	$\frac{k_2}{k_1 A_0}$	$\frac{k_2^2}{k_1 A_0}$	$k_0 B_0$	$k_0 A_0$	$\frac{k_0 k_2}{k_1 A_0}$
7	$j_4 j_1 j_3 j_4 j_3 j_2$	A_0	$\frac{k_0}{k_1 A_0}$	$\frac{k_0 k_2}{k_1 A_0}$	$k_0 B_0$	$k_0 A_0$	$\frac{k_0^2}{k_1 A_0}$
8	$j_4 j_1 j_3 j_4 j_4 j_2$	$\frac{k_0}{k_1 A_0}$	A_0	$k_2 A_0$	$k_0 B_0$	$\frac{k_0^2}{k_1 A_0}$	$k_0 A_0$

*** The simplified rate vector $\mathbf{v}_0$ in case 4 requires $k_2 = k_1 A_0 B_0$;**

The simplified rate vector $\mathbf{v}_0$ in case 5 requires $k_2 A_0 = k_0 B_0$.

A2.2 Simplex (E_1, E_2, E_3, E_5)

1. Reaction rates and j orderings

Case	$\mathbf{v}_0$	j orderings with same $\mathbf{v}_0$
9	$j_1j_1j_3j_5j_1j_2$	(1 2 3 5),(1 2 5 3),(1 3 2 5)
10	$j_1j_1j_3j_5j_1j_5$	(1 3 5 2),(1 5 2 3),(1 5 3 2),(5 1 2 3),(5 1 3 2)
11	$j_1j_2j_3j_5j_1j_2$	(2 1 3 5),(2 1 5 3),(2 5 1 3)
12	$j_1j_2j_3j_5j_3j_2$	(2 3 1 5),(2 3 5 1),(2 5 3 1),(3 2 1 5),(3 2 5 1)
13	$j_1j_1j_3j_5j_3j_2$	(3 1 2 5)
14	$j_1j_1j_3j_5j_3j_5$	(3 1 5 2),(3 5 1 2),(3 5 2 1),(5 3 1 2)
15	$j_1j_2j_3j_5j_1j_5$	(5 2 1 3)
16	$j_1j_2j_3j_5j_3j_5$	(5 2 3 1),(5 3 2 1)

2. (h, j) - (k, C) mapping

Case	$\mathbf{v}_0$	A	B	j_1	j_2	j_3	j_4
9	$j_1j_1j_3j_5j_1j_2$	$\frac{k_2^2}{k_0k_1A_0}$	$\frac{k_0A_0}{k_2}$	k_0A_0	k_0B_0	$\frac{k_2^2}{k_1A_0}$	$\frac{k_0^2A_0}{k_2}$
10	$j_1j_1j_3j_5j_1j_5$	$\frac{k_2}{k_1}$	B_0	k_0A_0	0	$\frac{k_0k_2}{k_1}$	k_0B_0
11	$j_1j_2j_3j_5j_1j_2$	$\frac{k_2^2A_0}{k_0k_1B_0^2}$	$\frac{k_0B_0}{k_2}$	k_0A_0	k_0B_0	$\frac{k_2^2A_0}{k_1B_0^2}$	$\frac{k_0^2B_0}{k_2}$
12	$j_1j_2j_3j_5j_3j_2$	A_0	$\frac{k_0B_0}{k_2}$	$\frac{k_0^2k_1A_0B_0^2}{k_2^2}$	k_0B_0	k_0A_0	$\frac{k_0^2B_0}{k_2}$
13	$j_1j_1j_3j_5j_3j_2$	A_0	$\frac{k_2}{k_0k_1}$	$\frac{k_2^2}{k_1A_0}$	k_0B_0	k_0A_0	$\frac{k_0k_2}{k_1A_0}$
14	$j_1j_1j_3j_5j_3j_5$	A_0	B_0	k_2B_0	0	k_0A_0	k_0B_0
15	$j_1j_2j_3j_5j_1j_5$	$\frac{k_0A_0}{k_1B_0^2}$	B_0	k_0A_0	k_2B_0	$\frac{k_0^2A_0}{k_1B_0^2}$	k_0B_0
16	$j_1j_2j_3j_5j_3j_5$	A_0	B_0	$k_1A_0B_0^2$	k_2B_0	k_0A_0	k_0B_0

* **The simplified rate vector $\mathbf{v}_0$ in case 10 requires $k_2B_0 = k_0A_0$;**

The simplified rate vector $\mathbf{v}_0$ in case 14 requires $k_2 = k_1A_0B_0$.

A2.3 Simplex (E_1, E_3, E_4, E_5)

1. Reaction rates and j orderings

Case	$\mathbf{v}_0$	j orderings with same $\mathbf{v}_0$
17	$j_1j_1j_3j_4j_1j_5$	(1 3 4 5),(1 4 3 5),(1 4 5 3)
18	$j_1j_1j_3j_5j_1j_5$	(1 3 5 4),(1 5 3 4),(1 5 4 3),(5 1 3 4),(5 1 4 3)
19	$j_1j_1j_3j_4j_3j_5$	(3 1 4 5)
20	$j_1j_1j_3j_5j_3j_5$	(3 1 5 4),(3 5 1 4),(5 3 1 4)
21	$j_4j_1j_3j_4j_3j_5$	(3 4 1 5),(3 4 5 1)
22	$j_4j_1j_3j_5j_3j_5$	(3 5 4 1),(5 3 4 1)
23	$j_4j_1j_3j_4j_4j_5$	(4 1 3 5),(4 1 5 3),(4 3 1 5),(4 3 5 1),(4 5 1 3),(4 5 3 1)
24	$j_4j_1j_3j_5j_4j_5$	(5 4 1 3),(5 4 3 1)

2. (h, j) - (k, C) mapping

Case	$\mathbf{v}_0$	A	B	j_1	j_2	j_3	j_4
17	$j_1j_1j_3j_4j_1j_5$	$\frac{k_2^2}{k_0k_1A_0}$	$\frac{k_0A_0}{k_2}$	k_0A_0	$\frac{k_2^2}{k_1A_0}$	$\frac{k_0^2A_0}{k_2}$	k_0B_0
18	$j_1j_1j_3j_5j_1j_5$	$\frac{k_2}{k_1}$	B_0	k_0A_0	$\frac{k_0k_2}{k_1}$	0	k_0B_0
19	$j_1j_1j_3j_4j_3j_5$	A_0	$\frac{k_2}{k_1A_0}$	$\frac{k_2^2}{k_1A_0}$	k_0A_0	$\frac{k_0k_2^2}{k_1A_0}$	k_0B_0
20	$j_1j_1j_3j_5j_3j_5$	A_0	B_0	k_2B_0	k_0A_0	0	k_0B_0
21	$j_4j_1j_3j_4j_3j_5$	A_0	$\frac{k_0}{k_1A_0}$	$\frac{k_0k_2}{k_1A_0}$	k_0A_0	$\frac{k_0^2}{k_1A_0}$	k_0B_0
22	$j_4j_1j_3j_5j_3j_5$	A_0	B_0	k_2B_0	k_0A_0	$k_1A_0B_0^2$	k_0B_0
23	$j_4j_1j_3j_4j_4j_5$	$\frac{k_0}{k_1A_0}$	A_0	k_2A_0	$\frac{k_0^2}{k_1A_0}$	k_0A_0	k_0B_0
24	$j_4j_1j_3j_5j_4j_5$	$\frac{k_0A_0}{k_1B_0^2}$	B_0	k_2B_0	$\frac{k_0^2A_0}{k_1B_0^2}$	k_0A_0	k_0B_0

* The simplified rate vector $\mathbf{v}_0$ in case 18 requires $k_2B_0 = k_0A_0$;

The simplified rate vector $\mathbf{v}_0$ in case 20 requires $k_2 = k_1A_0B_0$.

A2.4 Simplex (E_2, E_3, E_4, E_5)

1. Reaction rates and j orderings

Case	v_0	j orderings with same v_0
25	$j_4j_2j_3j_4j_3j_2$	(2 3 4 5),(3 2 4 5),(3 4 2 5)
26	$j_4j_2j_3j_5j_3j_2$	(2 3 5 4),(2 5 3 4),(3 2 5 4),(3 5 2 4),(3 5 4 2)
27	$j_4j_2j_3j_4j_4j_2$	(2 4 3 5),(2 4 5 3),(4 2 3 5),(4 2 5 3),(4 3 2 5)
28	$j_4j_2j_3j_5j_4j_2$	(2 5 4 3)
29	$j_4j_2j_3j_4j_3j_5$	(3 4 5 2)
30	$j_4j_2j_3j_4j_4j_5$	(4 3 5 2),(4 5 2 3),(4 5 3 2)
31	$j_4j_2j_3j_5j_3j_5$	(5 2 3 4),(5 3 2 4),(5 3 4 2)
32	$j_4j_2j_3j_5j_4j_5$	(5 2 4 3),(5 4 2 3),(5 4 3 2)

2. (h, j) - (k, C) mapping

Case	v_0	A	B	j_1	j_2	j_3	j_4
25	$j_4j_2j_3j_4j_3j_2$	$\frac{k_2}{k_1B_0}$	$\frac{k_0B_0}{k_2}$	k_0B_0	k_0A_0	$\frac{k_0^2B_0}{k_2}$	0
26	$j_4j_2j_3j_5j_3j_2$	A_0	$\frac{k_0B_0}{k_2}$	k_0B_0	k_0A_0	$\frac{k_1A_0^2B_0^2}{k_2^2}$	$\frac{k_0^2B_0}{k_2}$
27	$j_4j_2j_3j_4j_4j_2$	$\frac{k_2}{k_1B_0}$	$\frac{k_0B_0}{k_2}$	k_0B_0	$\frac{k_0^2}{k_1A_0}$	k_0A_0	0
28	$j_4j_2j_3j_5j_4j_2$	$\frac{k_2^2A_0}{k_0k_1B_0^2}$	$\frac{k_0B_0}{k_2}$	k_0B_0	$\frac{k_2^2A_0}{k_0k_1B_0^2}$	k_0A_0	$\frac{k_0^2B_0}{k_2}$
29	$j_4j_2j_3j_4j_3j_5$	A_0	$\frac{k_0}{k_1A_0}$	$\frac{k_0k_2}{k_1A_0}$	k_0A_0	$\frac{k_0^2}{k_1A_0}$	k_0B_0
30	$j_4j_2j_3j_4j_4j_5$	$\frac{k_0}{k_1A_0}$	A_0	k_2A_0	$\frac{k_0^2}{k_1A_0}$	k_0A_0	k_0B_0
31	$j_4j_2j_3j_5j_3j_5$	A_0	B_0	k_2B_0	k_0A_0	$k_1A_0B_0^2$	k_0B_0
32	$j_4j_2j_3j_5j_4j_5$	$\frac{k_0A_0}{k_1B_0^2}$	B_0	k_2B_0	$\frac{k_2^2A_0}{k_1B_0^2}$	k_0A_0	k_0B_0

* **The simplified rate vector v_0 in case 25 requires $k_0 = k_1A_0B_0$;**

The simplified rate vector v_0 in case 27 requires $k_2A_0 = k_0B_0$.

Appendix 3: Data points on the published phase diagrams of the BSF network[25]

Note

The tables list a "stability code" beside each point. The meaning of the code is as follows.

Stability Code	Meaning
1	SSI = lower stable steady state
2	SSII = higher stable steady state
3	bistability between two stable steady states
4	oscillations only
5	bistability between an oscillatory state and a lower stable steady state
6	bistability between an oscillatory state and a higher stable steady state

A3.1 The calculated phase diagram with $k_9 = 32.5\ M^{-2}s^{-1}$

k_0	$[SO_3^{2-}]_0$	stability
3.50×10^{-3}	0.030	2
5.50×10^{-3}	0.030	2
7.00×10^{-3}	0.030	2
9.00×10^{-3}	0.030	2
2.75×10^{-3}	0.040	2
4.25×10^{-3}	0.040	2
5.00×10^{-3}	0.040	2
6.00×10^{-3}	0.040	2
7.00×10^{-3}	0.040	2
8.00×10^{-3}	0.040	2
2.00×10^{-3}	0.050	2
4.00×10^{-3}	0.050	2
4.50×10^{-3}	0.050	2
5.00×10^{-3}	0.050	3
6.00×10^{-3}	0.050	3
7.00×10^{-3}	0.050	3
7.50×10^{-3}	0.050	3
8.00×10^{-3}	0.050	1
9.00×10^{-3}	0.050	1
1.75×10^{-3}	0.060	2
2.50×10^{-3}	0.060	2
3.00×10^{-3}	0.060	2
3.50×10^{-3}	0.060	3
4.00×10^{-3}	0.060	3
4.50×10^{-3}	0.060	1
6.00×10^{-3}	0.060	1
8.50×10^{-3}	0.060	1
1.00×10^{-3}	0.075	2
1.50×10^{-3}	0.075	2
2.00×10^{-3}	0.075	6
2.25×10^{-3}	0.075	6
2.50×10^{-3}	0.075	1
4.00×10^{-3}	0.075	1
7.00×10^{-3}	0.075	1
5.00×10^{-4}	0.085	2
1.00×10^{-3}	0.085	2
1.50×10^{-3}	0.085	4
1.75×10^{-3}	0.085	4
2.00×10^{-3}	0.085	1
5.00×10^{-3}	0.085	1
5.00×10^{-4}	0.100	4
1.00×10^{-3}	0.100	4
1.50×10^{-3}	0.100	1
3.00×10^{-3}	0.100	1

A3.2 The experimental phase diagram at 20°C

k_0	$[SO_3^{2-}]_0$	stability
2.00×10^{-3}	0.025	2
5.00×10^{-3}	0.025	2
9.00×10^{-3}	0.025	2
2.00×10^{-3}	0.030	2
5.00×10^{-3}	0.030	2
9.00×10^{-3}	0.030	2
5.00×10^{-3}	0.040	2
6.00×10^{-3}	0.040	3
7.00×10^{-3}	0.040	3
8.00×10^{-3}	0.040	3
9.00×10^{-3}	0.040	3
9.50×10^{-3}	0.040	3
3.00×10^{-3}	0.050	2
4.00×10^{-3}	0.050	3
5.00×10^{-3}	0.050	3
6.00×10^{-3}	0.050	3
7.00×10^{-3}	0.050	1
9.50×10^{-3}	0.050	1
1.00×10^{-3}	0.060	2
1.50×10^{-3}	0.060	2
2.00×10^{-3}	0.060	4
2.50×10^{-3}	0.060	4
3.00×10^{-3}	0.060	1
4.00×10^{-3}	0.060	1
5.00×10^{-3}	0.060	1
9.50×10^{-3}	0.060	1
5.00×10^{-4}	0.075	2
1.00×10^{-3}	0.075	4
1.50×10^{-3}	0.075	1
2.00×10^{-3}	0.075	1
3.00×10^{-3}	0.075	1
4.00×10^{-3}	0.075	1
5.00×10^{-3}	0.075	1
9.50×10^{-3}	0.075	1
5.00×10^{-4}	0.100	4
1.00×10^{-3}	0.100	1
2.00×10^{-3}	0.100	1
3.00×10^{-3}	0.100	1
4.00×10^{-3}	0.100	1
5.00×10^{-3}	0.100	1

A3.3 The experimental phase diagram at 30°C

k_0	$[SO_3^{2-}]_0$	stability
2.00×10^{-3}	0.025	2
5.00×10^{-3}	0.025	2
9.70×10^{-3}	0.025	2
5.00×10^{-3}	0.040	2
8.00×10^{-3}	0.040	2
9.50×10^{-3}	0.040	2
1.00×10^{-3}	0.050	2
2.00×10^{-3}	0.050	2
3.00×10^{-3}	0.050	2
3.50×10^{-3}	0.050	3
5.00×10^{-3}	0.050	3
5.50×10^{-3}	0.050	3
6.00×10^{-3}	0.050	3
6.50×10^{-3}	0.050	1
9.50×10^{-3}	0.050	1
2.00×10^{-3}	0.060	2
2.25×10^{-3}	0.060	2
2.50×10^{-3}	0.060	4
3.00×10^{-3}	0.060	4
3.50×10^{-3}	0.060	1
4.00×10^{-3}	0.060	1
5.00×10^{-3}	0.060	1
7.00×10^{-3}	0.060	1
9.50×10^{-3}	0.060	1
5.00×10^{-4}	0.075	2
1.00×10^{-3}	0.075	4
1.25×10^{-3}	0.075	4
1.50×10^{-3}	0.075	4
2.00×10^{-3}	0.075	1
3.00×10^{-3}	0.075	1
4.00×10^{-3}	0.075	1
5.00×10^{-3}	0.075	1
9.50×10^{-3}	0.075	1
5.00×10^{-4}	0.100	4
7.50×10^{-4}	0.100	4
1.00×10^{-3}	0.100	1
2.00×10^{-3}	0.100	1
3.00×10^{-3}	0.100	1
4.00×10^{-3}	0.100	1
5.00×10^{-3}	0.100	1

A3.4 The experimental phase diagram at 40°C

k_0	$[SO_3^{2-}]_0$	stability
1.00×10^{-3}	0.040	2
5.00×10^{-3}	0.040	2
9.50×10^{-3}	0.040	2
6.00×10^{-3}	0.050	2
7.50×10^{-3}	0.050	2
8.00×10^{-3}	0.050	3
8.50×10^{-3}	0.050	3
9.50×10^{-3}	0.050	1
3.00×10^{-3}	0.060	2
3.50×10^{-3}	0.060	2
4.00×10^{-3}	0.060	4
5.00×10^{-3}	0.060	4
5.50×10^{-3}	0.060	1
6.00×10^{-3}	0.060	1
9.50×10^{-3}	0.060	1
1.00×10^{-3}	0.075	2
1.50×10^{-3}	0.075	2
2.00×10^{-3}	0.075	4
3.00×10^{-3}	0.075	4
4.00×10^{-3}	0.075	1
5.00×10^{-3}	0.075	1
7.00×10^{-3}	0.075	1
9.50×10^{-3}	0.075	1
5.00×10^{-4}	0.100	2
7.50×10^{-4}	0.100	2
1.00×10^{-3}	0.100	4
1.75×10^{-3}	0.100	4
2.00×10^{-3}	0.100	1
2.50×10^{-3}	0.100	1
3.00×10^{-3}	0.100	1
4.00×10^{-4}	0.100	1
5.00×10^{-3}	0.100	1

Appendix 4: Computational techniques

I developed a FORTRAN program for calculating the steady state manifold, the stability regions on the steady state manifold, and the stability boundaries in experimental parameter space. I wrote a graphics program in CGI (Computer Graphics Interface)[71] to plot these curves. I also rewrote subroutines which generate the polynomials in the $(\mathbf{h},\mathbf{j})$ parameters. Some of the key concepts and algorithms used in my new software are described below. This information on the software should be of interest to users of the SNA package.

A4.1 Managing large polynomials in $(\mathbf{h},\mathbf{j})$ *parameters*

Stability analysis in the $(\mathbf{h},\mathbf{j})$ parameters involves expanding Δ_{d-1} and α_i as polynomials in these parameters. Huge number of terms can be produced. An efficient algorithm had to be developed in order to treat the networks which represent realistic chemical mechanisms.

The characteristic equation (27) is

$$\lambda^n + \alpha_1(\mathbf{h},\mathbf{j})\lambda^{n-1} + \alpha_2(\mathbf{h},\mathbf{j})\lambda^{n-2} + \cdots + \alpha_{n-1}(\mathbf{h},\mathbf{j}) + \alpha_n(\mathbf{h},\mathbf{j}) = 0$$

where $\alpha_1, \alpha_2, \cdots, \alpha_n$ are summations of many polynomial terms. It can be proved that for any term in the α_i,

1. The sum of the exponents of all j's equals the sum of the exponents of all h's$= i$;
2. the exponent of each h equals either 1 or 0.

These properties enable us to handle the polynomials using individual bits in computer memory. For example, a term $h_1h_3h_4h_7\cdots$ can be stored as

Bit #:	1	2	3	4	5	6	7	......	n
	1	0	1	1	0	0	1	......	0
	h_1	h_2	h_3	h_4	h_5	h_6	h_7	......	h_n

Thus, a four-byte computer word can handle up to 32 species, which would be a large network.

The exponents of the **j** parameters are treated in the similar way to the h exponents. The difference is that the j exponents can be much bigger than 1. So, we have to use more than one bit to store a j exponent. If the number of independent intermediates is n, then we need $\log_2(n+1)$ (rounded up) bits for each j component. The j components are always put in the higher bits of a word memory.

When polynomial terms are stored this way in memory, one can multiply two terms by adding the exponents. Doing bit-level manipulations makes the computation very fast. Access to the exponent of a specific h or j parameter is achieved using bit shift and bit rotation operations[72,73].

A4.2 Mapping between polynomial terms and memory addresses

A large amount of memory can be saved by storing only the coefficients of the polynomial terms at memory addresses which are in one-to-one correspondence with the possible exponents. This way, we do not need to explicitly store the exponents in memory.

The one-to-one mapping needed to convert polynomial terms and memory addresses to each other cannot be expressed as an explicit function, but can be calculated by a computer algorithm.

An example illustrates the algorithm. For a reaction network with four extreme currents and four independent intermediates, we have $f = 4$ and $n = 4$, where f is the number of currents. To set up a mapping between a polynomial term and an address, we first set up a mapping between every possible set of exponents of the $\mathbf{j}$ parameters and a *j-address*. The following table gives the exponents of j_3, j_2, and j_1 for each j-address.

j-address	j_3	j_2	j_1
0	0	0	0
1	0	0	1
2	0	0	2
3	0	0	3
4	0	0	4
5	0	1	0
6	0	1	1
7	0	1	2
8	0	1	3
9	0	2	0
10	0	2	1
11	0	2	2
12	0	3	0
13	0	3	1
14	0	4	0
15	1	0	0
16	1	0	1
17	1	0	2
18	1	0	3
19	1	1	0
20	1	1	1
21	1	1	2
22	1	2	0
23	1	2	1
24	1	3	0
25	2	0	0
26	2	0	1
27	2	0	2
28	2	1	0
29	2	1	1
30	2	2	0
31	3	0	0
32	3	0	1
33	3	1	0
34	4	0	0

For the polynomial α_i, we have $\sum_{k=1}^{J} l_k = i$, where l_k means the exponent of j_k. So,

$$l_4 = 4 - \sum_{k=1}^{3} l_k$$

for our example.

The mapping between the j-address and the exponents of the j parameters are constructed by filling the numbers into the columns starting from the j_1 column.

We increase the number one by one on the column until the summations of numbers in all j columns reach the number i, which is the subscript of the α_i. Then at the next entry, we eliminate the number on the column to 0 and add 1 to the column on the left. We treat every column in the same manner until the number on the most left column reach the value i.

In actual calculations, we do not need to construct the whole table as above. We only fill in the table until the j sequence of exponents in the table matches our j sequence. The corresponding j-address is the one we need.

The ***true address*** of a term is obtained by shifting the j-address n bits to the left in the memory and adding the bit sequence for the h exponents as discussed in the last section.

Let's use the polynomial term $j_4 j_3 j_2 j_1 h_4 h_3 h_2 h_1$ as an example to show how the address is calculated. Since the sum of the exponents is 4 one exponent can be ignored. We ignore j_4. The exponents of the sequence (j_3, j_2, j_1) are (1,1,1), so the j-address corresponding to the (1,1,1) is 20 according to the above mapping. To shift the j-address 4 bits to the left we multiply by 2^4 to get 20×2^4. The exponents of $h_4 h_3 h_2 h_1$ are (1,1,1,1) whose bit pattern is the number $2^4 - 1$. The address is calculated by combining the bit pattern.

$$address = 20 \times 2^4 + 2^4 - 1 = 335.$$

To get the polynomial term from the address, the same procedure is carried out backwards. In addition, there is one more final step to calculate the exponent of j_4 using the equation $l_4 = 4 - \sum_{k=1}^{3} l_k$.

A4.3 Bookkeeping of minor addresses in memory

To get the characteristic equation from a Jacobian matrix, the determinant $|\mathbf{I}\lambda - \mathbf{M}|$ is expanded. In the expansion, a series of minors is calculated. Each minor can contain many large polynomials. Keeping track of the positions of the polynomial terms in memory is a memory-consuming task. In the process of calculating the Hurwitz determinants, there are also many minors to be calculated and stored in memory temporarily.

I developed a method to handle these problems efficiently. Here are the basic ideas.

1. Minor numbers

   When determinants are expanded, the polynomials representing successively larger minors are stored in memory. The minors are indexed by column numbers. The combinations of column numbers indexing minors are called the *minor numbers*. For example:

$$\begin{vmatrix} a_{11} & a_{12} \\ a_{21} & a_{22} \end{vmatrix} = \text{minor}(1,2) \qquad \begin{vmatrix} a_{11} & a_{13} \\ a_{21} & a_{23} \end{vmatrix} = \text{minor}(1,3)$$

$$\begin{vmatrix} a_{12} & a_{14} \\ a_{22} & a_{24} \end{vmatrix} = \text{minor}(2,4) \qquad \cdots \begin{vmatrix} a_{1i} & a_{1j} \\ a_{2i} & a_{2j} \end{vmatrix} = \text{minor}(i,j), \quad j > i$$

$$\begin{vmatrix} a_{1i} & a_{1j} & a_{1k} \\ a_{2i} & a_{2j} & a_{2k} \\ a_{3i} & a_{3j} & a_{3k} \end{vmatrix} = \text{minor}(i,j,k) \qquad k > j > i$$

$$\vdots$$

$$\begin{vmatrix} a_{11} & a_{12} & \cdots & a_{1n} \\ a_{21} & a_{22} & \cdots & a_{2n} \\ \vdots & \vdots & \ddots & \vdots \\ a_{n1} & a_{n2} & \cdots & a_{nn} \end{vmatrix} = \text{minor}(1,2,\cdots,n) = |\mathbf{I}\lambda - \mathbf{M}|$$

2. Converting a minor number into a single integer number

In an early version of the stability analysis program, the address range of the minors involving columns (i, j, k, l) was stored in a matrix whose subscripts are (i, j, k, l). This method of storage wastes memory and it is limited by the number of subscripts allowed for arrays in some Fortran compilers.

The method that I developed for storing the address range of minors has no such limitations. It uses an integer variable that has at least n bits to do the conversion. All bits whose sequential numbers appear in the minor number are set to 1 and all other bits are set to 0. A single integer number corresponding to the minor number is produced.

Example:

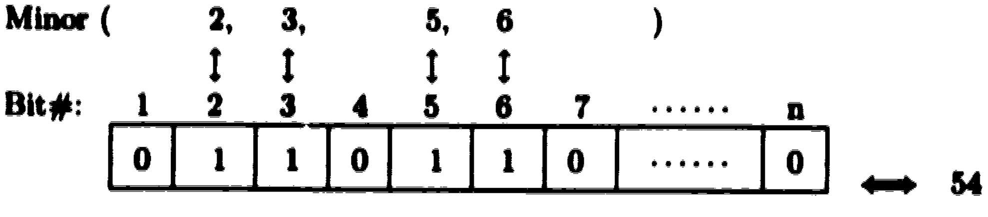

An *address array* uses this number as an index. It stores the starting and ending addresses of terms in the minor referred to by the index. For the minor (2,3,5,6) above whose index is 54 the starting and ending addresses of the polynomial are stored as follows:

D(54,1) ⟵ starting addresses of minor (2,3,5,6)

D(54,2) ⟵ ending addresses of minor (2,3,5,6).

These techniques make it possible to construct the Hurwitz determinant polynomials for networks with as many as 19 intermediates on a personal computer with 16MB of memory.

END

28-08-96

FIN